

E201 742

AD-A275 569



(2)

PL-TR-92-2231

Advanced Spectral Modeling Development

**R.G. Isaacs
S.A. Clough
R.D. Worsham
J.L. Moncet
W.O. Gallery**

**S DTIC
ELECTE
JAN 26 1994
A**

**Atmospheric and Environmental Research, Inc.
840 Memorial Drive
Cambridge, MA 02139**

14 September 1992

**Final Report
14 July 1989-14 July 1992**

Approved for Public Release; distribution unlimited



**PHILLIPS LABORATORY
Directorate of Geophysics
AIR FORCE MATERIEL COMMAND
HANSCom AIR FORCE BASE, MA 01731-3010**

94 1 25 070


94-02287



**Best
Available
Copy**

"This technical report has been reviewed and is approved for publication".


CARL P. ANDERSON
Contract Manager


WILLIAM A.M. BLUMBERG
Branch Chief


ROGER A. VAN TASSEL
Division Director

This report has been reviewed by the ESC Public Affairs Office (PA) and is releasable to the National Technical Information Service (NTIS).

Qualified requestors may obtain additional copies from the Defense Technical Information Center (DTIC). All others should apply to the National Technical Information Service (NTIS).

If your address has changed, or if you wish to be removed from the mailing list, or if the addressee is no longer employed by your organization, please notify PL/TSI, 29 Randolph Road, Hanscom AFB, MA 01731-3010. This will assist us in maintaining a current mailing list.

Do not return copies of this report unless contractual obligations or notices on a specific document requires that it be returned.

BEST AVAILABLE COPY

REPORT DOCUMENTATION PAGE			Form Approved OMB No. 0704-0188	
<small>Public reporting burden for this collection of information is estimated to average 1 hour per response, including the time for reviewing instructions, searching existing data sources, gathering and maintaining the data needed, and completing and reviewing the collection of information. Send comments regarding this burden estimate or any other aspect of this collection of information, including suggestions for reducing the burden, to Washington Headquarters Service, Directorate for Information Operations and Reports, 1215 Jefferson Davis Highway, Suite 1204, Arlington, VA 22202-4302, and to the Office of Management and Budget, Paperwork Reduction Project (0704-0188), Washington, DC 20503.</small>				
1. AGENCY USE ONLY (Leave blank)		2. REPORT DATE 14 September 1992		3. REPORT TYPE AND DATES COVERED Final (14 July 1989 - 14 July 1992)
4. TITLE AND SUBTITLE Advanced Spectral Modeling Development			5. FUNDING NUMBERS PE 62101F PR 7670 TA 09 WU BG Contract F19628-89-C-0150	
6. AUTHOR(S) R. G. Isaacs R. D. Worsham W.O. Gallery S. A. Clough J. L. Moncet				
7. PERFORMING ORGANIZATION NAME(S) AND ADDRESS(ES) Atmospheric and Environmental Research, Inc. 840 Memorial Drive Cambridge, MA 02139			8. PERFORMING ORGANIZATION REPORT NUMBERS	
9. SPONSORING / MONITORING AGENCY NAME(S) AND ADDRESS(ES) Phillips Laboratory 29 Randolph Road Hanscom AFB, MA 01731-3010 Contract Manager: Gail Anderson/GPOS			10. SPONSORING / MONITORING AGENCY REPORT NUMBER PL-TR-92-2231	
11. SUPPLEMENTARY NOTES				
12a. DISTRIBUTION / AVAILABILITY STATEMENT Approved for public release; Distribution unlimited			12b. DISTRIBUTION CODE	
13 ABSTRACT (Maximum 200 words) <p>This report describes the results of a basic research program to develop advanced spectral modeling techniques to treat a variety of current topics in spectroscopy and radiative transfer relevant to the modeling of atmospheric transmission and radiance fields. These include optimizing multiple scattering, surface properties, line coupling, line shapes, interferometric instrument function, and model validation. The overall goal of this research was the improvement of transmittance/radiance simulation modeling physics through continual model validation of results. Results of this study will enhance the capability to model atmospheric transmission and emission in support of DoD and other users.</p> <p>The report is divided into sections based on model physics areas which were investigated in the course of the contract. This work was done in support of the Advanced Spectral Modeling effort conducted by the Phillips Laboratory, Optical Physics Division.</p>				
14. SUBJECT TERMS Atmospheric transmission Spectral algorithm development Radiative transfer Spectroscopy			15. NUMBER OF PAGES 84	
			16. PRICE CODE	
17. SECURITY CLASSIFICATION OF REPORT Unclassified	18. SECURITY CLASSIFICATION OF THIS PAGE Unclassified	19. SECURITY CLASSIFICATION OF ABSTRACT Unclassified	20. LIMITATION OF ABSTRACT SAR	

TABLE OF CONTENTS

	Page
1. Introduction	1
2. Approach	2
3. Cross Section Data/Lorentz Capability	2
4. Atmospheric Multiple Scattering	5
4.1 Large Solar Zenith Angle Scattering	5
4.2 "Exact" Multiple Scattering	10
5. Heating Rates and Fluxes	12
6. Scattering Properties of Precipitation	17
7. Surface Properties	19
7.1 Visible and Near IR Surface Reflection	19
7.2 Microwave Surface Emissivities	22
8. Isotopic Ratios	25
9. Instrument Function Enhancements	27
9.1 Scanning Functions in the Spectral Domain	27
9.2 Scanning Functions in the Fourier Domain	28
9.2.1 Theory	29
9.2.2 Examples	31
9.2.3 Implementation	33
9.3 Interpolation	33
10. Line Shape	34
10.1 Line Shape for Carbon Dioxide	34
10.2 Line Coupling for Carbon Dioxide	37
11. Collision Induced Bands	45
12. Spectral Model Enhancements	45
13. Advanced Spectral Model Validation	48
13.1 Validation with Data from the High-resolution Interferometer Sounder (HIS)	48
13.2 ITRA Microwave Validation	58

TABLE OF CONTENTS (continued)

	<u>Page</u>
13.3 High Altitude Modeling Support Activities	65
13.3.1 MSX	65
13.3.2 Celestial Occultation Experiment	66
13.3.3 Earthlimb Experiments	68
13.3.4 MSX Contributions to Global Climate Monitoring	69
14. Support for Annual Review Conference	69
15. Conclusions	72
16. References	72

DTIC QUALITY INSPECTED 5

Accession For	
NTIS CRA&I	<input checked="" type="checkbox"/>
DTIC TAB	<input type="checkbox"/>
Unannounced	<input type="checkbox"/>
Justification	
By	
Distribution /	
Availability Codes	
Dist	Avail and/or Special
A-1	

LIST OF FIGURES

Figure		Page
1	The contribution of CCl_4 (790 cm^{-1}), CFC11 (850 cm^{-1}) and CFC12 (925 cm^{-1}) to the transmittance of an atmospheric layer at 975 mb.	6
2	The transmittance of the same layer as Figure 1 except that the spectral cross section data have been convolved with a Lorentzian to account for the effect of atmospheric pressure broadening.	6
3	Multiple scattering "quick fix".	8
4	Multiple scattering "quick fix": comparison to DOM.	9
5	Interface routine.	11
6	Limb layer radiance spectrum utilized for development of the improved radiance algorithm. The units are equivalent brightness temperature.	14
7	Radiance error in equivalent brightness temperature due to treatment of the layer as isothermal.	15
8	Radiance error utilizing the improved radiance algorithm.	15
9	Legendre polynomial coefficients of a Marshall-Palmer size distribution with a rainfall rate of 5 mmh^{-1} at four frequencies.	18
10	Spectral albedos for different surface types. Curves are given for new snow (\odot), old snow (Δ), a plowed field of clay loam (+), green plants (x), and a smooth ocean at solar zenith angles of 0° (\diamond) and 55° (\uparrow).	21
11	LOWTRAN radiance calculations with surface albedos in Figure 11.	23
12	(a) Variation of 54° look-angle polarized emissivity (ϵ_v , ϵ_η) with surface model at frequencies of 1.2, 5.0, 10.6, 18.0, and 35.0 GHz. (Surface models 1-6, Table 3) (b) Same as (a). (Surface models 7-12, Table 3.).	26
13	The Five FTS Scanning Functions and Their Associated Apodization Functions Available in FFTSCAN.	30
14	(a) FASCODE Calculated Spectrum Smoothed by FFTSCAN Plus The Error In the Smoothed Spectrum from using: (b) FFTSCAN With Boxcaring, and (c) the FASCODE3 Scanning Function.	32
15	The chi function for carbon dioxide with $V_0 = 2\text{ cm}^{-1}$. The solid line is for halfwidth of 0.08 cm^{-1} (1 atm) and the dashed line is for a halfwidth of 0.008 cm^{-1} (0.1 atm).	36

LIST OF FIGURES (continued)

Figure		Page
16	The chi function for carbon dioxide with $V_0 = 8 \text{ cm}^{-1}$. The solid line is for halfwidth of 0.08 cm^{-1} (1 atm) and the dashed line is for a halfwidth of 0.008 cm^{-1} (0.1 atm).	36
17	(a) Calculated limb transmittance spectrum with $V_0 = 2 \text{ cm}^{-1}$; (b) Calculated limb transmittance spectrum with $V_0 = 8 \text{ cm}^{-1}$	38
18	An ATMOS occultation transmittance spectrum. The tangent height is 20.5 km.	39
19	A calculation with $V_0 = 2 \text{ cm}^{-1}$ for the measurement conditions of Figure 19.	39
20	Limb transmittance spectrum for the conditions of the ITRA intercomparison with a 30 km tangent height for $V_0 = 2 \text{ cm}^{-1}$	40
21	Limb transmittance spectrum for the conditions of the ITRA intercomparison with a 30 km tangent height for $V_0 = 8 \text{ cm}^{-1}$	40
22	Effect of line coupling on the spectral residuals for the nadir HIS observation of 14 April 1986: a) no line coupling, b) line coupling with the basis coupling coefficients, and c) basis coupling coefficients multiplied by a factor of 1.3.	42
23	Effect of line coupling on the spectral residuals for the zenith observation of 1 November 1988 with the HIS instrument: a) no line coupling, b) line coupling with the basis coupling coefficients, and c) basis coupling coefficients multiplied by a factor of 1.3.	43
24	Brightness temperature residuals associated with Figure 22 as a function of brightness temperature.	44
25	HIS equivalent brightness spectra from April 14, 1986: nadir view over ocean from 19.6 km.	52
26	The difference spectrum in equivalent brightness temperature between the spectrum of Figure 26 and a calculated spectrum using FASCODE with the 1986 HITRAN line parameters. An error of 1 K in the window region at 1000 cm^{-1} corresponds to a 1.6% error in radiance.	52
27	The difference spectrum in equivalent brightness temperature between the spectrum of Figure 26 and a calculated spectrum using FASCODE with the inclusion of the effects of line coupling and improved carbon dioxide line parameters.	54

LIST OF FIGURES (continued)

Figure		Page
28	The difference spectrum in equivalent brightness temperature between the spectrum of Figure 26 and a calculated spectrum using FASCODE. The effect of CCl ₄ at 795 cm ⁻¹ , CFC11 at 850 cm ⁻¹ and CFC12 at 920 cm ⁻¹ have been taken into account in addition to the effects included in Figure 28.	54
29	The difference spectrum in equivalent brightness temperature between the spectrum of Figure 26 and a calculated spectrum using FASCODE. The effect of a thin cirrus cloud at 13 km has been included in addition to the effects treated in Figures 28 and 29.	55
30	Zenith radiance spectrum observed with the U. of Wisconsin HIS instrument at Denver, CO, 1 Nov. 1988, as part of the GAPEX campaign.	57
31	Radiance residuals between the observed spectral radiance of Figure 31 and a FASCODE calculation with a radiosonde defined atmosphere.	57
32	Sources of Spectral Radiance as Seen by the Spirit III Interferometer Viewing the Limb at a Tangent Height of 60 km.	67
33	Timeline for the stairstep maneuver for ELE-1.	70
34	Experiment timeline, from park to park, for ELE-1 showing the instrument modes, the spacecraft maneuvers, and the orbital positions.	70
35	Timeline for the sawtooth vertical profile scan for ELE-10.	71

LIST OF TABLES

<u>Table</u>	<u>Page</u>
1 First Moment Quadrature Direction Cosine Values, Weights and Representative Flux Errors	16
2 Radiative Source Functions. Forms of Boundary, $R_i(P_b)$, and Atmospheric, $S(p)$, Contributions to Sensor-incident Radiances, $R_i(\theta)$	20
3 Surface Model Types and Modeling Approaches	24
4 Comparison of Computational Time and Accuracy Among Three Scanning Function Options for the Sinc, Sinc2, and Triangle Scanning Functions	33
5 Characteristics of the HIS Instrument for Flight of 14 April 1986	49
6 The Input Atmosphere for the Validations in FASCODE Format	50
7 Abbreviated Input file for Atmospheric Layering Associated with ITRA Microwave Comparison	59
8 Layer Specifications Resulting from the Input File of Table 7	61
9 Earthlimb Experiment Plans	68

1. INTRODUCTION

The Air Force Phillips Laboratory, Geophysics Directorate (PL/GP) has developed two extensively used radiative transfer codes: LOWTRAN (Kneizys et al., 1983) and FASCODE (Clough et al., 1981 and Smith et al., 1978). The current implementations of these codes are LOWTRAN 7 and FASCOD3, respectively. FASCODE is a computer code for the accelerated line-by-line calculation of spectral transmittance and radiance applicable from the microwave to the near ultraviolet (Clough et al., 1986). LOWTRAN is a computer code with a resolution of 20 cm^{-1} utilizing a one parameter band model. The two codes share extensive common elements including the spherical refractive geometry capability, the aerosol models, and the molecular continuum. For LOWTRAN 7 the molecular band model parameters have been obtained from FASCODE calculations using the 1986 HITRAN database (Rothman et al., 1987), significantly extending the compatibility between the two codes. Some differences exist, primarily as a consequence of the algorithms required to handle the molecular absorption. In particular, the multiple scattering is treated differently and capabilities such as non-local thermodynamic equilibrium (NLTE) that are dependent on temperature cannot be implemented in LOWTRAN since it is a single parameter model.

As effective as these models are, the user community requires more accurate radiative transfer calculations for even more complex environments. These requirements relate to atmospheric state definition, long path surveillance, radiative transfer in cloudy environments and improved capabilities for highly disturbed environments. This report describes the results of a program in advanced spectral modeling to address these increasingly stringent requirements. The approach taken in this program has been to improve model physics with improvements quantified and assessed by model validation. AER scientists have worked closely with Geophysics Directorate counterparts who provided technical direction and prioritization of relevant topics explored.

Although, as described above, the AFGL line-by-line code already possesses many of the attributes desired of a generally applicable transmittance/radiance simulation code, it lacks a number of desirable and potentially useful capabilities. These include the capabilities to: (a) accommodate the use of cross section data for transmittance calculations, (b) perform generalized multiple scattering calculations, (c) calculate both heating and dissociative fluxes, (d) provide radar and lidar backscatter coefficients, (e) incorporate surface reflection and emissivity effects including those of surface polarization on

atmospheric radiance calculations, (f) extend NLTE capabilities, (g) modify the isotopic ratio, and (h) perform Fourier transform/interferometer studies.

This report is subdivided into task specific subsections. The following section describes our general approach to address these technical issues (Section 2). Subsequent sections provide descriptions of work performed to accommodate new physics.

2. APPROACH

Advanced spectral modeling techniques are required to treat a variety of current topics in spectroscopy and radiative transfer relevant to the modeling of atmospheric transmission and radiance fields. As alluded to in the introductory section above, these topics include optimizing multiple scattering, surface properties, line coupling, line shapes, interferometric instrument function, and model validation. While the topics are varied, improvements in modeling these phenomena will enhance the integrated capability of Phillips Laboratory atmospheric transmission and radiance computer codes to be applied in support of DoD and other users. The approach which has been taken in this study has been to improve the simulation modeling physics of specified submodel areas (with prioritization guidance by the Phillips Laboratory) based on a process of continual model validation of results. By comparison of model output results to data, the integrated effect of individual submodel improvements is assessed in a manner consistent with that experienced by the user community. While appropriate data did not always exist to test improvements in specific submodel areas, our overall goal was to validate enhancements with real data.

3. CROSS SECTION DATA/LORENTZ CAPABILITY

There are applications in radiative transfer for which it is not possible or not feasible to perform exact calculations. An obvious case is the one for which spectral line parameters are not available. Another situation arises in which the spectral density of transitions is so high that, for efficiency, it may be desirable to replace the line-by-line calculation with available cross section spectra without serious loss of accuracy. The initial implementation of a module to incorporate the effects of absorption by heavy molecules into the advanced spectral model was accomplished with the cross section data from the 1986 HITRAN database. File four of the 1986 AFGL line compilation (Rothman et al., 1987) includes seventeen spectral cross sections for eleven molecular species. These cross section data from the 1986 HITRAN database were only available for a single temperature

and pressure and their application at other temperatures and pressures constituted an approach that could involve unacceptable error.

The 1992 HITRAN database includes cross section data at more than a single temperature for many of the heavy molecular species. The initial version of the cross section module has been extensively enhanced to adapt the cross section data to the thermodynamic conditions of the atmospheric layer for which the molecular optical depths are required. The treatment of the temperature dependence for the cross sections has been achieved by linearly interpolating to the specified layer temperature. Cross section data are provided at a variety of pressures, generally pressures substantially lower than atmospheric reference pressure (1013 mb) appropriate to the lowest part of the atmosphere. While it is not feasible to address the problem in which the cross section optical depths are required at pressures lower than that for which the data is provided, the case in which the optical depths are required at higher pressures can be addressed. Since many of the atmospheric effects of the heavy molecules occur at the lower altitudes it is desirable to have an approximate approach that provides an improved result at the higher pressures. This has been accomplished by assuming that the cross section data are collisionally broadened and that the average collision broadened halfwidth for all lines is 0.08 cm^{-1} at 1013 mb. The temperature dependence of this assumed halfwidth value has not been taken into account, a consideration for future enhancements. The line shape for collisional broadening is the Lorentz shape. We take advantage of the fact that a Lorentzian of width α_1 convolved with a Lorentzian of width α_2 results in a Lorentzian with width $\alpha_1 + \alpha_2$. This result can be readily established by considering the convolution in the Fourier domain. Utilizing the fact that the Fourier transform of the Lorentzian is an exponential and that in the Fourier domain the convolution operation is represented by a product, we obtain directly the result that the resulting function is a Lorentzian since the product of two exponentials is itself an exponential.

In cases for which the available cross section data have been extrapolated to zero pressure for application to stratospheric problems, the line shape appropriate to the data is taken to be the Doppler shape. The same procedure as previously described is utilized to obtain cross sections at the specified pressure. Although in principal this procedure is not rigorous in the sense of the convolution of Lorentzians, it is likely to be a reasonable approximation since for most cases of interest the Doppler width will be considerably narrower than the final Lorentz width. This result is a consequence of the fact that the convolution of a narrow Doppler shape with a broad Lorentzian is a Lorentzian to good

approximation. In the limit of an infinitely narrow Doppler line, i.e. a δ function, the procedure becomes rigorous.

To implement the approximate method for correcting the data to higher pressures, we first establish the mean halfwidth of the data as $0.08 * (P_C / P_O)$ where P_C is the pressure at which the data are provided and P_O is 1013 mb. The value of $0.08 \text{ cm}^{-1}/\text{atm}$ is chosen as representative of the molecular atmospheric pressure broadening coefficient. We next calculate the collisional halfwidth for the atmospheric layer for which the optical depths are required as $0.08 * (P_1 / P_O)$ where P_1 is the specified layer pressure. To correct the cross section data to the layer pressure, the data are convolved with a Lorentzian of width $0.08 * [(P_1 / P_O) - (P_C / P_O)]$ in which it is required that this be a positive quantity. A further constraint is imposed with respect to the sampling interval of the data: the sampling interval is specified as a fourth of the mean layer halfwidth. If this sampling interval is less than 10% greater than the sampling interval at which the cross section data are provided no convolution is performed.

In working with Laurence Rothman at PL/GP on the format for the cross sections, a determination was made that it would be advantageous to include in the header the minimum and maximum value of the cross section value in the related spectral cross section record. At an early stage of the calculation of the cross section contribution to each layer, the maximum value of the cross section value is utilized in conjunction with the appropriate column amount to determine whether the inclusion of a particular cross section set is required. The decision is made relative to the value of the minimum optical depth parameter (DPTMIN), an input parameter which prescribes the minimum optical depth contributions to be included in the optical depth calculation for the current layer.

To expedite the inclusion of cross section contributions into the layer optical depth calculations the following approach has been implemented: based on the sampling interval for the cross sections as prescribed by the considerations discussed above, the cross section contribution is added to the optical depths in the appropriate array R1, R2, R3 or R4 using the four point Lagrange interpolation method. The choice of the appropriate array is determined as that array whose spectral sampling interval (DV) has the closest smaller value to that of the cross section results. The incorporation of the cross section data into the FASCODE calculations has utilized concepts and modules that are already available in FASCODE. The largest task has been in interlinking the available modules and interfacing the data files.

Vertical profiles of mixing ratio (Jan., Apr., Jul., Oct.) at latitude 28N (chosen as representative of a global average) were provided from the 'AER 2d chemistry model' for the following trace gases for consideration for incorporation into the XAMNTS module of FASCODE: CCl_4 , CFC13, CFC13F3, ClONO_2 , N_2O_5 , HO_2NO_2 , HNO_3 . An example of the effect of the convolution method is given in Figures 1 and 2. Figure 1 provides the contribution of 3 cross section molecules to the transmittance for the lowest layer in a multilayer nadir case. In Figure 2 we have the result for the same case as Figure 1 except that the convolution has been performed to provide a result consistent with the pressure of the layer. The spectra are attributable to CCl_4 at 790 cm^{-1} , CFC11 at 850 cm^{-1} and CFC12 at 925 cm^{-1} . The pressures at which the cross section data are provided are 0.453 mb for CCl_4 , 0.0933 mb for CFC11, and 0.266 mb for CFC12. The pressure of the atmospheric layer is 975 mb. Results of validations with HIS observations which include the effects of these heavy molecules have been generally favorable.

4. ATMOSPHERIC MULTIPLE SCATTERING

Preliminary studies of the implementation of the multiple scattering option in the AFGL spectral modeling codes (LOWTRAN, MODTRAN) has suggested some deficiencies in the current treatment. The current PL/GP band model for LOWTRAN treats multiple scattering through the use of a two-stream approximation to the radiative transfer equation, incorporating gaseous absorption with an exponential sum or k-distribution technique (Isaacs et al., 1987). This treatment is perhaps the most efficient one possible to handle multiple scattering, but it does break down in some regimes.

First, it was recognized that the approach as implemented did not explicitly treat cases in which earth sphericity was a factor, i.e. when the solar zenith angle cosine approached and exceeded 90° . Secondly, it was desired to provide an alternate high accuracy approach which directly incorporated the capability of a multistream multiple scattering model. Both these enhancements are described below.

4.1 Large Solar Zenith Angle Scattering

The multiple scattering approximation implemented in LOWTRAN and MODTRAN is based on the assumption of plane parallelism. The computational manifestation of this assumption is the appearance of the secant or inverse cosine air mass factor which is used

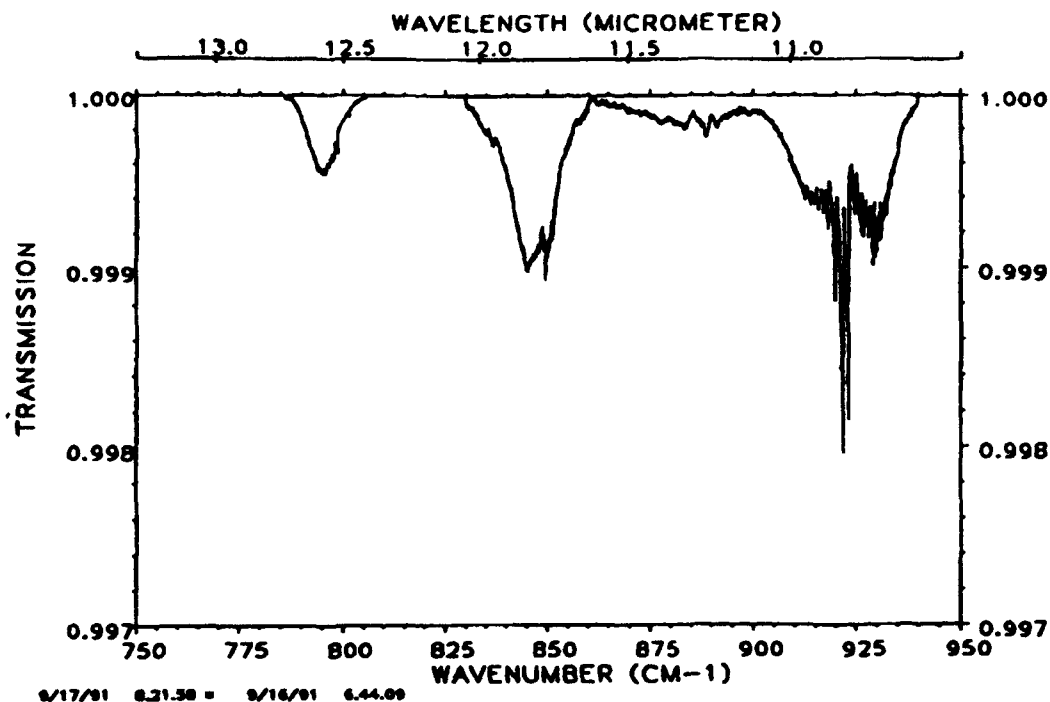


Figure 1. The contribution of CCl_4 (790 cm^{-1}), CFC11 (850 cm^{-1}) and CFC12 (925 cm^{-1}) to the transmittance of an atmospheric layer at 975 mb.

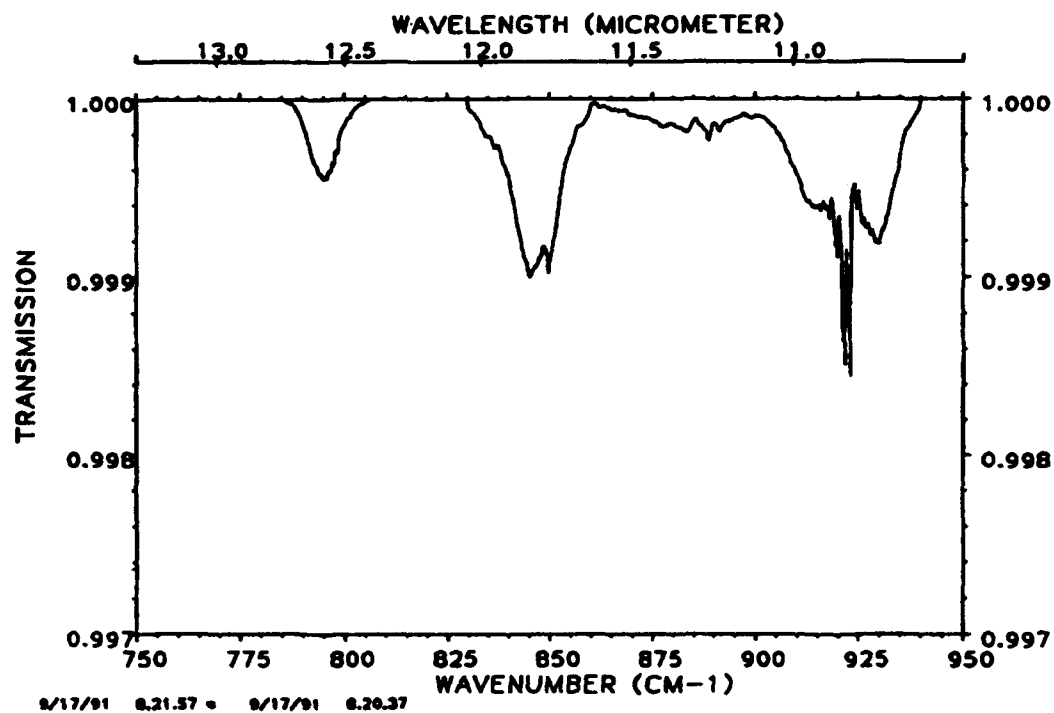


Figure 2. The transmittance of the same layer as Figure 1 except that the spectral cross section data have been convolved with a Lorentzian to account for the effect of atmospheric pressure broadening.

to convert between vertical optical path quantities and slant path optical properties. This assumption is used extensively in the calculation of the two stream equations which provide the approximation of scattered intensities for the multiple scattering source function.

A simple approach to treating the spherical geometry of high zenith angle, i.e. low sun cases, with respect to multiple scattering of solar radiation, recognizes that the primary solar scattering source function can be defined by evaluating the attenuation of the direct solar beam over the exact refracted path. The primary solar scattering source function is then calculated exactly as it is in the single scattering option, by replacing the secant of the SZA (solar zenith angle) as the air mass factor with the ratio of the actual refracted path optical thickness to the vertical path optical thickness for each layer. This eliminates the artificial singularity at the horizon (solar zenith angle of 90 degrees) and produces a realistic source function which degrades monotonically to zero.

Physically, the multiple scattering calculation uses the exact primary source function evaluated for the spherical atmosphere, but then assumes plane parallelism for the calculation of the multiple scattered contributions to path radiance. We call this the locally plane parallel approximation.

The approach we have adopted to implementing this enhancement is the following:

- Working with GL personnel, we identified the refracted path optical thickness for the solar path and the vertical path optical thickness corresponding to this path for each layer. The ratio of the former to the latter was defined as the air mass factor.
- The reciprocal of the air mass factor thus derived was defined as the effective solar zenith angle cosine for the multiple scattering approximation. This quantity has the following properties: (a) no singularity at 90 degrees, (b) it is not symmetric about 90 degrees, (c) it decreases monotonically but never reaches zero.
- Radiances were calculated as a function of SZA for a downward looking path originating at 30 km at $10,000 \text{ cm}^{-1}$ (assuming zero surface albedo). These are shown in Figure 3.

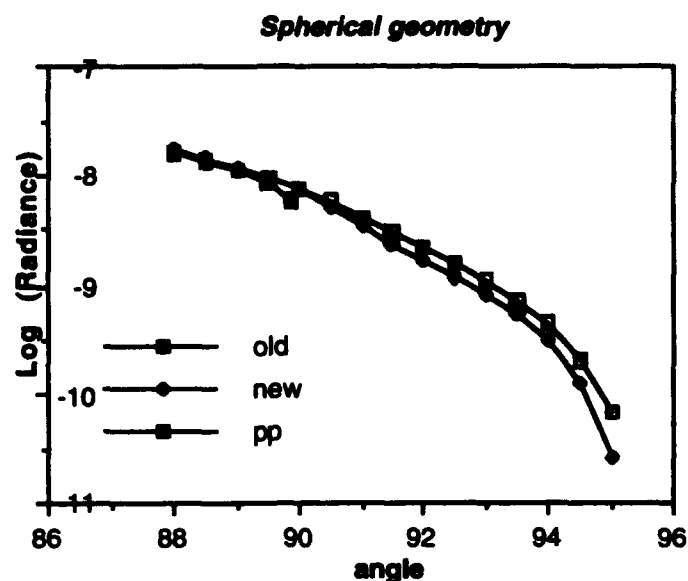


Figure 3. Multiple scattering "quick fix".

In the previous plane parallel (pp) formalism there was a singularity at a SZA of 90 degrees. A GL fix [denoted old(89)] constrained this angle so that it was symmetric about 90 degrees with the SZA fixed at 89 degrees for angles from 89 up to 91 degrees and so that the airmass factor [here defined as $1/\cos(\text{SZA})$] was positive definite for angles greater than 91 degrees.

It is seen that the pp approach blows up at 90 degrees as expected and the radiance is underestimated due to using the reciprocal of the cosine at large angles which underestimates the primary source function. The GL fix [old(89)] overestimates the radiance due to fixing the SZA at 89 degrees. The new approach is well behaved.

Calculations were also done to compare the results of this treatment for large zenith angles within the approximations used in MODTRAN and LOWTRAN to exact results from application of the discrete ordinate method (DOM). This comparison was facilitated by the LOWTRAN/DOM interface described in the following section (Section 4.2). Results of this comparison are shown in Figure 4. These include: (a) the new treatment and DOM results using (b) two and (c) eight streams, respectively. The figure illustrates that the new treatment is consistent with the eight stream DOM results for all solar zenith

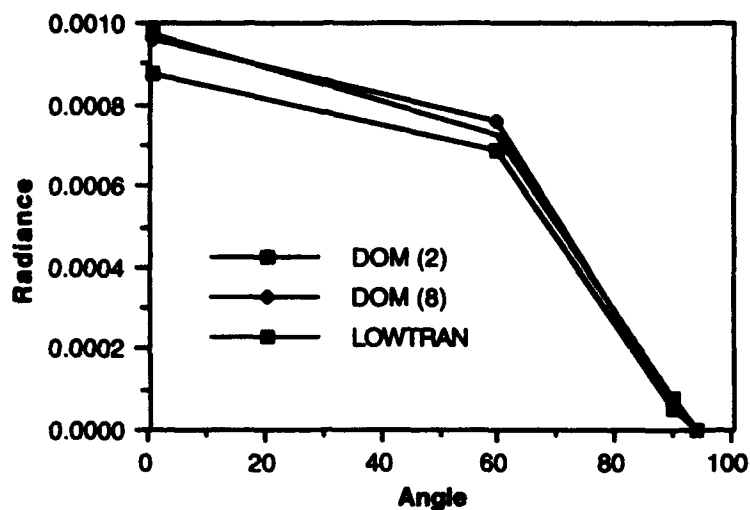


Figure 4. Multiple scattering "quick fix": comparison to DOM.

angles. It can be seen that over the range from over head sun to sun at the horizon (SZA=0, 90), the LOWTRAN approximation (although a two stream approach) gives a better fit to the eight stream DOM results than to the DOM two stream. This is because the DOM and LOWTRAN two stream approximations are inherently quite different. In fact, the LOWTRAN two stream solution (a hybrid modified delta-Eddington approximation) was selected specifically for its better fit to exact multiple scattering results.

The same improvements suggested here for LOWTRAN can be applied to the moderate resolution model MODTRAN.

In modifying LOWTRAN 7 to correctly calculate the large solar zenith case, one goal was to minimize the changes necessary so that any forth-coming errata would be as simple as possible. With this in mind, all changes to LOWTRAN were constrained to the subroutine FLXADD. In this routine the variable CSZEN is redefined to be the ratio of the refracted path optical thickness to the vertical path optical thickness. This required the addition of twenty-three lines of code to FLXADD.

Other changes which should be considered, but which were not implemented are:

- 1) remove the GL fix in routine LWTRN7 which constrains CSZEN to 89 degrees (not currently a problem since CSZEN is reset in FLXADD to correct value).
- 2) remove references to CSZEN in routine SSGEO since this calculation of CSZEN is no longer necessary.

An updated version of FLXADD has been made available to PL/GP.

4.2 "Exact" Multiple Scattering

A particular deficiency of the multiple scattering approximation is the two stream approach. At the time of its development an accuracy of 20% in radiance was deemed acceptable. Subsequently, user requirements have driven the need for more accurate scattered radiance fields, particularly for the calculation of backgrounds. The most dramatic improvement of multiple scattering accuracy would come about by changing from a two-stream approximation to a multiple stream scattering model. There are two approaches to the multiple stream multiple scattering problem that have significant and complimentary advantages. The adding-doubling method is highly accurate and is fast for applications in which the spectral radiance at a specific atmospheric level is required. For applications in which the radiative transfer result is required for the full atmosphere, net fluxes and heating/cooling rates, and for which the number of spectral points is not extremely large, LOWTRAN resolution, the discrete ordinate method (DOM) offers some distinct advantages.

An efficient, accurate, and well tested DOM code has recently become available (Stamnes and Conklin, 1984). The number of streams can be selected by the user to be anywhere from 2 to 64, depending on the problem the user is interested in. In the two-stream mode the code would behave as the one currently in LOWTRAN, although it would be a bit quicker. The accuracy increases markedly as the number of streams increases, but so does the computation time. Four streams is easily a factor of 2 or 3 more accurate than two streams, while eight streams is easily an order of magnitude more accurate. Furthermore, the need for a diffusivity factor disappears when a multi-stream approach is used, removing another approximation. The multiple stream code would be particularly helpful

for solar or lidar cases, and is essential if one wishes to expand LOWTRAN's capabilities to include dusty and cloudy atmospheres.

The approach to provide an "exact" multiple scattering capability with LOWTRAN which introduced minimal program impacts was to link the LOWTRAN and DOM codes. To accomplish the required connectivity between the LOWTRAN atmospheric profile optical properties and the DOM code, an interface routine is provided. This is illustrated in Figure 5.

LOWTRAN was modified by adding approximately sixty lines of code, consisting mostly of write statements into the body of routines LWTRN7 and TRANS. This modified version of LOWTRAN produces an additional output file which is read in by the DOM interface code DOMLOW. The following information is provided to DOMLOW from LOWTRAN for each frequency:

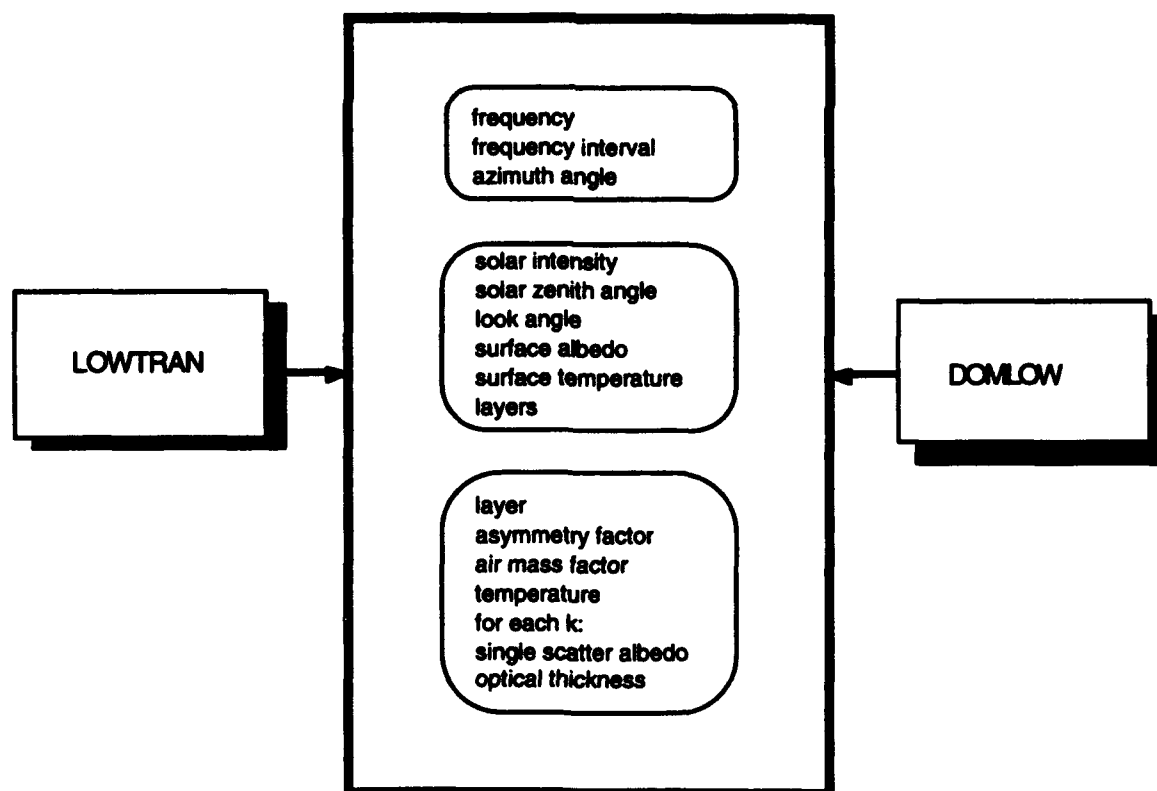


Figure 5. Interface routine.

- frequency, wavelength and bounds for current frequency interval.
- azimuth angle, solar intensity at top of atmosphere, solar zenith angle at surface, cosine of theta (look angle), surface albedo, surface temperature and number of layers.
- profile of asymmetry factors at every layer, the effective air mass factor (ratio of refracted path optical thickness to vertical path optical thickness) and the layer edge temperatures.
- profiles of single scattering albedo and optical thickness for each layer and value of k.

User selection of atmospheric model follows from LOWTRAN. The interface routine reads in the output file described above, and calls the DOM subroutine.

DOMLOW has been made available to PL/GP.

5. HEATING RATES AND FLUXES

The capabilities in the present PL/GP line-by-line model extend to providing users with two fundamental radiative properties of atmospheric paths, namely transmittance and radiance. Another derived quantity of interest to atmospheric modelers is the flux profile, F , associated with atmospheric heating. The upward and downward flux profiles are defined as:

$$F^{\pm}(v, \tau) = \int_0^1 \mu I(v, \tau, \pm\mu) d\mu$$

while the net flux is given simply by:

$$F(v, \tau) = \int \mu I(v, \tau, \mu) d\mu = F^{+} - F^{-}$$

here I is the frequency dependent, azimuthally averaged radiance field, τ is the optical thickness which can be related to atmospheric level, and μ is the direction cosine. Heating rates are obtained by differentiating the net flux with respect to an appropriate path parameter such as height, i.e. the heating, $h(z)$, would be proportional to:

$$h(z) \propto \frac{dF(v, \tau)}{d\tau} \frac{d\tau}{dz}$$

The development of the capability to obtain fluxes and heating rates for advanced spectral modeling has been performed in conjunction with support from DOE. The effort has involved three aspects: (1) the development of an improved algorithm to calculate radiances for a vertically inhomogeneous layer; (2) modifications to the line-by-line radiative transfer model (FASCODE) to provide the necessary intermediate radiance results including an appropriate spectral averaging method; and (3) an algorithm to compute the fluxes and heating rates from the intermediate radiances. The implementation and validation of the improved radiance algorithm was accomplished through the support of the current contract.

An important problem in atmospheric radiative transfer is the treatment of vertical inhomogeneity, particularly with respect to the treatment of the variation of the Planck function in the inhomogeneous layer. This is a particularly important issue in the calculation of cooling/heating rates which involves the calculation of the flux divergence. A method has been developed which has gained general acceptance in the field of radiative transfer to address the problem of the vertical inhomogeneity of the temperature field. It is called the 'linear in tau method' from the assumption that the Planck function varies linearly from a value appropriate to the level boundary in the direction of the radiation (optically thick limit) to one appropriate to an average for the layer (optically thin limit). This approach was considered by us to have had a number of limitations: (1) the associated algorithm is computationally expensive; (2) the result involves a division by the optical depth requiring the definition of a strong and weak regime; (3) there is no mechanism to account for the variation of the optical depth in the path (i.e. the exponential atmosphere); and (4) it was not initially obvious how to accommodate a value of the Planck function in the thin limit that deviated from the average Planck function for the layer. An algorithm has been developed which is designed to avoid some of these problems and has the advantage of being computationally fast.

The algorithm for the radiance from a layer, R , in which the Planck function varies along the optical path in the layer, is given in our approximation by the relation:

$$R = [\bar{B} + (\alpha\tau) B_u] \cdot (1 + \alpha\tau)^{-1} \cdot (1 - T)$$

where \bar{B} is the Planck function appropriate to the optically thin limit, B is the Planck function associated with the layer boundary in the direction of the radiance, τ is the optical depth of the layer, T is the associated transmittance, and all quantities are to be taken at the

monochromatic frequency of the calculation. The parameter a in this Padé approximation has been obtained empirically from studying a number of zenith, nadir and limb simulations. A value for the constant a of 0.20 provides a significantly improved result over an algorithm that does not take into account the vertical inhomogeneity of the temperature field. Figure 6 indicates the spectral radiance in equivalent brightness temperature in a representative spectral region from 740 cm^{-1} to 742 cm^{-1} for a simulated limb calculation. The reference calculation has been obtained by dividing the limb layer into five sub-layers and utilizing the new algorithm in the calculation. Figure 7 demonstrates the error obtained when the limb layer is treated as a single isothermal layer at the path weighted temperature of the layer. Figure 8 demonstrates the error when the limb layer is treated as a single layer and the new algorithm for radiance is utilized. It should be emphasized that in the optically thick limit the new algorithm provides correct radiance values at the layer boundaries. This is essential to ensure that in this limit the net flux at the boundaries is zero, resulting in no net heating or cooling. The algorithm for calculating fluxes has been made available at PL/GP on file FLUXF/UN=ISAACS. We are indebted to Gail Anderson and Frank

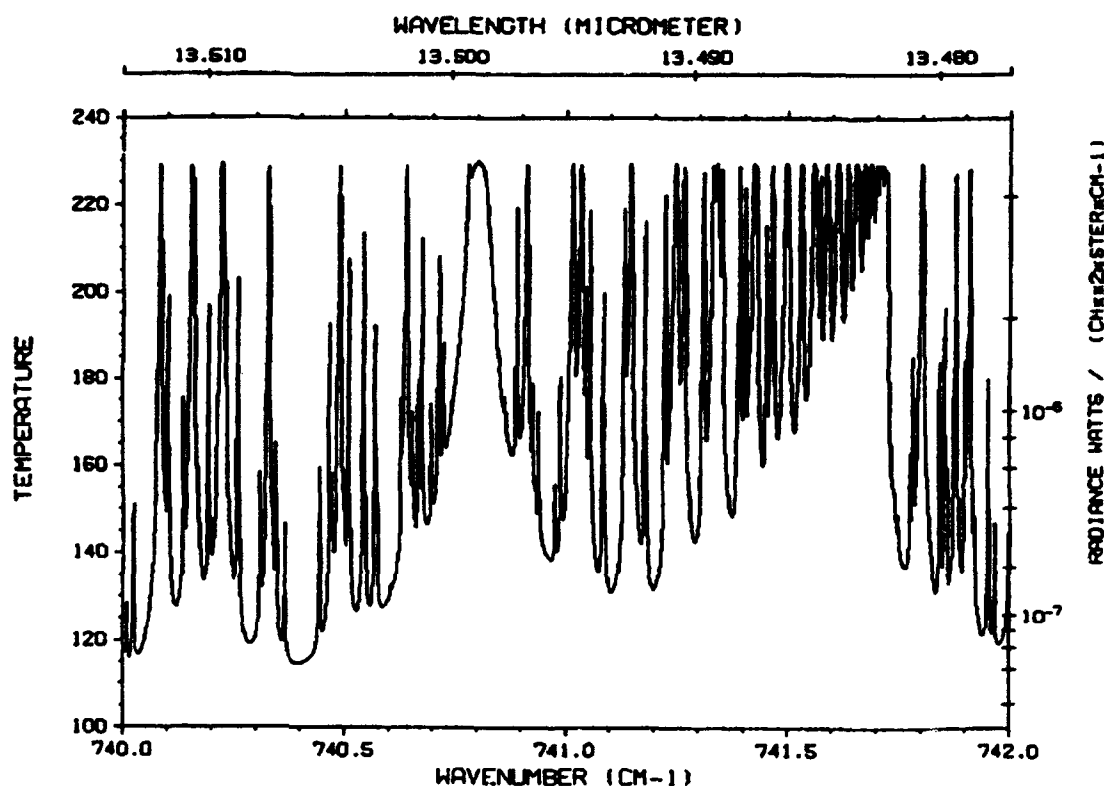


Figure 6. Limb layer radiance spectrum utilized for development of the improved radiance algorithm. The units are equivalent brightness temperature.

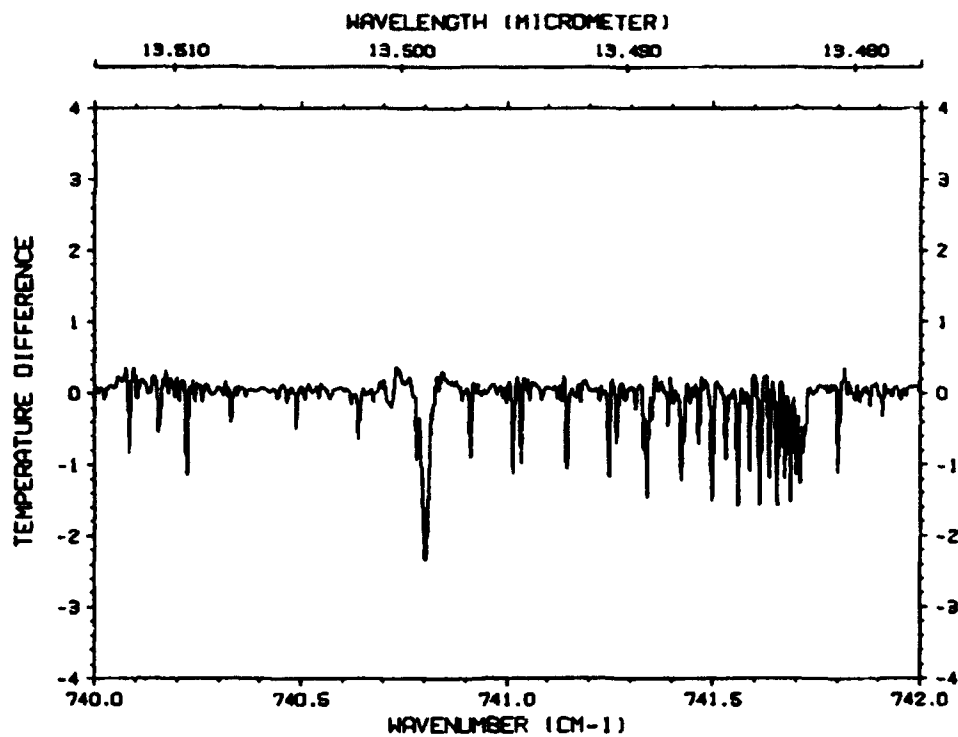


Figure 7. Radiance error in equivalent brightness temperature due to treatment of the layer as isothermal.

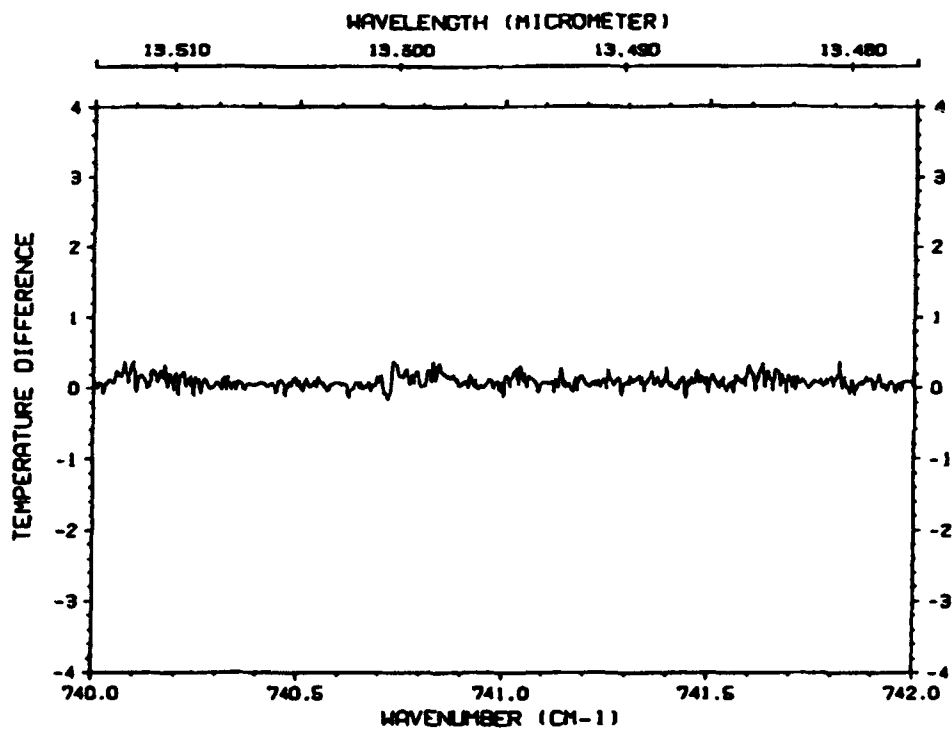


Figure 8. Radiance error utilizing the improved radiance algorithm.

Kneizys for discussions leading to an appropriate treatment in the optically thin limit. In the final analysis our concerns with the linear in tau method may have been greater than appropriate and with judicious coding this approach may ultimately prove preferable.

The strategy implemented for computing fluxes is as follows: (1) the line-by-line calculation of optical depths for the nadir is performed and the results retained for subsequent utilization; (2) the radiances are calculated using these spectral optical depths multiplied by the reciprocal of the direction cosine associated with the angle for which the radiance is required; (3) the monochromatic radiances are spectrally degraded at each layer to reduce storage and data handling requirements; and (4) the fluxes are obtained from the upwelling and downwelling degraded spectral radiances to provide the up- and downwelling fluxes. New radiance algorithms are provided for this calculation due to the necessity to merge from the top of the atmosphere down for the downwelling radiances and from the bottom to the top for the upwelling radiances. First moment gaussian quadrature is utilized for the flux calculation. For the clear sky no more than three first moment quadrature points are required. Table 1 provides the direction cosine values, quadrature weights and the anticipated error for quadratures up to three. Finally, a post-processing program, RADSUM, has been developed for obtaining flux and heating rate results at the desired atmospheric levels.

Table 1. First Moment Quadrature Direction Cosine Values, Weights and Representative Flux Errors

number of quadrature points	direction cosine	weight	% error in flux	
			up	down
1	0.66667	0.5	0.7	-4.5
2	0.35505	0.18196	0.05	-0.58
	0.84495	0.31804		
3	0.21234	0.06983	0.007	-0.063
	0.59053	0.22924		
	0.91141	0.20093		

6. SCATTERING PROPERTIES OF PRECIPITATION

Radar backscatter is derivable from a knowledge of the precipitation scattering properties. Precipitation scattering properties including the extinction coefficient, single scattering albedo, and the angular scattering function are generally available via standard Mie theory calculations. Radar backscatter is simply calculated from the angular scattering functional scattering coefficient. The Mie theory formalism requires a knowledge of particle size distribution and index of refraction. The index of refraction, in turn, is dependent on frequency, phase (i.e. ice or water), and temperature. To avoid the cumbersome necessity of performing on-line Mie theory calculations to support each possible combination of these model variables within multiple scenario brightness temperature simulations, a parameterization has been developed based on the existing Mie theory calculations of Savage (1978). This parameterization is available for implementation within LOWTRAN/FASCODE. The attributes of the precipitation property modeling subroutine are described in a paper by Isaacs et al. (1988).

The resultant subroutine provides an efficient method to obtain the extinction coefficients, single scattering albedo, and angular scattering function over the frequency domain from 19 to 240 ghz. The angular scattering function is given in terms of its first eight Legendre polynomial expansion coefficients. Precipitation angular scattering functions are not highly anisotropic at microwave frequencies and this number of terms usually suffices to describe them. Furthermore, this number of terms is consistent with the Gaussian quadrature required to specify the brightness temperature field (Savage, 1978). The scattering function asymmetry factor used in standard multiple scattering approximations is easily obtained from a knowledge of the second Legendre coefficient. Figure 9 from Isaacs et al. (1988) illustrates the first eight Legendre polynomial coefficients of a Marshall-Palmer size distribution with a rainfall rate of 5 mmh^{-1} at four frequencies and compares exact values with those from the subroutine interpolation. Calculation of radar backscatter from the optical data extracted above proceeds from the following equation (McCartney, 1976):

$$\beta(\pi) = \frac{\beta_s}{4\pi} P(\pi) \quad (\text{cm}^{-1} \text{sr}^{-1})$$

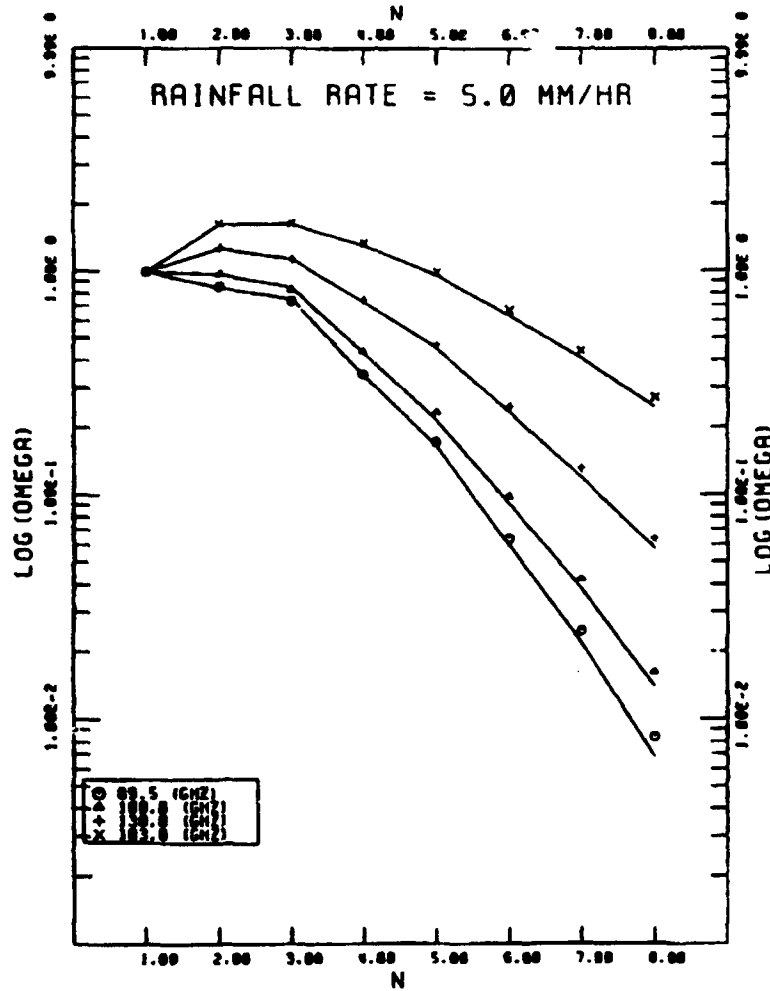


Figure 9. Legendre polynomial coefficients of a Marshall-Palmer size distribution with a rainfall rate of 5 mmh⁻¹ at four frequencies.

The angular scattering coefficient, $P(\pi)$, is evaluated by summing over the first eight Legendre polynomials, $P_l(\theta)$, using the extracted coefficients, W_l , and evaluating them at an angle of π , i.e.

$$P(\pi) = \sum_{l=1}^8 W_l P_l(\pi)$$

We have modified the algorithm described in Isaacs et al. (1989) to provide the precipitation angular scattering function from its Legendre polynomial decomposition and to evaluate the backscatter. This can be integrated into the advanced spectral modeling codes as an enhancement.

7. SURFACE PROPERTIES

The radiometric properties of the earth's surface determine both backgrounds against which atmospheric targets are observed by air and spaceborne sensors and the radiance distribution of the sky background observed from surface and in situ sensors. The role of surface properties in passive radiative transfer is illustrated by the comprehensive boundary contributions to upward radiance solutions given in Table 2.

In these equations, a general source function (i.e. either solar or thermal or both) is implied and $\epsilon(\nu)$ is the frequency dependent, surface emissivity. Equivalently, these expressions could be written in terms of the surface reflectivity, $r(\nu)$, which is unity minus the emissivity. Currently, LOWTRAN allows the user to specify a gray (i.e. constant with frequency) surface emissivity value which is used to calculate surface emission for downward looking paths which terminate at the earth's surface. There is no provision to treat spectral dependence of the surface emission. Furthermore, there is no internal data file of typical spectral reflectances for generic geophysical surfaces from which the user can select appropriate path termination properties. Finally, we note that users interested in passive microwave sensors or signals returned from the surface by reflection of lasers at visible and near infrared wavelengths require the capability to treat polarization.

For enhanced spectral models, the treatment of surface reflection, emission, and polarization properties is described. At visible and near infrared wavelengths, we have reviewed the literature to provide surface reflection models for our remote sensing studies which are applicable to generic geophysical surfaces such as the ocean, land, vegetation, and snow. We have modified LOWTRAN to address these surfaces with a user specified input selection. The reflectivity is a function of wavelength for the domain of data provided. At microwave frequencies, we provide a set of algorithms to evaluate surface emissivity. This can be used as an adjunct to the advanced spectral models. Due to the complexity of the resulting radiative transfer calculation (i.e. when scattering and polarization occur) these have not been integrated into the advanced spectral models. This capability is provided by the enhanced RADTRAN code (Isaacs et al., 1989a).

7.1 Visible and Near IR Surface Reflection

Albedo spectra were gathered representing new snow and old granular snow (Warren and Wiscombe, 1980; Wiscombe and Warren, 1980) a plowed field

Table 2. Radiative Source Functions. Forms of Boundary, $R_i(P_b)$, and Atmospheric, $S(p)$, Contributions to Sensor-incident Radiances, $R_i(\theta)$.

	Spectral Region	Boundary, $R_i(p_b)$	Atmospheric, $S(p)$
[1]	Ultraviolet/visible ($\lambda < 0.7\mu m$)	$\pi F_i \rho_i(\Omega_s) \tau_i(\theta_s, P_s)$	$\omega_i(p) J_i(p, \Omega)$
[2]	Near infrared ($0.7 < \lambda < 4.0\mu m$)	$\pi F_i \rho_i(\Omega) \tau_i(\theta_s, P_s)$ + $\epsilon_i B_i[T(p_s)]$ + $(1 - \epsilon_i) R_i \downarrow(p_s)$	$[1 - \omega_i(p)] B_i[T(p)]$ + $\omega_i(p) J_i(p, \Omega)$ (note 1)
[3]	Infrared ($4.0 < \lambda < 100\mu m$)	$\epsilon_i B_i[T(p_s)]$ + $(1 - \epsilon_i) R_i \downarrow(p_s)$	$B_i[T(p)]$ (note 2)
[4]	Millimeter/microwave ($\lambda < 100\mu m$)	$\epsilon_i B_i[T(p_s)]$ + $(1 - \epsilon_i) R_i \downarrow(p_s)$ (note 3)	$[1 - \omega_i(p)] B_i[T(p)]$ + $\omega_i(p) J_i(p, \Omega)$

Legend

F_i	solar irradiance
ρ_i	bidirectional reflectance of surface
Ω_s, θ_s	sun/sensor reflection angle, solar zenith angle
ϵ_i	surface emissivity
ω_i	single scattering albedo
$R_i \downarrow$	downward atmospheric flux
B_i	planck function (thermal source function)
$J(p, \Omega)$	scattering source function for scattering angle Ω

Notes:

- (1) Assumes scattering by aerosol or cloud
- (2) Assumes no scattering; if scattering, same as (1)
- (3) Assumes scattering by precipitation; if no scattering, same as (2)

(Eaton and Dirmhirn, 1979), green vegetation (Eaton and Dirmhirn, 1979), and smooth ocean surfaces (Curran, 1971; Sidran, 1981). Figure 10 illustrates these reflectance spectra in the wavelength range between 0.4 and 2.0 μm (5,000 to 25,000 cm^{-1}). These curves, illustrated in Figure 10, were chosen as characteristic of each surface type, although there is a great deal of variation within each type based on their differing compositions and local climates. For example, the ocean albedos change with surface conditions which effect wave spectra, white cap coverage, and amount of sea foam.

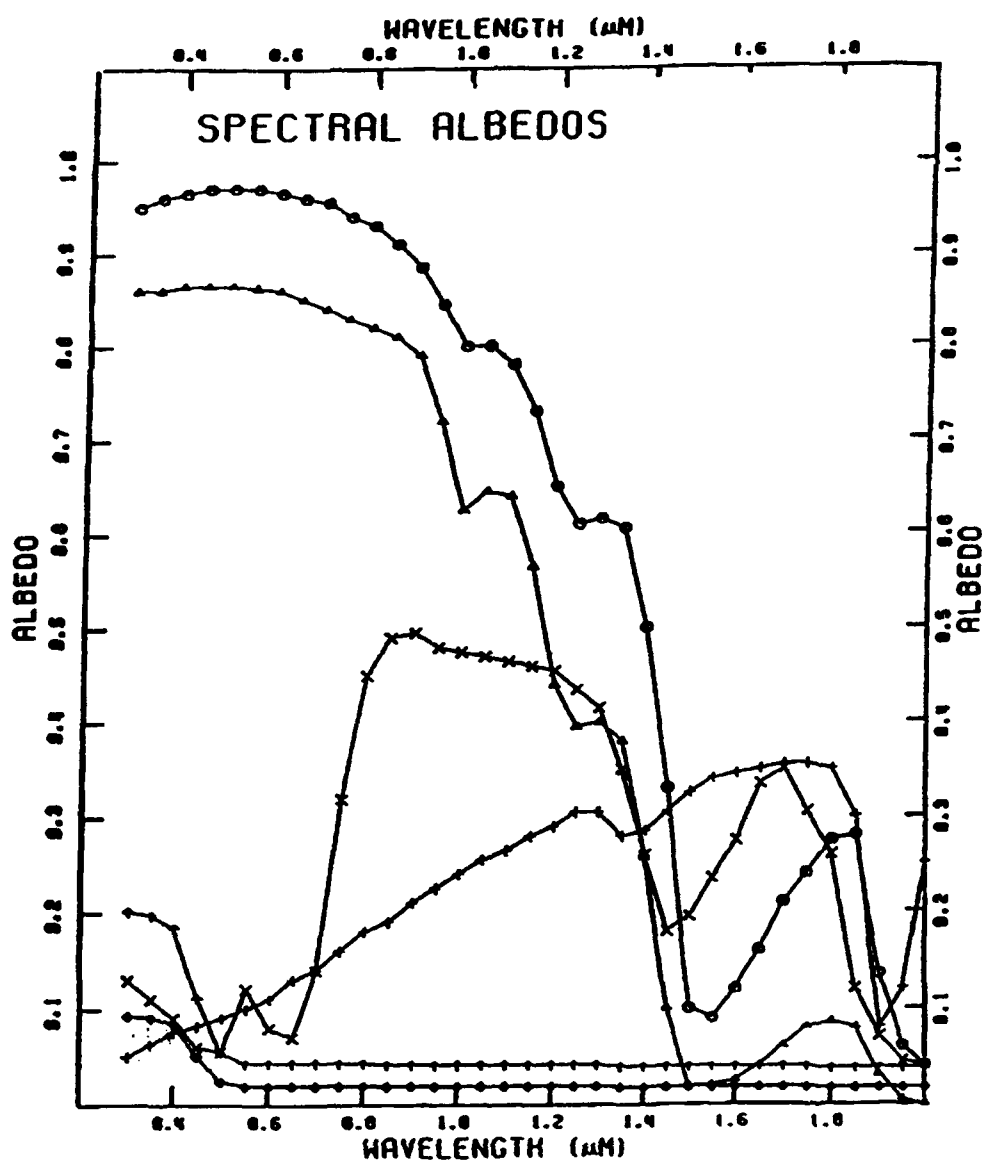


Figure 10. Spectral albedos for different surface types. Curves are given for new snow (©), old snow (Δ), a plowed field of clay loam (+), green plants (x), and a smooth ocean at solar zenith angles of 0° (\diamond) and 55° (\uparrow).

The main features to note are that snow has a very large albedo at visible wavelengths ($0.4 \leq \lambda \leq 0.7 \mu\text{m}$), but quickly drops off in the near infrared region ($0.7 \leq \lambda \leq 3 \mu\text{m}$) due to the absorption characteristics of water. The plowed field albedo is much lower in the visible but gradually rises with wavelength to exceed the snow's albedo in the near infrared. The green vegetation curve has a pronounced plateau between 0.7 and $1.3 \mu\text{m}$, and the ocean albedos are comparatively low for all wavelengths.

The LOWTRAN code was modified to use these spectra at visible and near infrared wavelengths (Isaacs and Vogelmann, 1988). To implement these spectra, the simplifying assumption was made that the surface behaved as a Lambertian reflector. This means that the special case of sunglint (specular reflection) was not treated. The ocean's albedo, which depends on the solar zenith angle, was modeled out to 55° using a fit of detailed calculations (Sidran, 1981). Angles greater than this are reset to 55° which will underestimate the albedo at extreme solar zenith angles. An example of LOWTRAN calculations using these albedos and the clear sky model is provided in Figure 11, illustrating how these different surface properties are manifested in the reflected spectrum.

7.2 Microwave Surface Emissivities

A set of microwave surface emission models which can provide frequency-dependent, polarized surface emissivity calculations for a variety of geophysical surfaces has already been developed at AER (Isaacs et al., 1987b). The selection of a simple surface modeling approach is made difficult by the complexity of geophysical surfaces. For example, homogeneous dielectric slab models for both land and ocean have been commonly used to provide the required surface emissivity parameters to initiate brightness temperature simulation calculations. It is apparent from an examination of recent microwave satellite imagery that such approaches cannot reproduce the fidelity of the complex fields of observed surface properties. This is due to the neglect of important physical mechanisms such as scattering by such approaches, and their failure to treat the spatial inhomogeneities in dielectric properties due to the inherent physical structures of real surfaces. On the other hand, it is necessary to consider the computational level of effort required to model all of the physics, even if it were well understood.

Related to the choice of an appropriate model is the detail of surface type characterization desired, i.e. how many surface types to treat. In reality, of course, there is a continuum of geophysical surface types. A sufficiently general model can attempt to

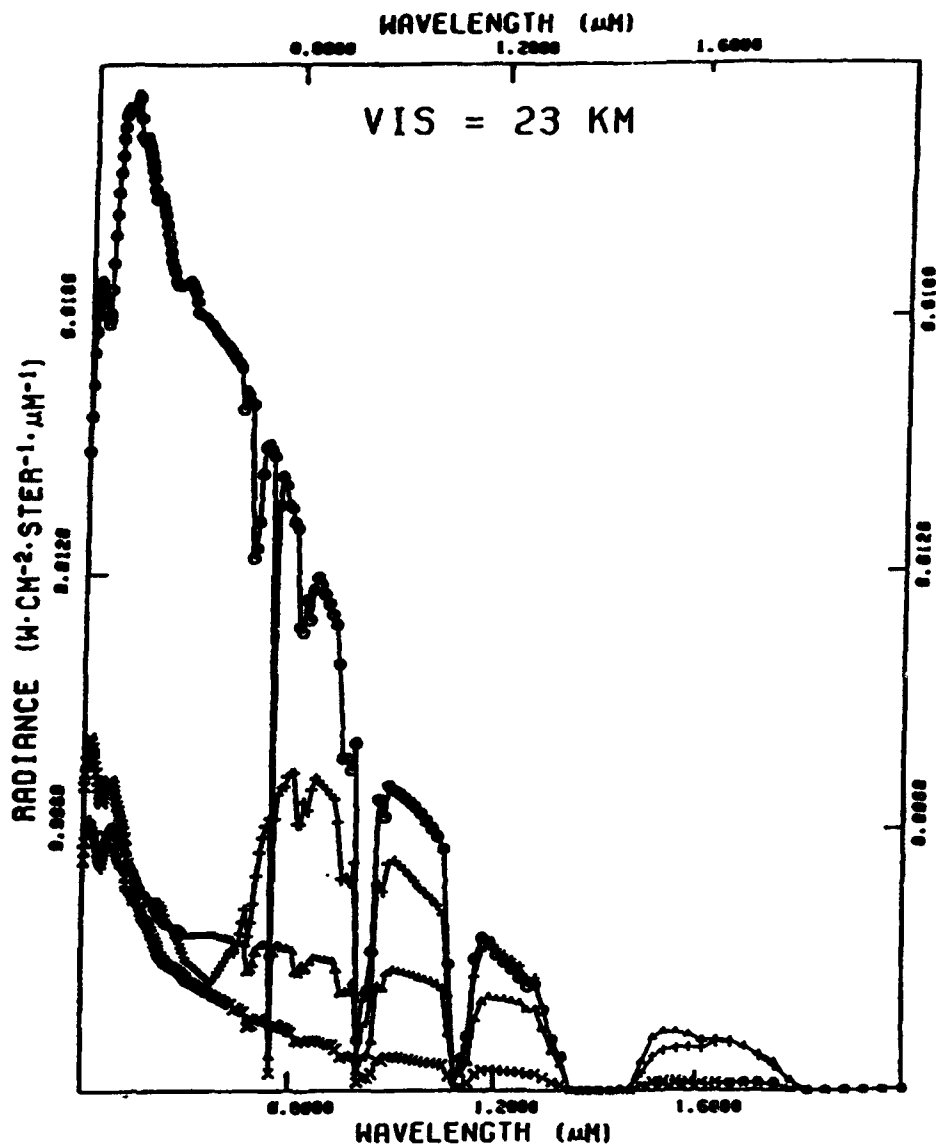


Figure 11. LOWTRAN radiance calculations with surface albedos in Figure 10.

simulate some of the behavior exhibited by subsets of surface types within this continuum by choosing appropriate parameterizations of relevant surface properties and varying them within representative ranges. The choice of surface types employed within the surface modeling package was based both on the desire to treat a comprehensive set of surfaces and, to some extent, on the requirements of potential model users with specific surface related simulation applications. The surface types selected are: (a) calm and rough ocean, (b) first year (FY) and multiyear (MY) sea ice, (c) wet and dry snow over land, (d) moist soil, (e) vegetation, and (f) land. The land surface type provides a background for snow, soil, and vegetation models in addition to its potential role as a distinct surface type itself.

A menu will be provided to select from among the available surface type choices. Surface types are summarized in Table 3.

Both the calm ocean and land are modeled as simple dielectric slabs. The other surface types, however, clearly require a more sophisticated modeling treatment. As the following discussion will indicate, it is not appropriate to treat all of the surface types delineated above by a single formalism. Therefore, two distinct approaches have been applied in the development of these surface emission models: that based on wave theory for random discrete scatterers and that based on radiative transfer theory for continuous random media. The former approach is applied to modeling the ocean surface, sea ice, and snow, while the latter is applied to both soil and vegetation. These approaches are also summarized in Table 3.

Table 3. Surface Model Types and Modeling Approaches

Model	Surface Type	Modeling Approach
1	Calm ocean	Dielectric slab
2	Rough ocean	Random discrete scatterers
3	FY sea ice	Random discrete scatterers
4	MY sea ice	Random discrete scatterers
5	Dry snow	Random discrete scatterers
6	Wet snow	Random discrete scatterers
7	Vegetation	Continuous random medium ($M_v=0.5$, $D=200$)
8	Vegetation	Continuous random medium ($M_v=0.3$, $D=100$)
9	Vegetation	Continuous random medium ($M_v=0.2$, $D=50$)
10	Vegetation	Continuous random medium ($M_v=0.1$, $D=10$)
11	Dry Soil	Continuous random medium ($M_v=0.1$, $D=50$)
12	Wet Soil	Continuous random medium ($M_v=0.5$, $D=50$)

In the wave theory approach for random discrete scatterers, one or more layers is defined consisting of a dielectric medium with either uniform properties or containing a random distribution of discrete dielectric spheres with distinct dielectric properties. These latter inclusions give the medium scattering properties which by appropriate choice of the background and inclusion permittivities can be tuned to exhibit the observed behavior of sea ice and dry snow, for example. The radiative transfer approach for continuous random media models the surface from a different perspective. Some surfaces are spatially

inhomogeneous in their dielectric properties, yet the inhomogeneities are not due to discrete spherical scatterers. The approach provides an alternative treatment in which the permittivity is varied continuously throughout the medium. Furthermore, these spatial variations are parameterized in such a manner that the relative effects of variations in the vertical and horizontal physical structure of the medium can be modeled. These surface emissivity models are summarized in a recent journal article (Isaacs et al., 1989b).

Figure 12 illustrates surface emissivities calculated for the models in Table 3 at frequencies of 1.2, 5.0, 10.6, 18.0, and 35 ghz for a look angle of 54 degrees.

8. ISOTOPIC RATIOS

The HITRAN database accounts for isotopic abundance by including the fractional abundance in the line strengths. The isotopic abundances are specified on a file associated with the HITRAN database. With the inclusion of isotopic partition function data with the HITRAN database, the advanced spectral model has been modified to correctly describe the strength variation with temperature for the relevant isotopic species. An individual isotopic species of interest is essentially treated as a separate molecule. For some atmospheric applications, e.g. altitude dependent photodissociation of isotopic species, it would be desirable to provide an option for treating variation of isotopic ratios in the radiative calculation. This capability is only partially implemented in the model in the sense that a mechanism is not currently available to input mixing ratio profiles for individual isotopic species of interest. This option could be readily implemented once an approach is established to provide the necessary but potentially extensive input data.

A copy of the Total Internal Partition Sums program (TIPS) was received from R. Gamache, Gamache et al., 1990. A modified version of this partition function program was incorporated into subroutine MOLEC. The capability to utilize the results from TIPS and correctly treat the molecular isotopes was incorporated into LNFL, HIRAC1, LNCOR1 and LINF4. On comparing the results of the new model with those from the previous version, significant divergence was encountered at temperatures greater than 400 K. After some study and discussions with R. Gamache it was established that for some molecules an insufficient number of states were utilized in computing the partition sums for the higher temperatures. In the current implementation of the partition function

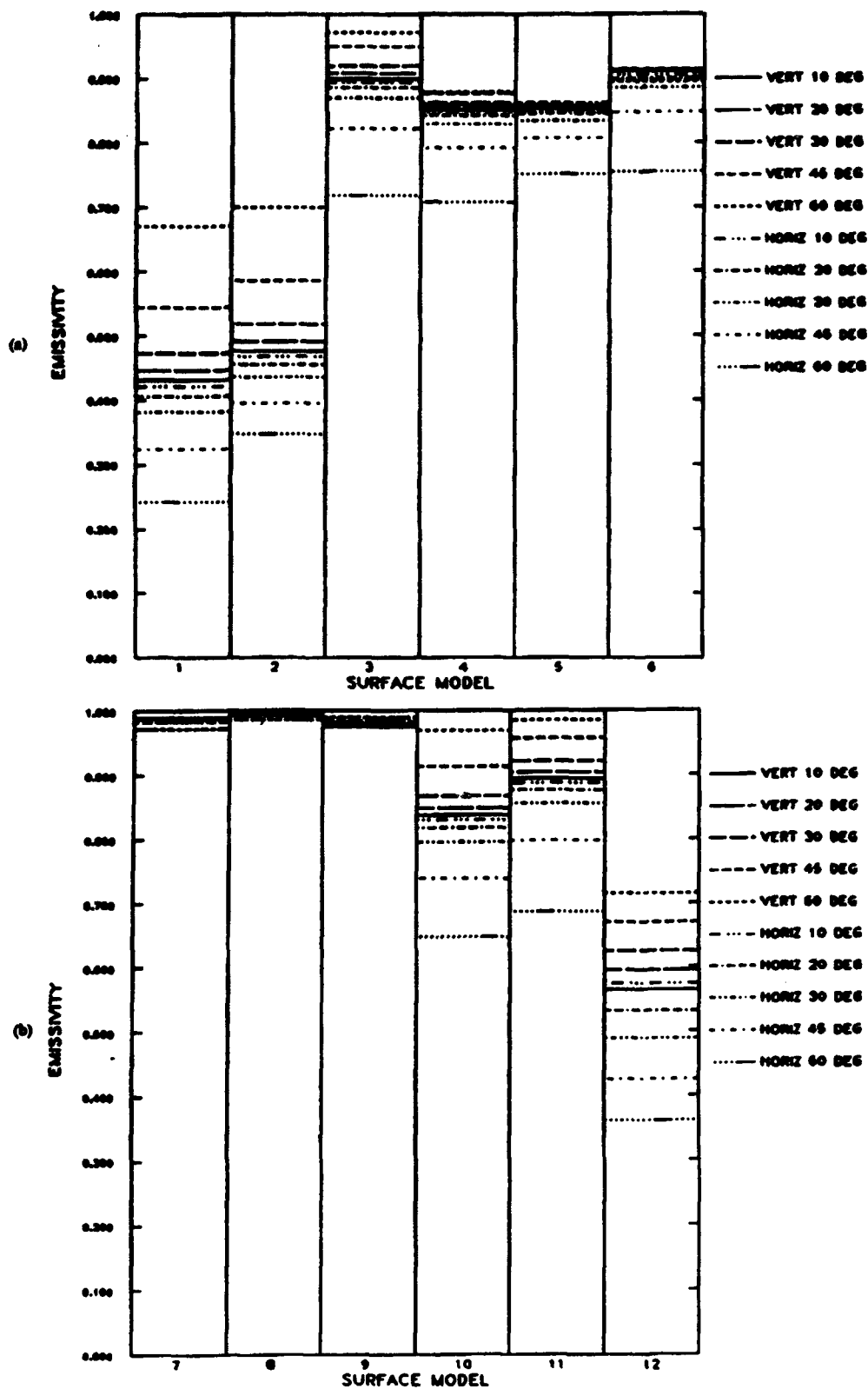


Figure 12. (a) Variation of 54° look-angle polarized emissivity (ϵ_v , ϵ_h) with surface model at frequencies of 1.2, 5.0, 10.6, 18.0, and 35.0 ghz. (Surface models 1-6, Table 3) (b) Same as (a). (Surface models 7-12, Table 3.)

calculation, the partition function for temperatures above 400 K is obtained by applying a classical isotopic independent temperature dependence to the value of the partition function at 400 K. This approach retains isotopic dependence for temperatures above 400 K.

9. INSTRUMENT FUNCTION ENHANCEMENTS

FASCODE includes the capability to convolve a monochromatic spectrum with an instrument response function (also known as a scanning function) in order to model a measured spectrum. This convolution can be performed either as a convolution in the spectral domain, as is currently done in FASCODE, or in the Fourier domain, using Fourier transforms. We have enhanced the instrument function capabilities of FASCODE both by improving the existing scanning functions and by adding the capability to perform the convolution in the Fourier domain. In addition, we have improved the efficiency of the interpolation routines.

9.1 Scanning Functions in the Spectral Domain

As a result of interactions with the U. of Wisconsin group, new scanning functions for sinc and sinc**2 have been developed and implemented in FASCOD3. The bound for these scanning functions has been extended to the proper value and the SHRINK function has been correctly applied so that the scanned spectra is consistent with the result that would be obtained if the calculation were performed in the fourier domain. The sampling interval used for the shrink algorithm is one-eighth the halfwidth of the scanning function for all functions. The effective bound for the sinc function is 119 halfwidths and for the sinc**2 function is 54 halfwidths. The area under the respective functions is effectively unity. A negative aspect of using the sinc function is the large bound associated with the function. For the HIS spectra with an unapodized halfwidth of 0.25 cm^{-1} , the bound is 30 cm^{-1} which requires that the calculated spectrum must extend 30 cm^{-1} beyond the spectral region of interest at each end of the spectrum. Nevertheless the higher resolution associated with the sinc function is a much more critical test of the spectroscopic results than can be obtained with other functions. The algorithm as it is coded performs the calculation with remarkably good efficiency.

9.2 Scanning Functions in the Fourier Domain

Nowadays, most measurements of infrared spectra both in the lab and in the atmosphere are made with Fourier Transform Spectrometers (FTS). Examples of atmospheric measurements with an FTS are the Stratospheric Cryogenic Infrared Balloon Experiment (SCRIBE) (Murcray et al., 1981), and High Resolution Interferometric Sounder (HIS) instruments (Smith et al., 1979). These instruments are characterized by high spectral resolution (up to 0.06 cm^{-1}) and large signal-to-noise. The AFGL line-by-line model is an ideal tool to provide simulations of spectral radiance at these spectral resolutions to aid in the identification of lines, perform retrieval studies, and to investigate phenomena such as line mixing (Hoke et al., 1988).

The spectral response function or "scanning function" of an FTS is nominally a sinc function, but can be modified by "apodizing" the interferogram: the scanning function is the Fourier Transform of the apodization function. The effect of apodization is to reduce the side lobes of the scanning function at the expense of broadening the central peak. When comparing calculated spectra with spectra measured with an FTS, it is important to accurately model the effects of the scanning function, including the side lobes.

Previously, FASCODE has performed the spectral smoothing as a convolution in the spectral domain. The accuracy of this approach depends upon the spectral extent (i.e. number of side lobes) over which the scanning function is defined. However, for a convolution, the computational time increases with the spectral extent, and for accurate calculations, can become large. We have developed a technique to perform spectral smoothing in the Fourier domain. This technique directly mimics the operation of an FTS: the calculated spectrum is transformed into an "interferogram", "apodized", and then transformed back to the smoothed spectrum. With this method, all the side lobes of the scanning function are preserved.

This technique has been implemented in a set of routines called FFTSCAN. The user is given the choice of a number of commonly used FTS scanning functions, and may specify the resolution either in terms of the width of the scanning function or in terms of the maximum optical path difference of an equivalent interferometer. As an option, the input spectrum may be prescanned with a narrow rectangular scanning function, leading to large savings in computational time and storage at negligible cost in accuracy. The routines may

be run as a stand alone program or added to FASCODE as an option. This work is reported on more fully in a separate report (Gallery and Clough, 1992).

9.2.1 Theory

In Fourier Transform Spectroscopy, the spectrum S is obtained from the interferogram I from:

$$S(\nu) = F (A(x) \cdot I(x)) \quad (1)$$

where F indicates the Fourier Transform, $A(x)$ is the apodization function, ν is the wavenumber and x is the optical path difference. By analogy, FFTSCAN calculates the smoothed spectrum S' from a monochromatic spectrum S as:

$$S'(\nu) = F (F (R) \cdot F (S)) \quad (2)$$

where $R(\nu)$ is the scanning function. Here, $F (S)$ is equivalent to the interferogram and $F (R)$ performs the role of the apodization function A . A fundamental theorem of Fourier Transforms states that:

$$F (F (R) \cdot F (S)) = R \star S \quad (3)$$

showing that Equation 2 is the same as a convolution in the frequency domain (\star indicates convolution).

The program offers a choice of five scanning functions commonly used with an FTS. These scanning functions, along with their associated apodization functions, are shown in Figure 13. For compatibility with previous versions of FASCODE, the rectangle, triangle, and gaussian scanning functions are also offered. The user may specify the width of the scanning function either as the half width at half maximum (HWHM) or as the maximum optical path difference of an equivalent interferometer.

The user is given the option of pre-scanning the input spectrum with a rectangular scanning function which is narrow compared with the selected scanning function (boxcaring). The pre-scanned spectrum is then resampled onto a coarser grid resulting in a large reduction in the number of points. Subsequent processing is then performed on the reduced spectrum. This procedure can result in large (orders of magnitude) savings in computational time and storage. The distortion of the resulting spectrum is small and can be partially corrected by "deconvolving" the reduced spectrum.

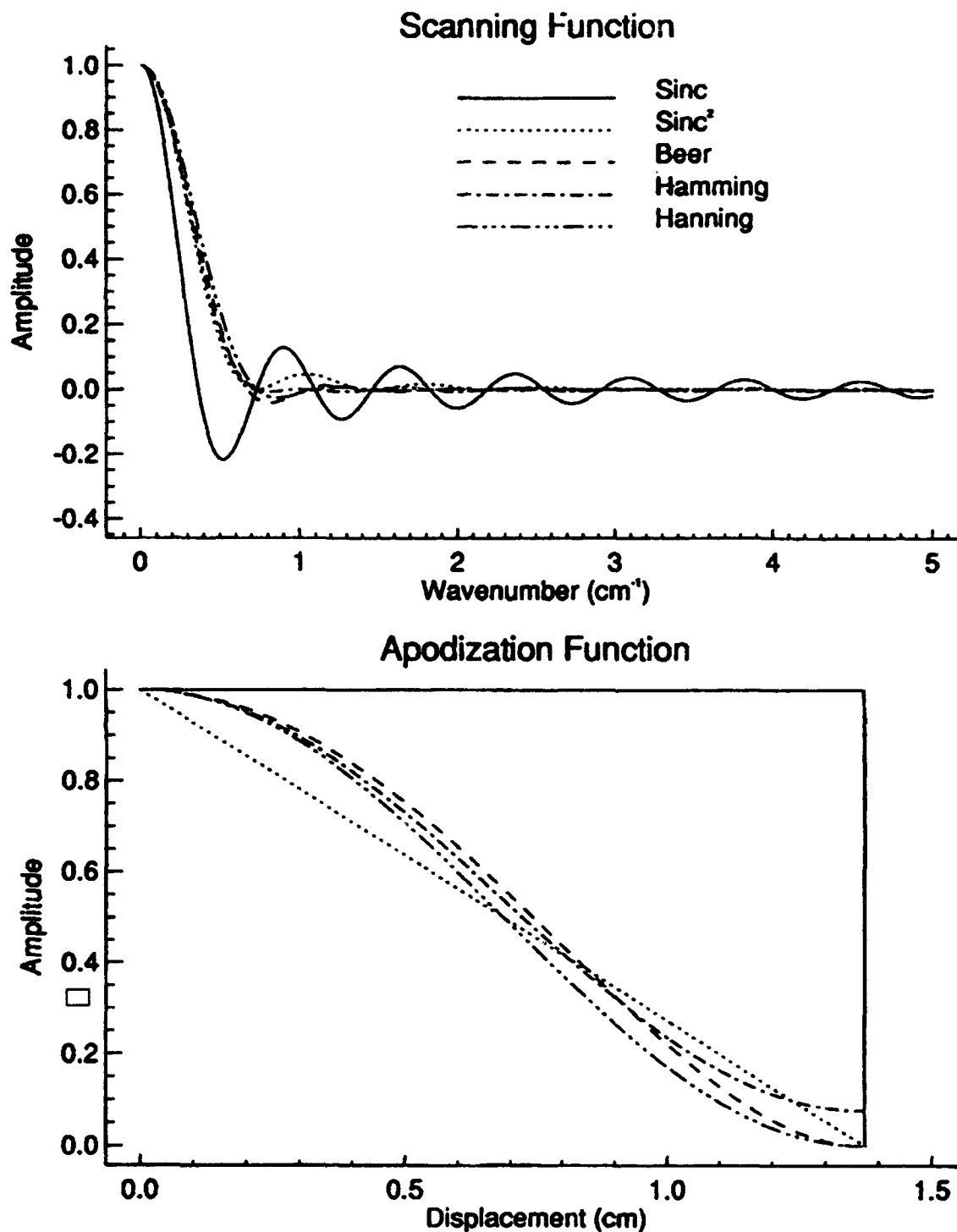


Figure 13. The Five FTS Scanning Functions and Their Associated Apodization Functions Available in FFTSCAN. The maximum displacement of 1.374 cm corresponds to the HIS instrument.

A FASCODE calculation can contain millions of points, more than can be stored and transformed in memory. A disk-based FFT routine was obtained from Mark Esplin of Stewart Radiance Lab, Bedford, MA, which can transform an array of arbitrary size. Using this routine, the FFTSCAN can smooth a FASCODE spectrum of any size. The computational time for the disk-based FFT is no more than three times that of an in-memory FFT of the same size. The program decides which routine to use - disk-based or in-memory-based upon the size of the spectrum and available memory.

9.2.2 Examples

Figure 14 shows an example of a FASCODE spectrum smoothed using FFTSCAN. The calculated spectrum models the upward radiance at 72 km for the US Standard Atmosphere. The monochromatic calculation extended from 600 to 800 cm^{-1} with a $\Delta\nu$ of 0.000953. In Figure 14a, the monochromatic FASCODE spectrum was smoothed with a sinc scanning function of $\text{HWHM} = 0.21926 \text{ cm}^{-1}$, corresponding to the HIS resolution. Figure 14b shows the error in the scanned spectrum from using boxcaring with deconvolution. In this case, boxcaring results in a 38 fold reduction in the number of points in the spectrum. The maximum error of about 1×10^{-8} is about 0.5 percent of the typical spectral excursion of 2×10^{-6} or about 0.2 percent of the maximum spectral value of 8×10^{-8} . For reference, Figure 14c shows the error using the standard FASCOD3 convolution with a bound of 119 halfwidths. The reference spectrum for calculating the errors in Figures 14b and 14c is the FFTSCAN calculation without boxcaring, interpolated to the proper grid.

Table 4 compares the computational time and maximum error for the calculations shown in Figure 14. The calculations were performed on an Sun SPARC station 2 and the scanning functions were applied from 625 cm^{-1} to 775 cm^{-1} . The results for scanning with the sinc² and the triangular scanning functions are also shown. Note that the boxcaring errors for the other functions are four times less than that for the sinc function.

These results show that for the sinc function, FFTSCAN with boxcaring provides a three-fold increase in speed and a better than two-fold increase in accuracy over the conventional FASCODE scanning routines. For the sinc² and the triangle, the execution time for the two programs is about equal, but FFTSCAN is again twice as accurate. The reference spectrum for calculating the errors is again the FFTSCAN calculation without boxcaring, interpolated to the proper grid.

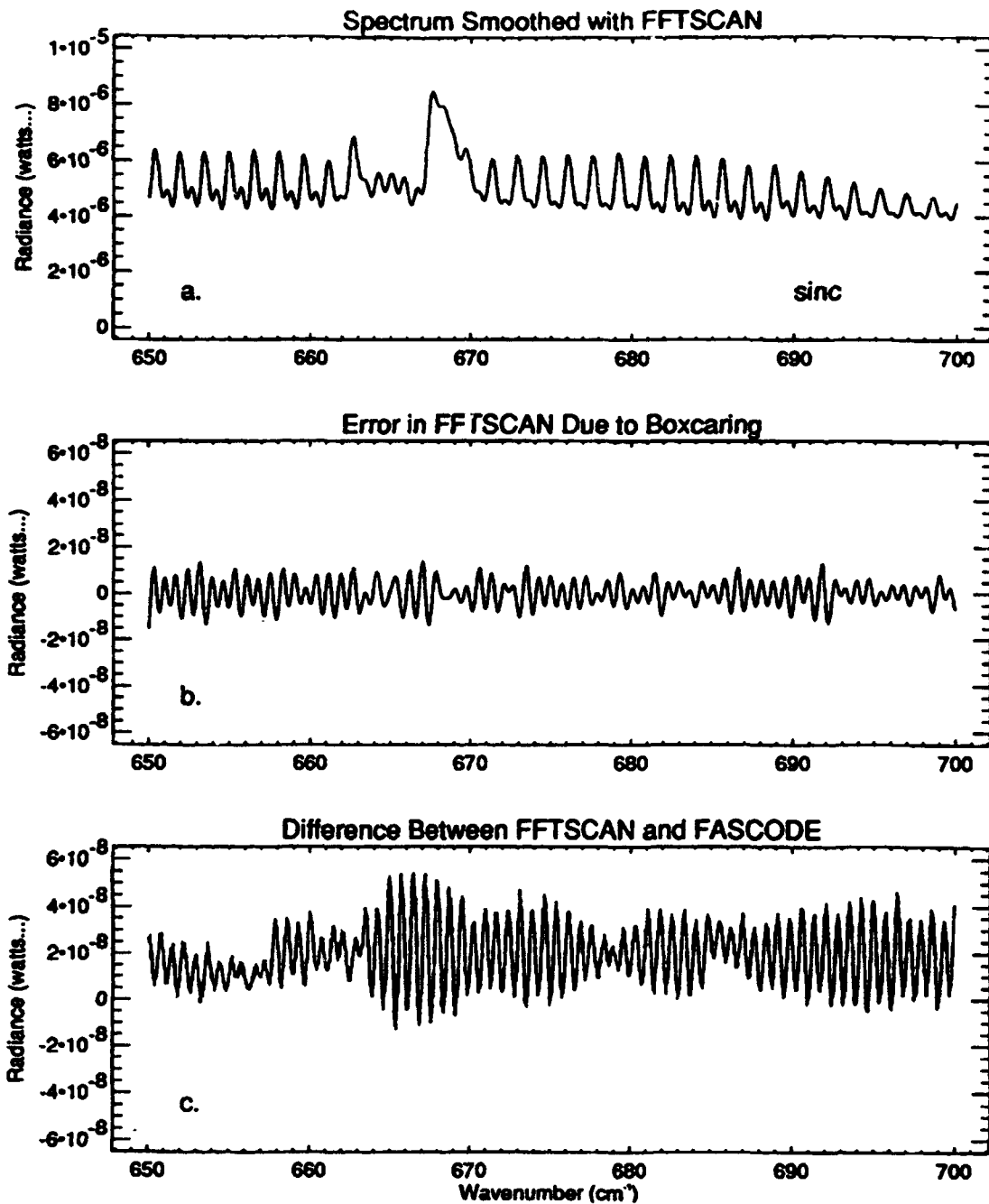


Figure 14. (a) FASCODE Calculated Spectrum Smoothed by FFTSCAN Plus The Error In the Smoothed Spectrum from using: (b) FFTSCAN With Boxcaring, and (c) the FASCODE3 Scanning Function. The scanning function is a sinc with a HWHH of 0.21962 cm^{-1} , corresponding to the HIS instrument in the unapodized mode.

Table 4. Comparison of Computational Time and Accuracy, FFTSCAN versus FASCODE, for the Sinc, Sinc², and Triangle Scanning Functions.

Scanning Option	Computational Time (sec)			Maximum Error (Percent Radiance)		
	Sinc	Sinc ²	Triangle	Sinc	Sinc ²	Triangle
FFTSCAN, No Boxcar	117	117	117	(NA)	(NA)	(NA)
FFTSCAN, With Boxcar	5.8	3.7	3.3	0.2	0.05	0.05
FASCODE3 Convolution	17.9	3.9	3.0	0.5	0.1	0.1

Notes:

- The computational times refer to a Sun SPARC station 2. Times are approximate and both the absolute and the relative times will vary depending on the case.
- The spectral extent of the smoothed spectrum was from 650 to 775 cm⁻¹.
- The monochromatic dV was 0.000953 cm⁻¹.
- The number of points in the scanned function was 167,958 (no boxcaring) and 4419 (with boxcaring), a reduction of a factor of 38.

9.2.3 Implementation

FFTSCAN is written in ANSI Standard Fortran 77 and is designed to be highly portable. It currently runs on a Sun SPARC station 2 but has been ported to a DEC VAX, an CDC Cyber, and an IBM PC. The few hardware dependent parameters, related to the disk-based FFT routines, are declared as parameters and collected in include files for easy modification. FFTSCAN can either be run as an independent program or be included as a module of FASCODE (called by setting ISCAN = 3). However, it has not yet actually been incorporated into FASCODE. A detailed set of user instructions is included in the report.

9.3 Interpolation

A new interpolation algorithm has been developed which is considerably more efficient than the previous algorithm and provides the option of performing linear or four point interpolation. The latter option uses continuous first derivatives, consistent with the four point interpolation in the other FASCODE modules.

10. LINE SHAPE

The current limitations on the accuracy of many radiative transfer calculations is the limitation of our knowledge of the shape of the spectral line wings. The far wing line shape for water vapor is treated by including the line wing effects in the continuum. For carbon dioxide, the collisionally-broadened line wings are dependent on quadrupole-quadrupole interactions giving rise to line wing effects closer to line center. This precludes incorporation of wing effects in the continuum as the continuum is defined in the advanced spectral model. There are two important aspects of the line broadening problem that need to be considered for a proper treatment of atmospheric absorption by carbon dioxide: duration of collision effects and line coupling effects. In principal these effects should be treated together. In reality the problem is sufficiently complex that treating them independently is difficult enough and for most purposes reasonable results can be obtained in the context of the known physical constraints.

10.1 Line Shape for Carbon Dioxide

The carbon dioxide line shape that has been used in the spectral model was deduced from measurements by Burch in the 2400 cm^{-1} band head. Recent comparisons with other models and with the data discussed in Section 13.1 suggest that the sub-lorentzian character of the carbon dioxide line shape currently being used is too strong. The line shape is given by the expression

$$f(\nu) = L(\nu - \nu_o) \chi(|\nu - \nu_o|)$$

with

$$L(\nu - \nu_o) = \frac{1}{\pi} \frac{\alpha_c}{(\nu - \nu_o)^2 + \alpha_c^2}$$

where $L(\nu - \nu_o)$ is the impact line shape with α_c the collisional halfwidth, ν_o the transition wavenumber value, and $\chi(|\nu - \nu_o|)$ is a function generally referred to as the chi factor, which provides the necessary correction to the impact line shape to obtain agreement with observed line wing effects.

For the advanced spectral model, the implementation of the strong sub-lorentzian behavior appropriate to carbon dioxide requires the application of a chi factor $\chi'(|\nu - \nu_o|)$, to the fourth function (Clough et al., 1981), where χ' is defined through the relation

$$\begin{aligned}
& 1 + C_2 (v - v_o)^2 + C_4 (v - v_o)^4 + C_6 (v - v_o)^6 & |v - v_o| \leq V_o \\
\chi'(|v - v_o|) = & D \exp(-a|v - v_o|^b) & |v - v_o| \geq V_o
\end{aligned}$$

where we have utilized values for the constants obtained from the work of Burch and collaborators,

$$a = 0.623$$

and

$$b = 0.410.$$

The coefficients C_2 , C_4 , C_6 and D are chosen to provide continuity of the chi function for the value and the first two derivatives of the function at wavenumber value V_o .

The total chi factor for the line $\chi(|v - v_o|)$, in the context of the present model, is given by the expression

$$\begin{aligned}
& 1 - \frac{Q_3(|v - v_o|)}{L(v - v_o)} \chi'(|v - v_o|) & |v - v_o| \leq 64\alpha_c \\
\chi(|v - v_o|) = & \chi'(|v - v_o|) & |v - v_o| \geq 64\alpha_c
\end{aligned}$$

where $Q_3(|v - v_o|)$ is a polynomial used in the line shape decomposition. In Figure 15 we indicate the chi function for carbon dioxide previously implemented in the spectral model for which $V_o = 2 \text{ cm}^{-1}$. One of the significant drawbacks to the present formulation is that the chi function is pressure dependent and in Figure 16 two chi functions are provided, one with $\alpha_c = 0.08 \text{ cm}^{-1}$ which corresponds to atmospheric pressure and one with $\alpha_c = 0.008 \text{ cm}^{-1}$ corresponding to one-tenth atmospheric pressure. The carbon dioxide line shape is readily modified in the spectral model through the choice of V_o . In Figure 16 we provide a new recommended chi function obtained with $V_o = 8 \text{ cm}^{-1}$. This provides a result that is less pressure dependent, has an integrated value for the line shape closer to unity, and is consistent with the data against which we have made comparisons.

The bandhead of carbon dioxide at 2385 cm^{-1} is an interesting spectral region particularly from the point-of-view of its importance for remote sensing of temperature. It has been proposed that line coupling plays an important role in the valleys between spectral

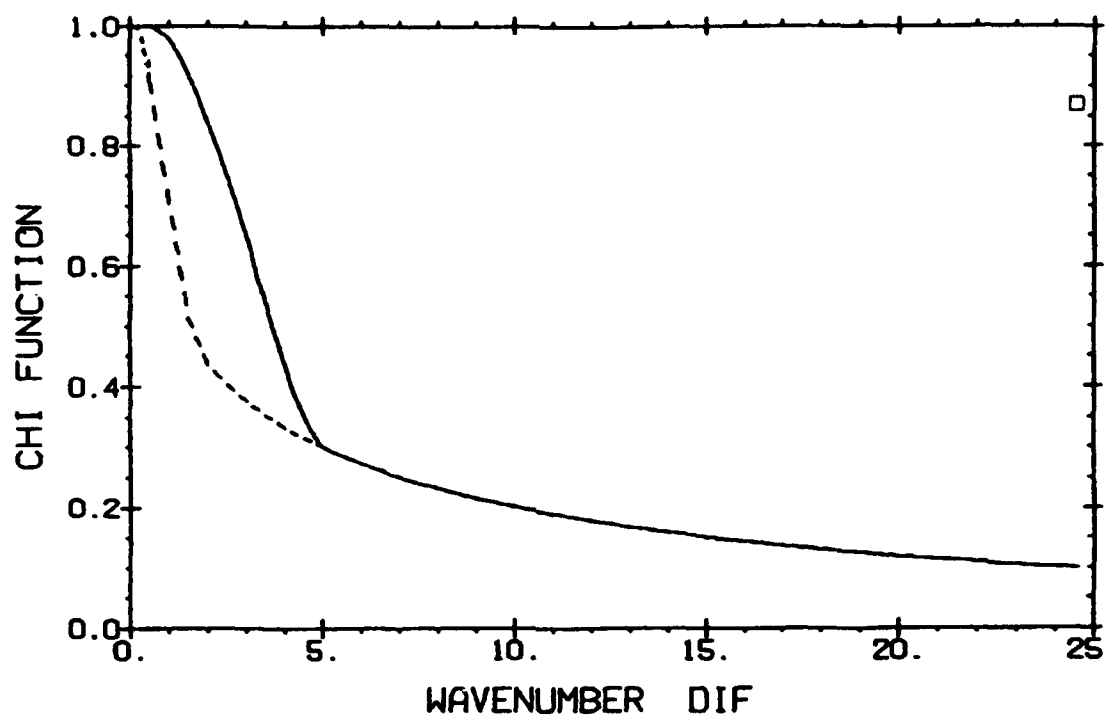


Figure 15. The chi function for carbon dioxide with $V_0 = 2 \text{ cm}^{-1}$. The solid line is for halfwidth of 0.08 cm^{-1} (1 atm) and the dashed line is for a halfwidth of 0.008 cm^{-1} (0.1 atm).

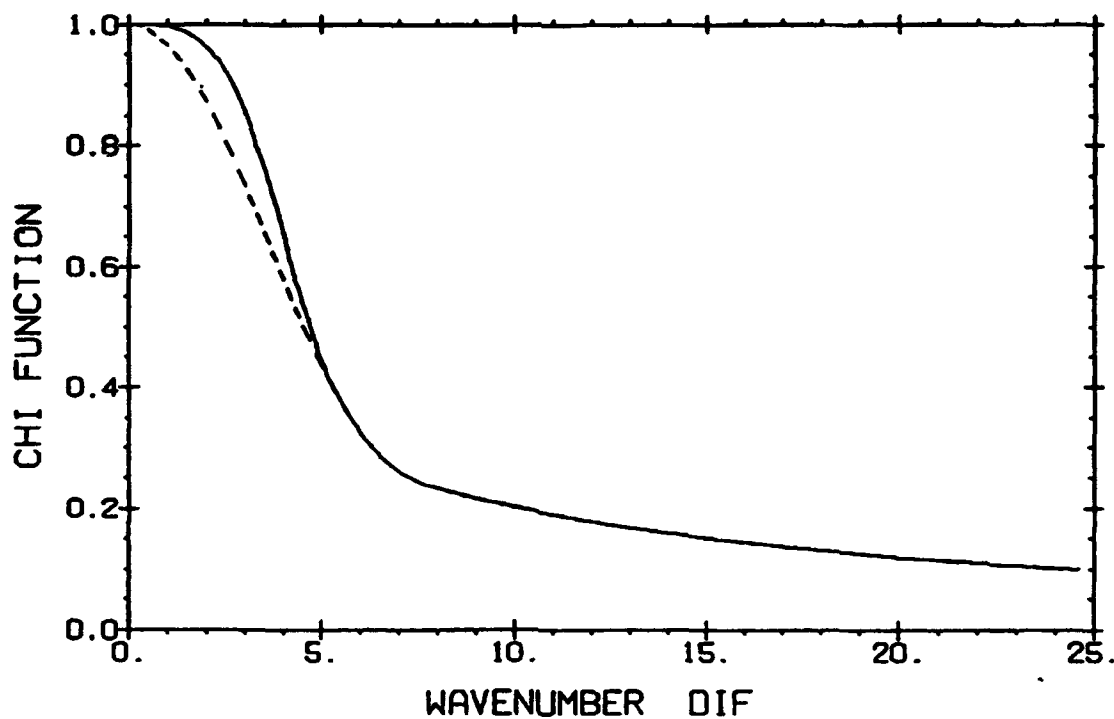


Figure 16. The chi function for carbon dioxide with $V_0 = 8 \text{ cm}^{-1}$. The solid line is for halfwidth of 0.08 cm^{-1} (1 atm) and the dashed line is for a halfwidth of 0.008 cm^{-1} (0.1 atm).

lines in this band and particularly at the bandhead. However, performing accelerated line-by-line computations including line coupling effects with spectral lines spanning a broad range is problematical. Consequently it is presumed that a judicious choice of chi function will satisfactorily describe the absorption in this region. In Figure 17 we show the calculated transmittance for a limb calculation for two values of V_0 : $V_0 = 2 \text{ cm}^{-1}$ and $V_0 = 8 \text{ cm}^{-1}$. The tangent height for this case is 20.5 km. The results are substantially the same.

In Figure 18 we provide an ATMOS limb occultation spectrum (R. Zander, private communication, 1988) with a 17.7 km tangent height. The absolute values for the transmittance are in some doubt in this spectrum so it is not feasible to perform a detailed analysis with this particular data set. A calculation with $V_0 = 2 \text{ cm}^{-1}$, shown in Figure 19, provides a result which while in marginal agreement with the observation cannot really be considered satisfactory. It should be noted that an instrument function consistent with the ATMOS data was not available so that the lines appear with greater amplitude in the calculation. Based on the previous considerations, a calculation with $V_0 = 8 \text{ cm}^{-1}$ would provide substantially the same result. There are three effects contributing to the absorption in the spectral region of disagreement: carbon dioxide line shape including line coupling, the collision induced band of nitrogen, and the water vapor continuum. Improved data is really necessary to facilitate the analysis of these effects.

A final comparison was performed between calculations with the different chi factors for a case in the 690 cm^{-1} region from the ITRA exercise. In Figure 20 is shown the transmittance spectrum for a 30 km tangent height with $V_0 = 2 \text{ cm}^{-1}$ and in Figure 21 the result with $V_0 = 8 \text{ cm}^{-1}$. Here a difference is discernible in the spectral valleys between the lines.

10.2 Line Coupling for Carbon Dioxide

Because of the importance for remote sensing of the carbon dioxide Q-branches in the spectral region from 600 cm^{-1} - 800 cm^{-1} , a concerted effort has been devoted to the refinement and validation of the model in this spectral region particularly with respect to the Q-branches. Our efforts have proceeded directly along the lines described by Hoke et al. (1988) and the reader is referred to that paper for details of the approach. In the present report we describe the validation of the coupling coefficients and the rationale for a proposed refinement. The Q-branches of principal interest occur at 618, 720, 740 and 794 cm^{-1} .

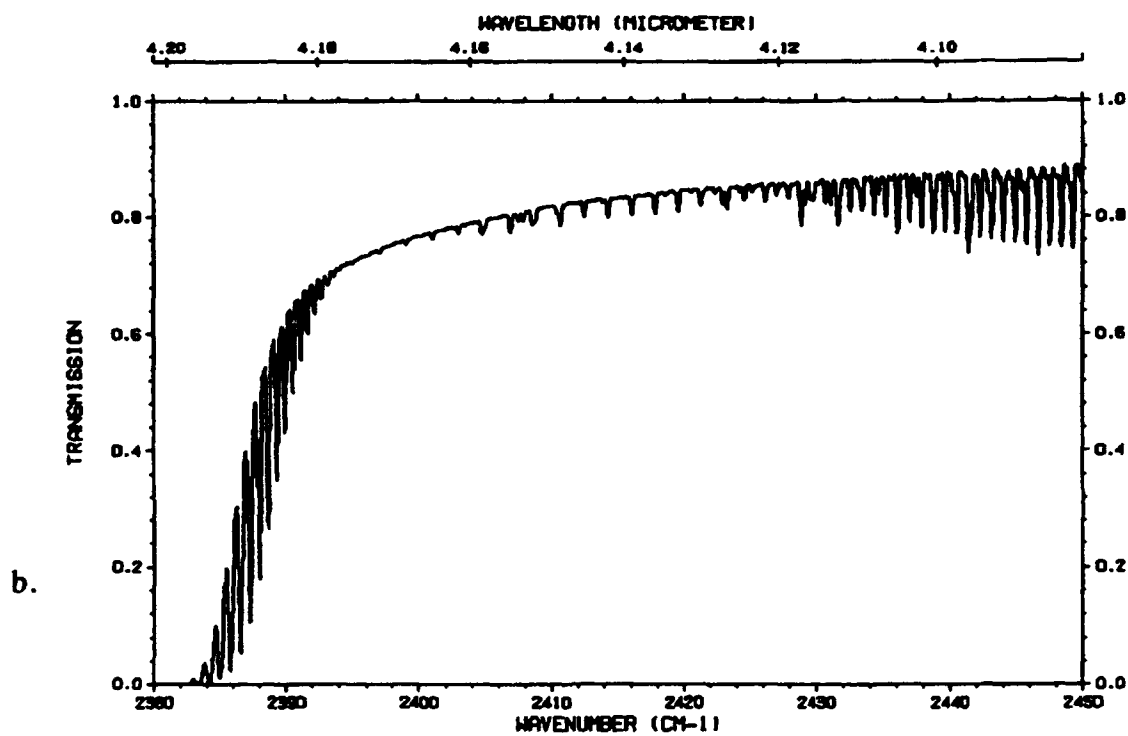
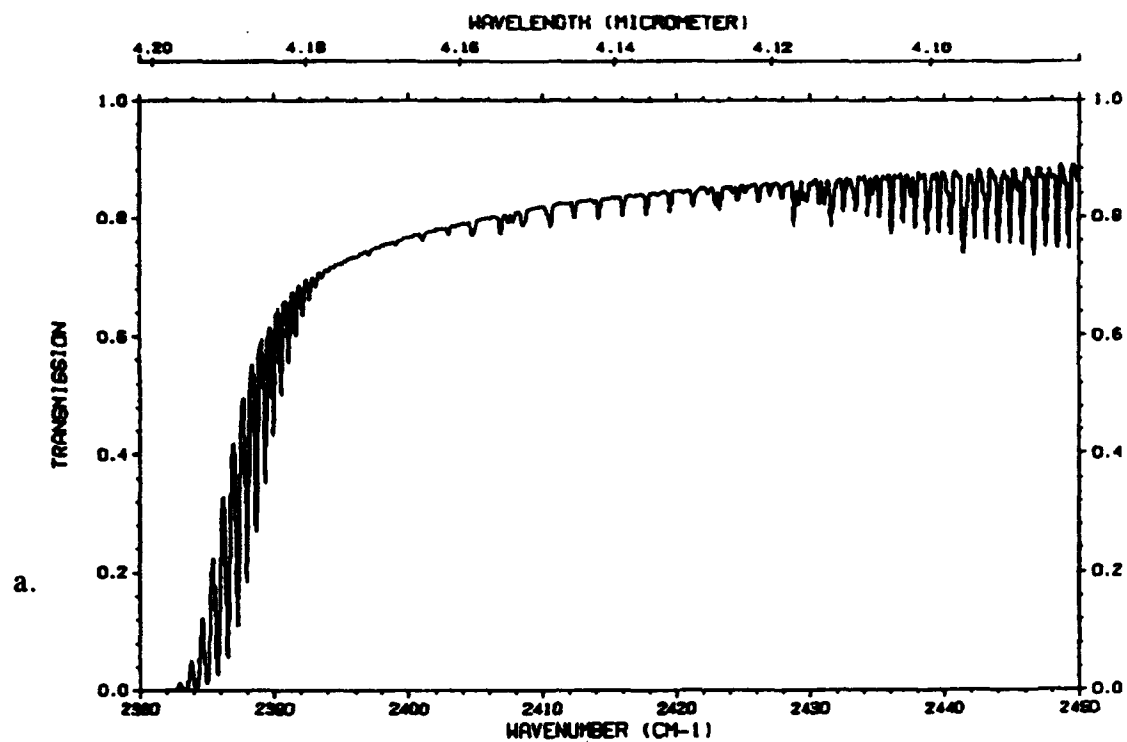


Figure 17. (a) Calculated limb transmittance spectrum with $V_0 = 2 \text{ cm}^{-1}$; (b) Calculated limb transmittance spectrum with $V_0 = 8 \text{ cm}^{-1}$.

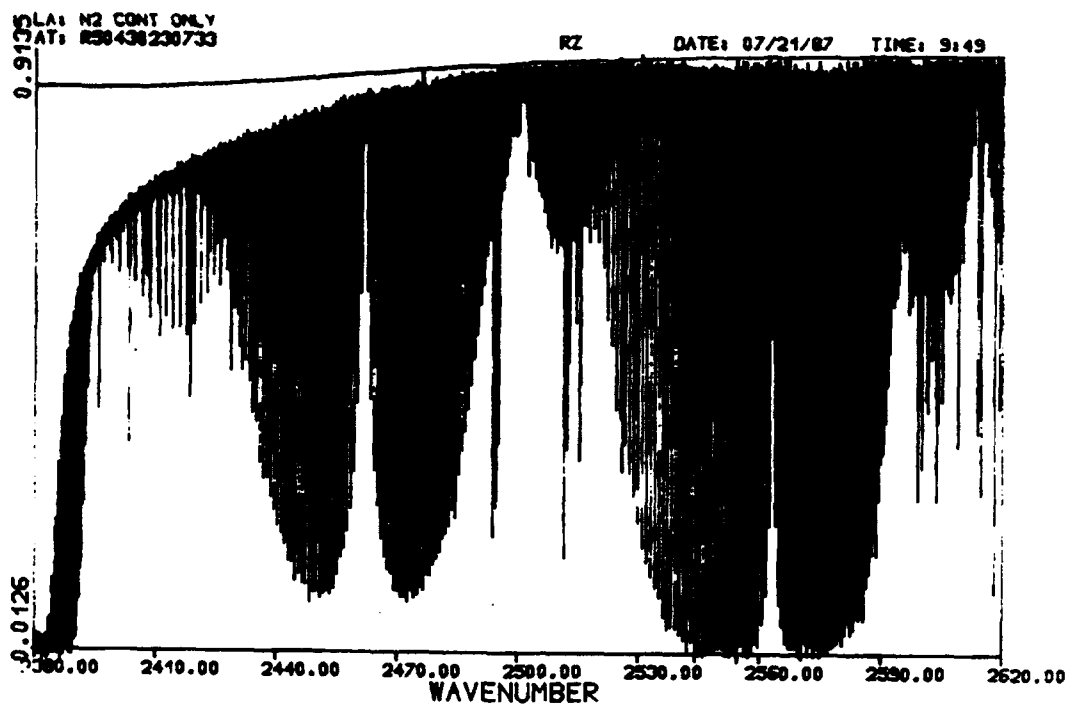


Figure 18. An ATMOS occultation transmittance spectrum (R. Zander, private communication, 1988). The tangent height is 20.5 km.

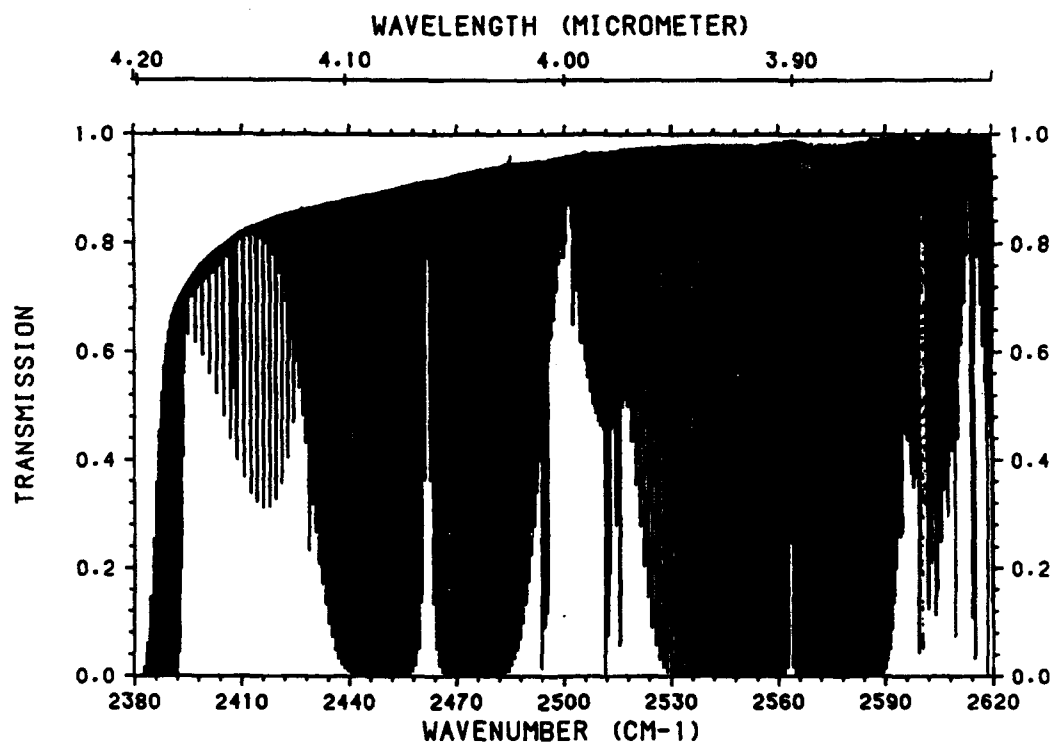


Figure 19. A calculation with $V_0 = 2 \text{ cm}^{-1}$ for the measurement conditions of Figure 19.

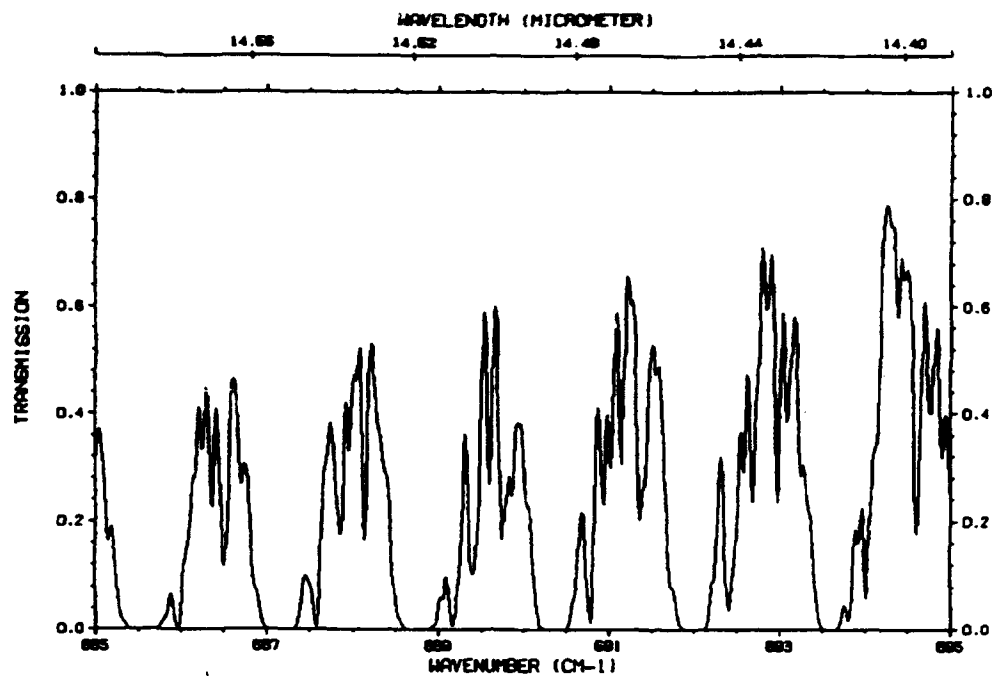


Figure 20. Limb transmittance spectrum for the conditions of the ITRA intercomparison with a 30 km tangent height for $V_o = 2 \text{ cm}^{-1}$.

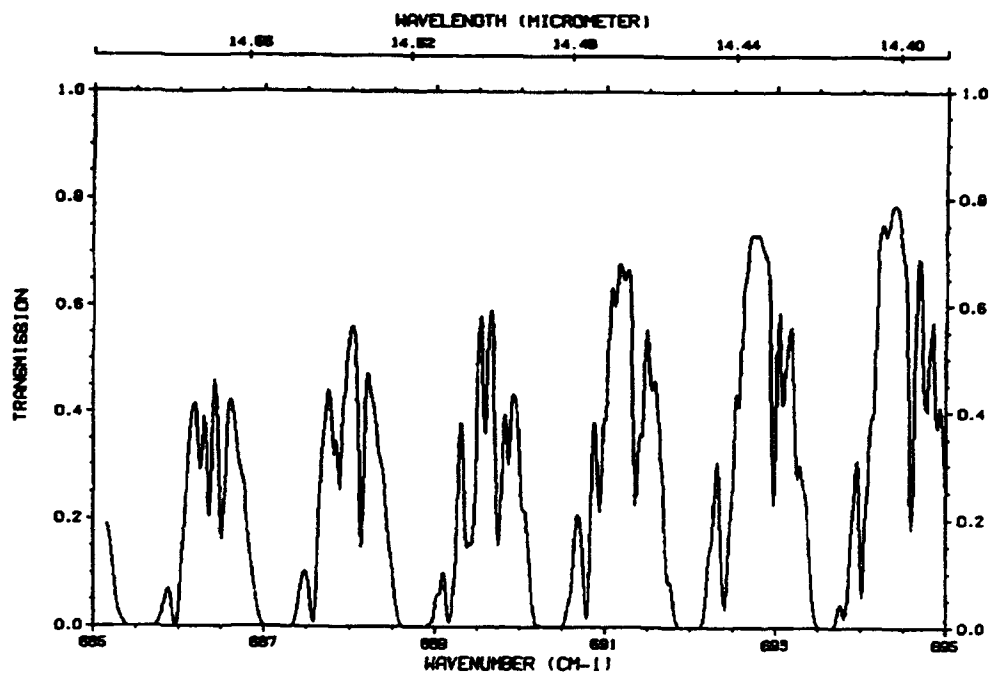


Figure 21. Limb transmittance spectrum for the conditions of the ITRA intercomparison with a 30 km tangent height for $V_o = 8 \text{ cm}^{-1}$.

The initial data that were used for the validation were from a nadir viewing spectral radiance measurement made with the HIS instrument, Smith et al. (1983), from the ER2 aircraft flying at 19.6 km over ocean on April 14, 1986. A summary of the experiment and an initial analysis of the data was given by Clough et al. (1988). In Figure 22 we indicate the spectral residuals from 600 - 800 cm^{-1} in terms of equivalent brightness temperature for a validation with 1992 HITRAN parameters and no line coupling. The residual at 667 cm^{-1} is due to warmer gas in the vicinity of the instrument and not to line coupling. With respect to the line coupling, Figure 22a provides a result similar to that given in Figure 26 but for the smaller spectral range. In Figure 22b we indicate the residuals obtained with the line coupling coefficients provided by Hoke et al. (1988 and private communication). Although a substantial improvement has been obtained, the residuals associated with the Q-branches are apparent and unacceptably large for remote sensing problems. In the course of studying this problem it became apparent that if the coupling coefficients, both the y's and the g's, were scaled by a multiplicative factor of 1.3, a much improved result was obtained. This result is provided in Figure 22c. In the calculation of the coupling coefficients, a combination of the energy power gap and exponential gap have been used to obtain the elements of the rate matrix. The coefficients of the energy gap expressions have been obtained by performing a least squares fit to the carbon dioxide halfwidths. This is far from a rigorous procedure for obtaining the rate matrix elements so that from our perspective the need to scale the coupling coefficients is not inconsistent with the physics. It should be noted that a single scale factor provides an improved result for the three Q-branch regions at 618, 720, and 740 cm^{-1} . This provides support for the proposition that the effect is due to the line coupling parameters and not to an artifact of the measurement or to the errors in the description of the atmospheric temperature field. The Q-branch at 740 cm^{-1} is associated with a much warmer temperature than the 618 or 720 cm^{-1} Q-branches. The residuals for the 794 cm^{-1} Q-branch are only marginally effected by inclusion of line coupling effects, primarily because of residuals associated with other species.

After discussion with scientists at the Phillips Laboratory, the value of performing a similar validation using a zenith ground based observation became apparent. Data from 1 November 1988 taken as part of the GAPEX experiment by the U. of Wisconsin researchers (Knuteson et al., private communication) have been utilized. This validation provides a second observation with a significantly different temperature field with respect to the optical path. The results are provided in Figure 23. The results for the 618, 720, and 740 cm^{-1} Q-branches fully support the scaling factor of 1.3. In the course of this

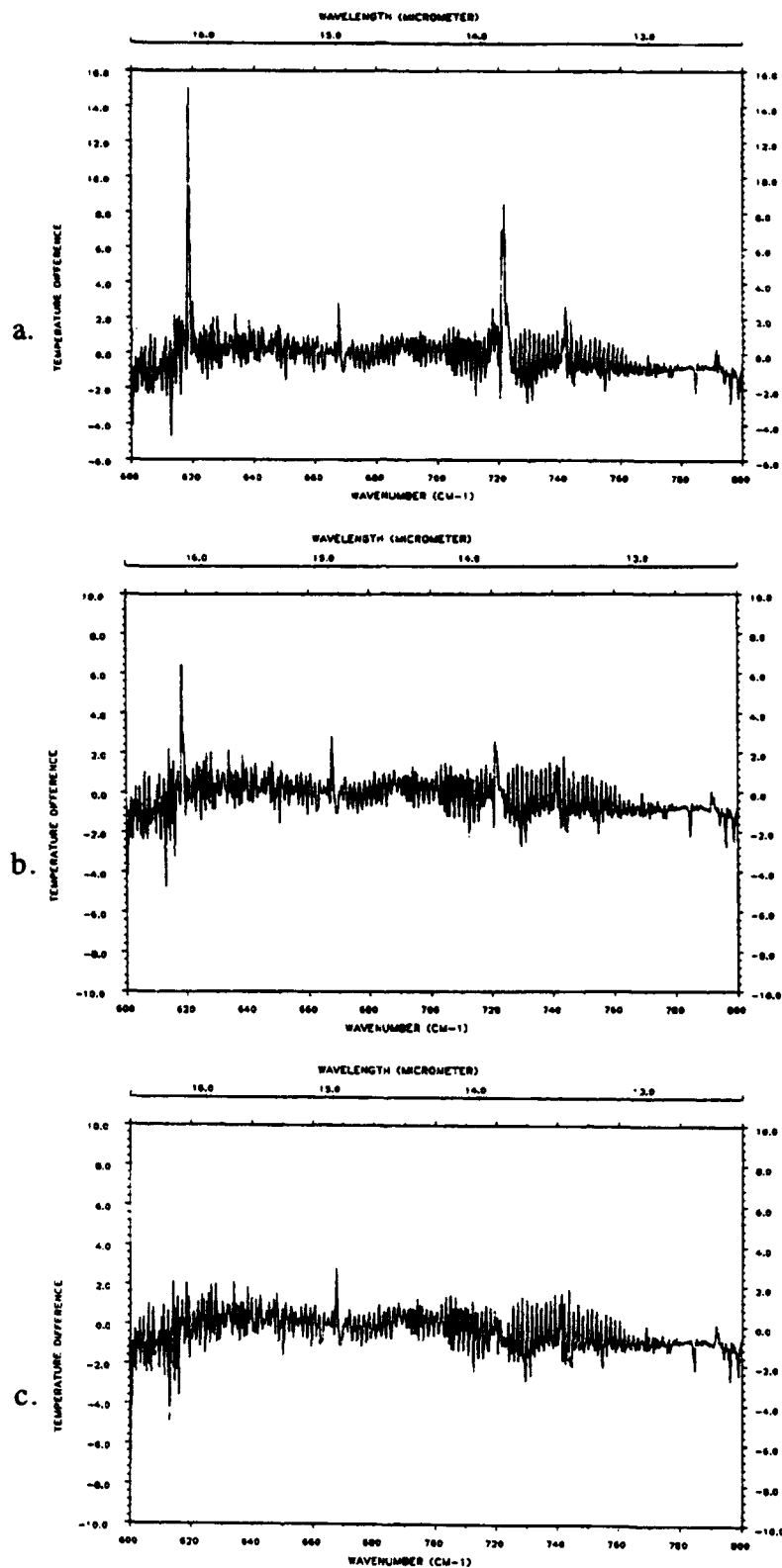


Figure 22. Effect of line coupling on the spectral residuals for the nadir HIS observation of 14 April 1986: a) no line coupling, b) line coupling with the basis coupling coefficients, and c) basis coupling coefficients multiplied by a factor of 1.3.

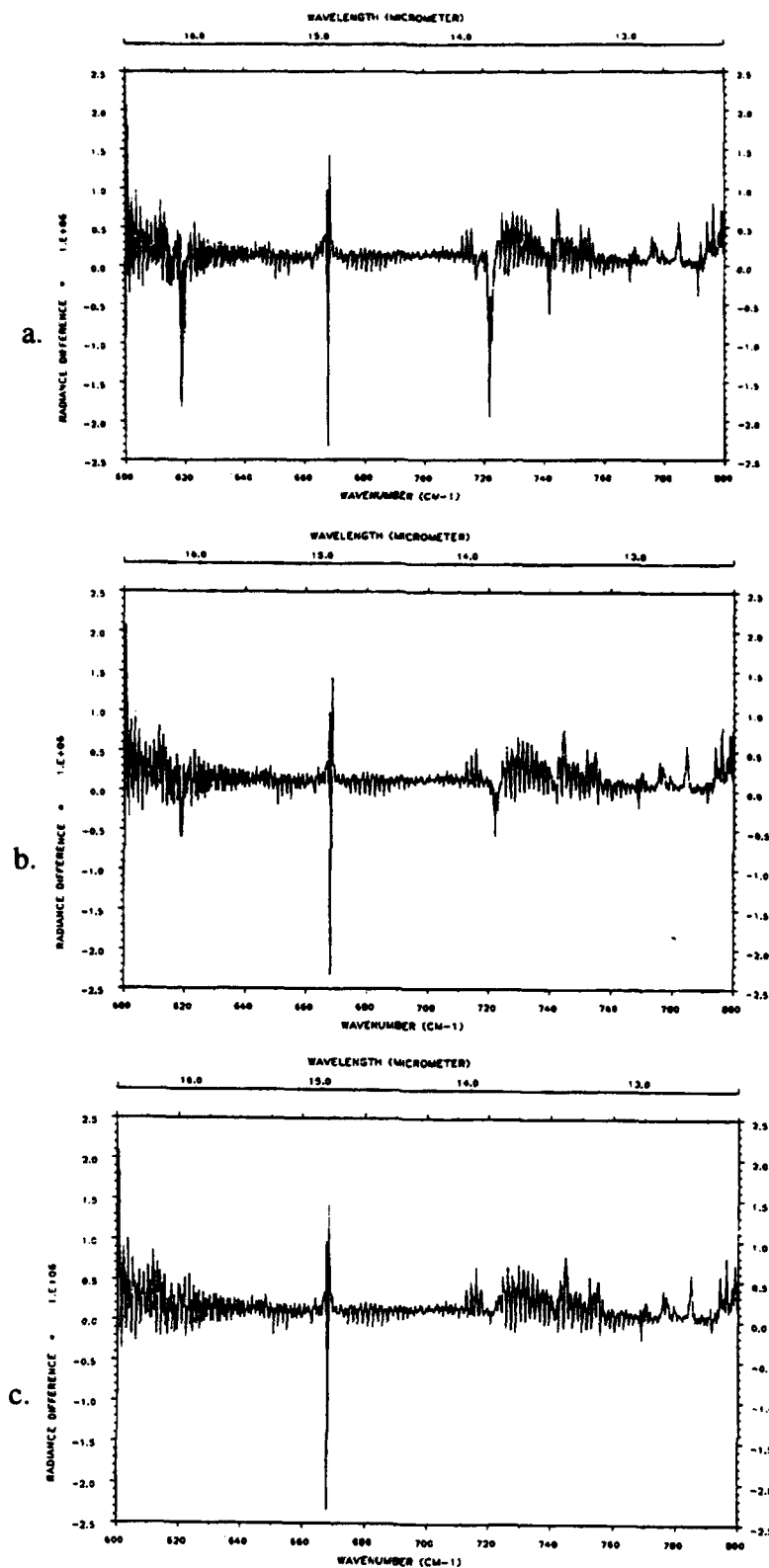


Figure 23. Effect of line coupling on the spectral residuals for the zenith observation of 1 November 1988 with the HIS instrument: a) no line coupling, b) line coupling with the basis coupling coefficients, and c) basis coupling coefficients multiplied by a factor of 1.3.

study, an adjustment of the temperature dependence of the coupling coefficients was explored to ascertain whether equivalent results could be obtained. Consistent with the fact that the different Q-branches are influenced by different temperature regimes in the atmosphere, no simple adjustment of the temperature dependence could provide an equivalent result. The spectral residuals associated with the P and R branches of the 618 and 720 cm^{-1} carbon dioxide bands as seen in Figures 22 and 23 are of particular note. These residuals, up to $\pm 2\text{K}$ in brightness temperature for the nadir, are the largest residuals in this measurement band. It has not been possible to obtain an improved result with a retrieved atmospheric temperature profile, suggesting that the errors are spectroscopic in nature. This conclusion is supported by a plot of the residuals from 680 - 780 cm^{-1} of Figure 22 against equivalent brightness temperature as provided in Figure 24. The lack of correlation implies that there is no adjustment of the atmospheric temperature field that can provide an improved result.

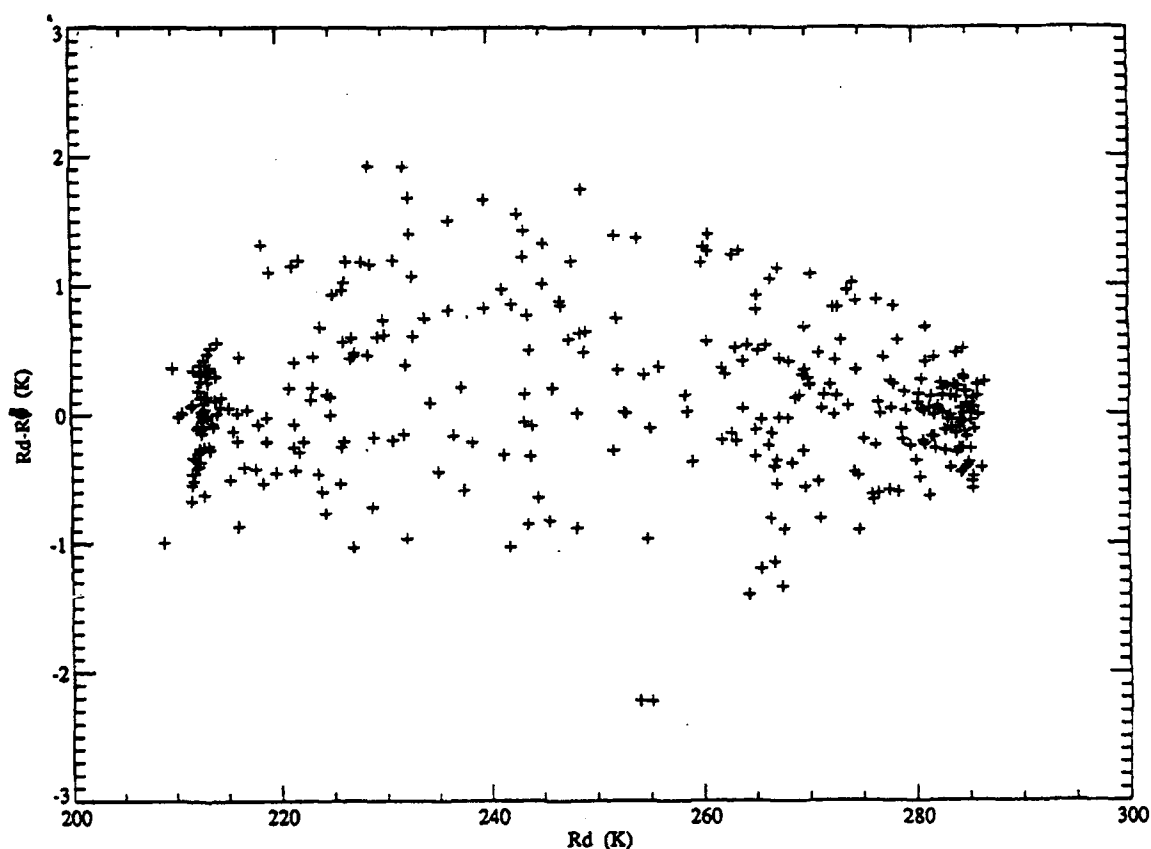


Figure 24. Brightness temperature residuals associated with Figure 22c as a function of brightness temperature.

11. COLLISION INDUCED BANDS

As a result of recent theoretical and experimental considerations, it is possible to attain some improvement in the treatment of a number of collision induced bands important to atmospheric radiative transfer modeling. The collision induced bands of particular interest include the nitrogen band in the pure rotation region, the oxygen band at 1600 cm^{-1} and the nitrogen band at 2350 cm^{-1} with important contributions at 2400 cm^{-1} .

With respect to the collision induced nitrogen band at 2350 cm^{-1} , the best current validations appear to be associated with the ATMOS experiment in which it is possible to study the absorption in the spectral region from $2400 - 2600\text{ cm}^{-1}$ as a function of tangent height (e.g. Figure 18). As a result of studying ATMOS spectra for 20.5 and 17.6 km tangent heights and given the uncertainty in the far wing line shape of carbon dioxide which impacts the absorption beyond the bandhead at 2385 cm^{-1} , a modification of the nitrogen continuum currently in the model does not seem warranted at the present time. It should be pointed out that the ATMOS spectra test both the pressure and temperature dependence of the model, although not independently.

With respect to the collision induced oxygen band at 1600 cm^{-1} , we have implemented the modification proposed by Rinsland et al., 1989. This modification involved the application of a multiplicative scale factor of 0.78 to all values of the oxygen continuum. The analysis of Rinsland et al. (1989) was also based on results from the ATMOS occultation experiment (R. Zander, private communication, 1988).

12. SPECTRAL MODEL ENHANCEMENTS

A review of the advanced spectral modeling developments implemented for FASCODE under this effort are summarized below. A number of these topics are covered in greater detail in other sections of this report, but are included here for completeness.

CURRENTLY IMPLEMENTED INTO FASCODE

- LINE-BY-LINE CALCULATION
 - Interpolation error corrected (affected interpolation of aerosols, the continuum, and the fourth function, at the ends of the panel)
 - Implementation of the improved radiance algorithm (uses level temperatures)

- **SCAN/INTERPOLATION UPDATES**
 - Error in SHRINK fixed (related to wavenumber shifts)
 - RECTANGLE function updated
 - SINC function updated with new bound
 - SINC**2 function updated with new bound
 - Input option for first zero crossing of periodic functions
 - Input option to specify the output spectral spacing
 - Input file is first interpolated before being scanned when input DV is too coarse
 - INTRPL rewritten (four-point interpolation scheme added)
- **CROSS-SECTIONS FOR HEAVY MOLECULES**
 - Extinction effects of heavy molecules (HITRAN '86)
 - Lorentzian convolution over the cross-sections to account for pressure-dependence effects
 - Temperature-dependent cross-section data from HITRAN '91 can also be used
 - Atmospheric trace profiles from 'AER/NASA community model'
- **PARTITION SUMS**
 - Program TIPS from Gamache and Rothman incorporated
 - Isotopic species now treated correctly within FASCODE
 - Problem with partition sums at high temperatures addressed (Gamache and Rothman currently investigating)
 - TESTMM was also modified to set the isotope for all lines contained in the block data set to 'I'.
- **LINE COUPLING**
 - Line coupling coefficients on TAPE3 at four temperatures are required (200 K, 250 K 296 K and 340 K)
 - Files: CPLDT & CPLDT13/UN=ISAACS (9 Nov 1990)
 - Current implementation is compatible with HITRAN '91
 - The line-coupling coefficients for O₂ were updated and integrated back into LNFL and BTEST
- **FLUX CALCULATIONS**
 - Heating rate routines provided in FLUXF/UN=ISAACS (9 Nov 1990)
- **FSCATM**
 - Level temperatures and pressures provided on TAPE7 output
 - Cross-section profile capability added
- **LOWTRAN7/AEROSOLS**
 - Fix to V1, V2 (AV1, AV2 in LOWTRN) on FILHDR
 - Option added to allow input of precalculated aerosols

- **SEQUENTIAL TRANSMITTANCE/RADIANCE**
 - Total transmittances/radiances from observer to successive layers
 - Extensive improvements have been made in the sequential calculation option, formerly called the weighting function option. Sequential radiances may now be obtained, an option that is necessary for the calculation of fluxes and heating rates. The improved interpolation algorithm has been adapted to perform more efficient interpolations in the course of the merging computations for transmittance and radiance.
- **REFLECTED ATMOSPHERE**
 - Option to include the effects of atmospheric radiation reflected by the earth's surface
 - Spectral variation of reflectivity and emissivity (quadratic in wavenumber)
- **PLOT PACKAGE ENHANCEMENTS - ACCESS TO FORMATTED RESULTS**
 - The output of the plot header is now an option
 - Optional formatted output file
 - FASCODE formatted output plot file
 - File difference/ratio option
 - Plot overlays with offsets
 - Interface to NCAR routines
- **ENHANCED PORTABILITY**
 - Hollerith data statements have been replaced with character strings
 - UNIX date and time calls provided
- **NEW DEFAULTS**
 - The default for the average air broadened halfwidth (ALFAL0) has been changed to 0.08 cm^{-1} for the case of no line coupling. Suggested value for ALFAL0 is 0.04 cm^{-1} for the case with line coupling.
 - Default values for line rejection may be invoked using negative values for DPTMIN and/or DPTFAC. The default values are
 0.0002 for DPTMIN
 0.001 for DPTFAC
 - The default values for the boundary temperature differential for FSCATM have been changed to
 8 K at alt1
 12 K at alt2
- **LNFL - LINE FILE CREATION PROGRAM**
 - Molecules expanded to 35 (from 28)
 - Isotope information now included in molecule variable
 - Fully compatible with HITRAN 91
 - Flag on header indicates presence of isotopic information

- **USER DOCUMENTATION**
 - User Instructions for FASCODE and LNFL
 - Description of routines and input parameters
 - Block Diagrams of FASCODE and LNFL

Additional Issues related to FASCOD3 -

- J.C. Chetwynd (PL/GP) and R.D. Worsham (AER) met in late June and confirmed that the changes which had been made in the AER code, were also in the PL/GP version of the code.

13. ADVANCED SPECTRAL MODEL VALIDATION

13.1 Validation with Data from the High-resolution Interferometer Sounder (HIS)

A detailed comparison between measured and calculated upwelling radiances has been undertaken to validate both the results from the High-resolution Interferometer Sounder, HIS, (Smith et al., 1983) and to validate the performance of the advanced atmospheric radiance model. This constitutes an important step in establishing the extent of the retrieval improvement attainable with the HIS instrument operating in space. Special emphasis has been placed on atmospheric spectroscopic issues associated with line coupling; the line shape for carbon dioxide; and atmospheric window absorption including effects due to water vapor and chlorofluorocarbons in the 800 to 1200 cm^{-1} region.

The HIS is an accurately calibrated Fourier Transform spectrometer developed to measure infrared radiances. The important characteristics of the instrument are summarized in Table 5 and described in detail by Revercomb (1987). Accurate radiometric calibration has been a central focus of the HIS program and is achieved by using two blackbody calibration sources, one at 300 K and the other at 245 K. In the validations described here, a correction has been applied to the measured the interferogram to account for a small finite field-of-view effect. This correction has been applied by the U. of Wisconsin workers and has facilitated the validation with the spectral model. Finally, a Fourier transform is performed to obtain the spectrum. No additional apodizing function has been applied to the data described here so that the effective apodizing function is a rectangle in the interferogram domain providing a sinc scanning function in the spectral domain. The calculated spectral radiances are obtained using the sinc scanning function at the identical spectral values as the calibrated experimental spectra.

Table 5. Characteristics of the HIS Instrument for Flight of 14 April 1986

Spectral Range	
Band I	590 - 1070 cm^{-1}
Band II	1040 - 1930 cm^{-1}
Band III	2070 - 2750 cm^{-1}
Platform	ER2
Altitude	19.6 km
View	nadir
Surface	ocean
Instrument temperature	ambient
Resolution (hwhm)	0.365 cm^{-1}
absolute	~ 1 K
relative	0.5 K

The particular data set we have utilized in this validation is from an ER2 flight over the ocean off the California coast on April 14, 1986. This data set has been chosen primarily because of the greater confidence in the characterization of the ocean surface properties relative to those for land surface. The calibrated spectral radiance in units of equivalent brightness temperature for the measurement set to be studied is shown in Figure 25. An input atmosphere for FASCODE developed by R. Knuteson at the University of Wisconsin is provided in Table 6. The temperature and water vapor profiles were obtained from routine local radiosonde measurements while profiles for the other molecular species were obtained from the U.S. Standard atmosphere. The mixing ratio for carbon dioxide has been taken as 345 ppmv. The surface emissivity has been taken as 1.0 and the surface temperature has been obtained from the equivalent brightness temperature in the spectral window since an independent measurement of the surface temperature was not available.

In Figure 26 we show the difference between the HIS measurement and a FASCODE calculation performed using this 24-layer atmosphere and the 1986 HITRAN database (Rothman et al., 1987). The agreement is generally satisfactory, but a number of spectroscopic issues are clearly evident. The large positive residuals at the 618, 720,

Table 6. The Input Atmosphere for the Validations in FASCODE Format

```

$ CALCULATION OF TRANSMITTANCES FROM RADIOSONDE NO. 81          ALL
HI=1 F4=1 CN=1 AE=0 EM=1 SC=1 FI=0 PL=0 TS=0 AM=0 MG=0 LA=0 MS=0      5      5
590.      1110.      0.      .0002      .001
287.      1.
24      7      1.000000      RAOB 72394 8610 H1=      19.67 H2=      .00 ANG= 180.000 LEN= 0
974.98      286.07      1      .00 1000.00 286.91      .43 950.00 285.22
8.778E+21 3.668E+20 2.878E+16 3.404E+17 1.584E+17 1.808E+18 2.223E+23 8.323E+23
934.99      284.93      1      .70 920.000 284.64
3.308E+21 2.197E+20 1.779E+16 2.038E+17 9.375E+16 1.083E+18 1.331E+23 5.003E+23
884.95      283.41      1      1.36 850.000 282.16
4.423E+21 5.130E+20 4.354E+16 4.760E+17 2.155E+17 2.529E+18 3.109E+23 1.172E+24
814.93      280.42      1      2.06 780.000 278.64
2.603E+21 5.122E+20 4.638E+16 4.753E+17 2.100E+17 2.525E+18 3.104E+23 1.172E+24
739.87      276.03      1      2.94 700.000 273.36
3.158E+21 5.860E+20 5.499E+16 5.438E+17 2.335E+17 2.889E+18 3.551E+23 1.340E+24
684.98      272.19      1      3.29 670.000 271.00
1.542E+21 2.193E+20 2.099E+16 2.035E+17 8.549E+16 1.081E+18 1.329E+23 5.014E+23
644.94      268.99      1      3.90 620.000 266.95
2.581E+21 3.664E+20 3.519E+16 3.399E+17 1.408E+17 1.806E+18 2.220E+23 8.374E+23
595.68      265.04      1      4.53 571.470 263.10
2.476E+21 3.552E+20 3.521E+16 3.296E+17 1.350E+17 1.751E+18 2.153E+23 8.119E+23
535.59      259.66      1      5.55 500.000 256.11
2.634E+21 5.233E+20 5.564E+16 4.856E+17 1.975E+17 2.580E+18 3.172E+23 1.197E+24
487.48      254.85      1      5.93 475.000 253.59
7.576E+20 1.830E+20 2.099E+16 1.698E+17 6.861E+16 9.019E+17 1.109E+23 4.187E+23
452.42      251.03      1      6.67 430.000 248.42
1.179E+21 3.293E+20 4.110E+16 3.056E+17 1.219E+17 1.623E+18 1.996E+23 7.538E+23
414.96      246.55      1      7.19 400.000 244.66
3.487E+20 2.193E+20 3.076E+16 2.036E+17 7.954E+16 1.081E+18 1.329E+23 5.026E+23
374.88      241.34      1      8.13 350.000 237.92
2.451E+20 3.659E+20 5.902E+16 3.395E+17 1.279E+17 1.801E+18 2.217E+23 8.385E+23
324.85      233.85      1      9.19 300.000 229.66
9.570E+19 3.659E+20 8.125E+16 3.391E+17 1.194E+17 1.797E+18 2.217E+23 8.387E+23
274.82      224.99      1      10.39 250.000 220.16
2.951E+19 3.656E+20 1.291E+17 3.371E+17 1.079E+17 1.788E+18 2.216E+23 8.383E+23
224.83      215.91      1      11.80 200.000 211.46
1.131E+19 3.654E+20 2.425E+17 3.323E+17 9.354E+16 1.774E+18 2.215E+23 8.380E+23
175.04      212.53      1      13.59 150.000 213.71
9.022E+18 3.661E+20 3.753E+17 3.252E+17 7.213E+16 1.752E+18 2.218E+23 8.392E+23
142.55      213.49      1      14.24 135.108 213.25
3.793E+18 1.088E+20 1.467E+17 9.476E+16 1.623E+16 5.136E+17 6.595E+22 2.495E+23
125.04      212.19      1      15.25 115.000 211.07
5.149E+18 1.471E+20 2.117E+17 1.263E+17 1.798E+16 6.874E+17 8.920E+22 3.374E+23
107.50      211.16      1      16.11 100.000 211.26
3.824E+18 1.097E+20 2.116E+17 9.221E+16 1.064E+16 5.056E+17 6.648E+22 2.515E+23
92.509      211.99      1      17.12 85.0000 212.76
4.798E+18 1.097E+20 2.445E+17 8.975E+16 8.615E+15 4.978E+17 6.650E+22 2.516E+23
77.498      212.61      1      18.33 70.0000 212.45
6.108E+18 1.097E+20 2.765E+17 8.593E+16 6.725E+15 4.868E+17 6.650E+22 2.516E+23
65.001      212.51      1      19.29 60.0000 212.58

```

Table 6. The Input Atmosphere for the Validations in FASCODE Format

```

4.917E+18 7.319E+19 2.489E+17 5.424E+16 3.481E+15 3.157E+17 4.436E+22 1.678E+23
58.198      212.66      1      19.67 56.3960 212.75
2.028E+18 2.638E+19 1.471E+17 1.875E+16 1.092E+15 1.113E+17 1.599E+22 6.047E+22
0.21962109 600.0665 1080.009 1 4 -.13775637 12 1 1 11 05
0.21962109 600.0665 1080.009 0 4 -.13775637 12 1 1 11 05
-1.

```

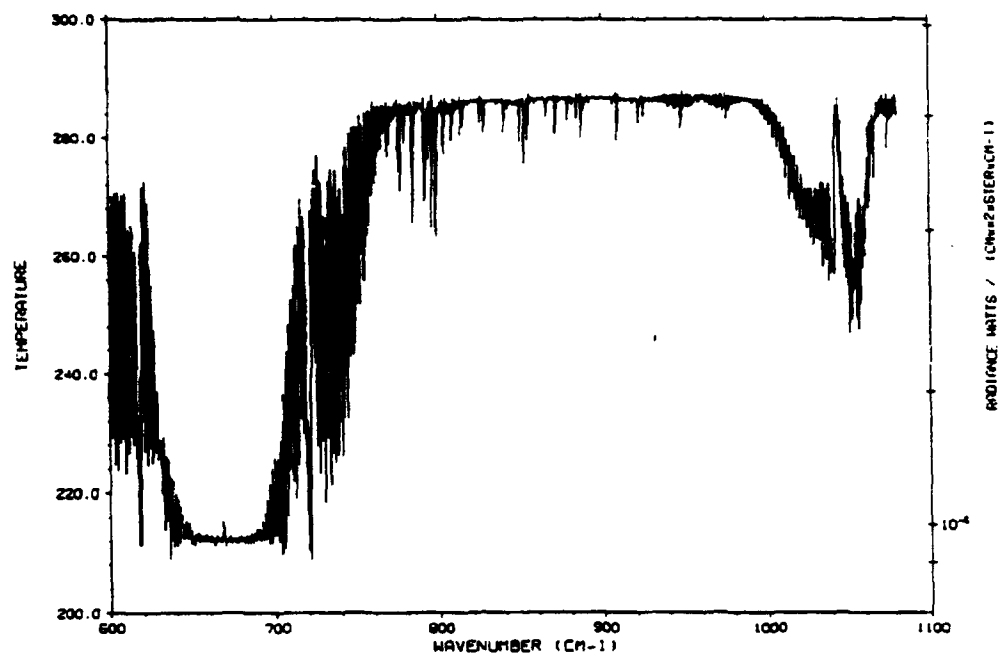


Figure 25. HIS equivalent brightness spectra from April 14, 1986: nadir view over ocean from 19.6 km.

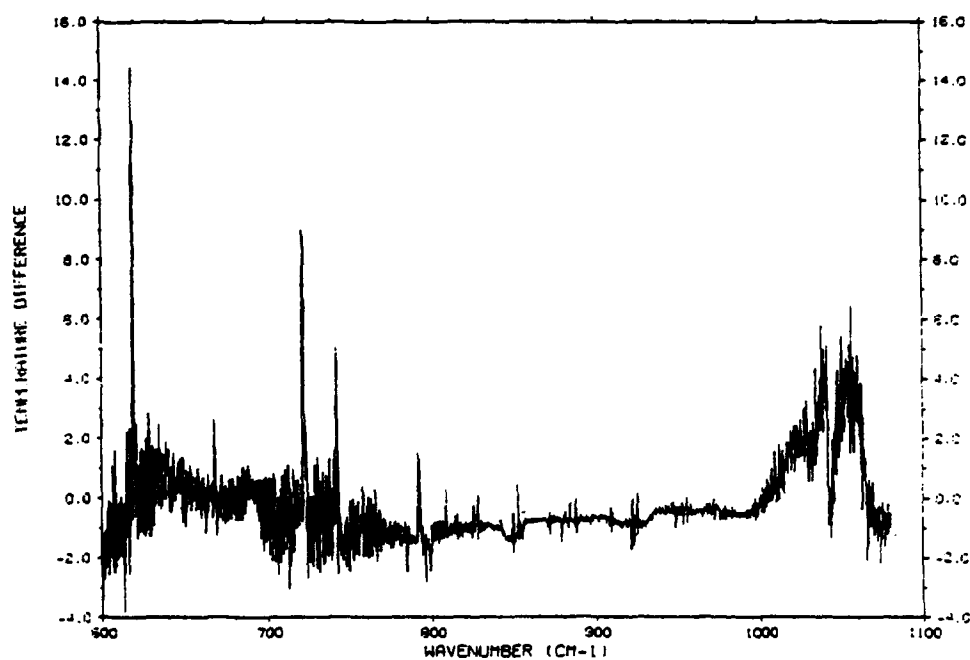


Figure 26. The difference spectrum in equivalent brightness temperature between the spectrum of Figure 25 and a calculated spectrum using FASCODE with the 1986 HITRAN line parameters. An error of 1 K in the window region at 1000 cm^{-1} corresponds to a 1.6% error in radiance.

740, and 791 Q-branches are due to line coupling. The positive residual at 667 cm^{-1} is actually due to a short path of warmer gas in the vicinity of the instrument pod and not to line coupling in the main carbon dioxide Q-branch. The broad negative features at 795, 850, and 920 cm^{-1} are due to CCl_4 , CFC11, and CFC12, respectively. Finally, the difference between the true ozone profile and the U.S. Standard profile assumed for this calculation is responsible for the spectral discrepancies from 990 to 1060 cm^{-1} . Despite the fact that the radiosondes were not especially well located temporally or spatially with respect to the observation, this validation based on the radiosonde data is remarkably good.

The effects of line coupling including its temperature dependence have been accounted for using line coupling coefficients of Hoke and Clough (1989) multiplied by a factor of 1.3 based on this and related spectra. The results are presented in Figure 27. Essential to these results are improved interim carbon dioxide line parameters provided by L.S. Rothman (1988). The improvement in the carbon dioxide line intensities are qualitatively consistent with those developed for ATMOS, Brown et al. (1987). The residuals for ozone have been reduced through the application of a retrieval algorithm to attain an improved ozone profile, Clough et al. (1990) and Isaacs et al. (1990). The remaining residual associated with the main Q-branch of carbon dioxide at 667 cm^{-1} due to warm gas near the instrument is unaffected by the inclusion of line coupling effects.

It is of interest to note in Figure 27 that the three spectral features with reduced radiance associated with CCl_4 at 795 cm^{-1} , CFC11 at 850 cm^{-1} , and CFC12 at 920 cm^{-1} are the manifestation of the greenhouse cooling effect attributable to these three anthropogenic gases. Using the option in the advanced spectral model to treat the effects of cross sections appropriate to the heavier molecules, we obtain the results shown in Figure 28. The option to perform a convolution to account for the difference in pressure between that appropriate to the atmospheric layers and the pressure at which the cross section data are provided was not available at the time these calculations were performed. The cross sections are due to Massie et al. (1985). The profiles for the species treated, CCl_4 , CFC11, and CFC12, have been obtained from the AER 2d chemistry model, Ko et al. (1990). The broad spectral features due to the radiative effects of these molecules is well accounted for as demonstrated in this residual spectrum.

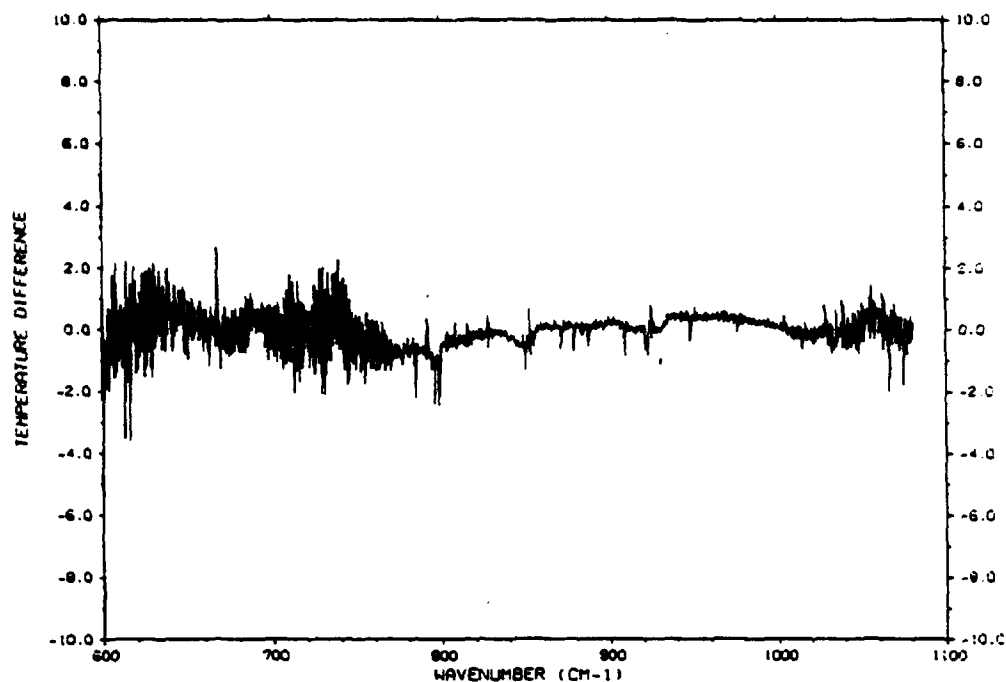


Figure 27. The difference spectrum in equivalent brightness temperature between the spectrum of Figure 25 and a calculated spectrum using FASCODE with the inclusion of the effects of line coupling and improved carbon dioxide line parameters.

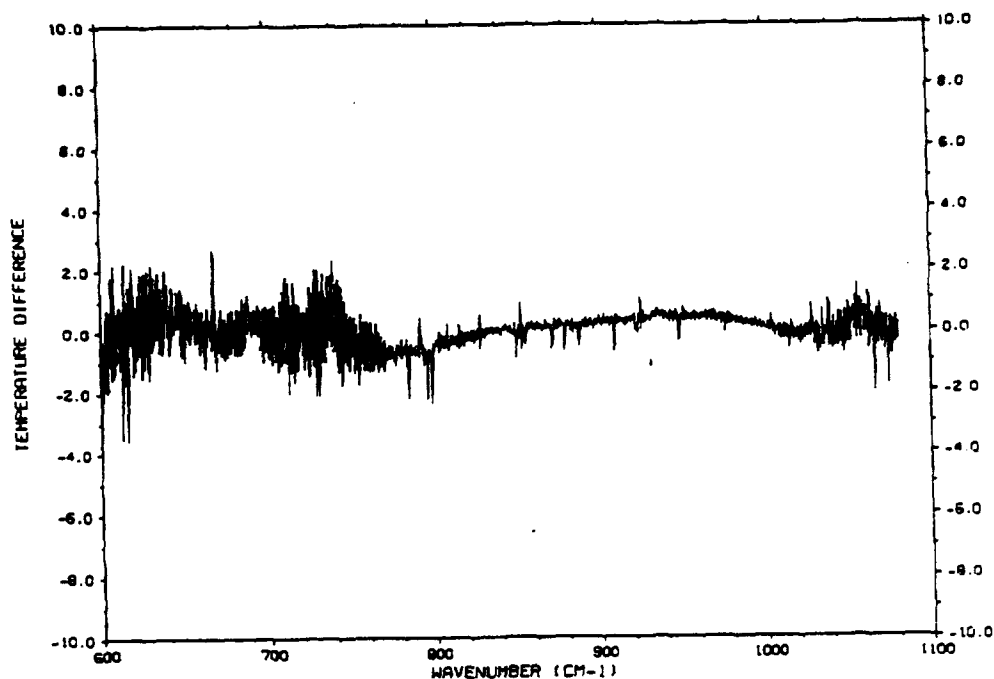


Figure 28. The difference spectrum in equivalent brightness temperature between the spectrum of Figure 25 and a calculated spectrum using FASCODE. The effect of CCl_4 at 795 cm^{-1} , CFC11 at 850 cm^{-1} and CFC12 at 920 cm^{-1} have been taken into account in addition to the effects included in Figure 27.

Of significant interest in Figure 28 is the very broad spectral behavior of the residual spectrum from 600 - 1100 cm^{-1} . A number of possibilities exist to explain this broad spectral behavior. An important explanation that we have not sufficiently explored is the spectral variation of the emissivity. Prabhakara et al. (1987) have suggested that thin cirrus clouds may have spectral effects similar to those observed here. In order to study this possibility we have invoked the cirrus cloud model available in LOWTRAN7 and adjusted the optical depth of the cloud layer to provide qualitative agreement with the observed spectrum. The cloud optical depth has been taken as 0.05 at 0.55 microns and the cloud has been placed at 13 km. The result for the introduction of the cloud model is provided in Figure 29. For computational expediency, conservative scattering has been assumed which is valid for the present case. The cloud is at a cold temperature so that the details of the cloud radiance is a secondary effect. The main role of the cloud is in attenuating the upwelling radiance due to warmer temperatures. The thin cirrus cloud model in LOWTRAN7 has been developed by Shettle and is characterized by spherical particles with a four micron mode radius. Additionally, the 1992 HITRAN line parameters have been used for the validation of Figure 29 and an additional iteration has been performed for the ozone profile.

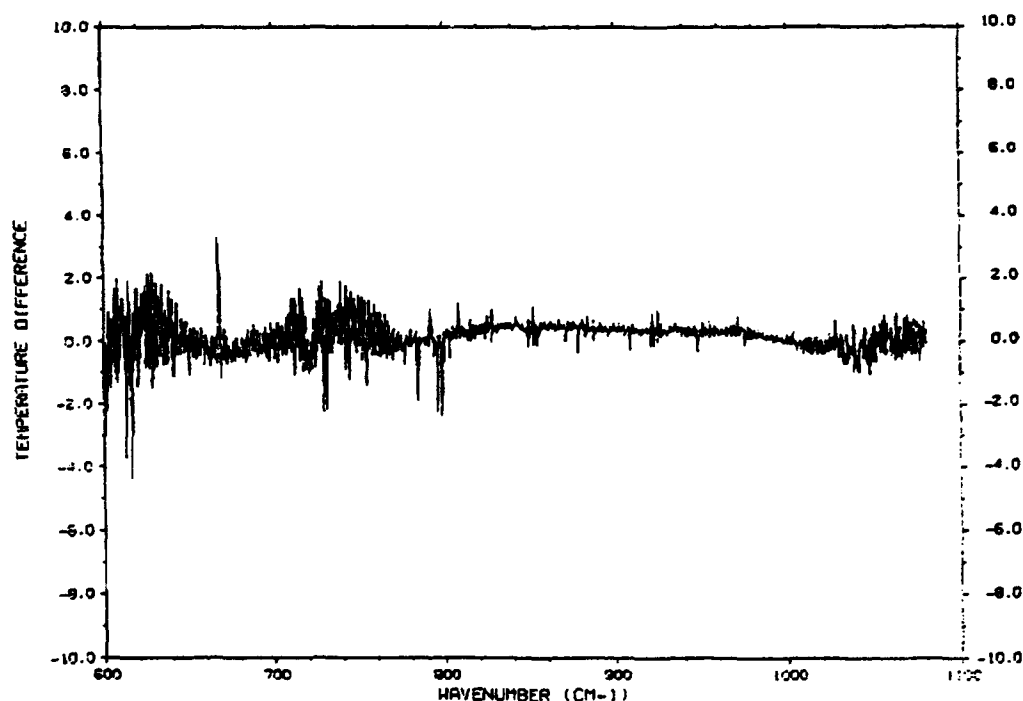


Figure 29. The difference spectrum in equivalent brightness temperature between the spectrum of Figure 25 and a calculated spectrum using FASCODE. The effect of a thin cirrus cloud at 13 km has been included in addition to the effects treated in Figures 27 and 28.

At this stage of the validation a number of conclusions can be drawn. Perhaps the most important concerns the high quality of the radiance spectrum, particularly when the nature of the platform, the ER2 aircraft, is considered. The noise level in the data is of the order of 0.1 K, the relative calibration appears to be of the order of 0.25 K and the absolute calibration gives every indication of being better than 1 K. If Figure 29 is compared with Figure 29, substantial improvement has been attained. The sharp, apparently random spectral residuals throughout the spectrum are associated with water vapor. The denser more regular residuals from 600 - 780 cm^{-1} are associated with carbon dioxide. The magnitude of the water vapor residuals is principally due to errors in the line strengths and widths, with a contribution from the radiosonde atmospheric description. The errors on the carbon dioxide region are apparently spectroscopic in nature and are due to errors in the line strengths and widths. It is important to recognize that the errors being considered here are of the order of 2% in the radiance. Also of interest is the general improvement in the water vapor residuals in the ν_2 region (above 800 cm^{-1}) and of the ozone residuals. These improvements in the spectral residuals are a direct consequence of improvements in the 1992 HITRAN line parameters.

Another important validation that has been performed is one for the same spectral region except that the HIS spectral radiometer was on the surface at Denver Colorado observing in the zenith mode. In Figure 30 is presented the radiance spectrum from 600 - 1100 cm^{-1} obtained with the HIS instrument. In Figure 31 is shown a difference spectrum in brightness temperature between the measurement and a calculation using the advanced spectral model. For this comparison the line coupling coefficients have again been multiplied by the factor of 1.3 consistent with the downlooking comparisons. In the comparison of Figure 32 the cross sections for the heavy molecular species have not been taken into account. Residuals due to CFC11 at 850 cm^{-1} and CFC12 at 920 cm^{-1} are again apparent. In this case the effect of the absorption is to provide a positive residual, i.e. the spectral model without inclusion of cross section effects is not calculating enough radiance in the lower layers in which the fluorocarbons are absorbing. It is of interest that for a completely different viewing situation and a different atmosphere, many of the same spectral residual features are apparent as in the downviewing spectra: spectral residuals associated with carbon dioxide and with water vapor.

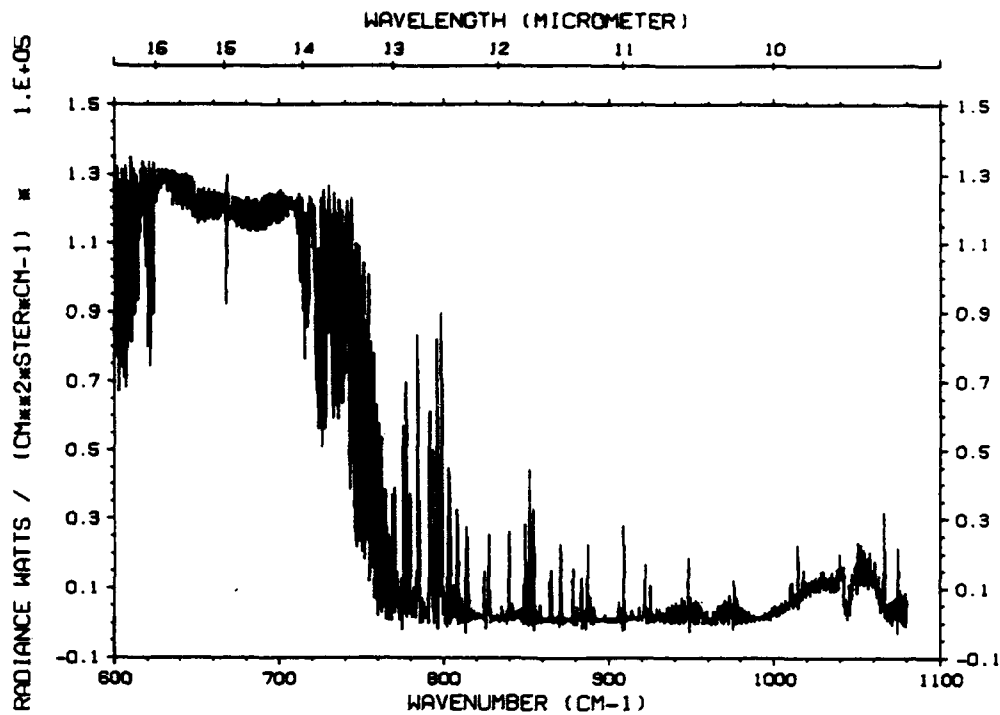


Figure 30. Zenith radiance spectrum observed with the U. of Wisconsin HIS instrument at Denver, CO, 1 Nov 1988, as part of the GAPEX campaign.

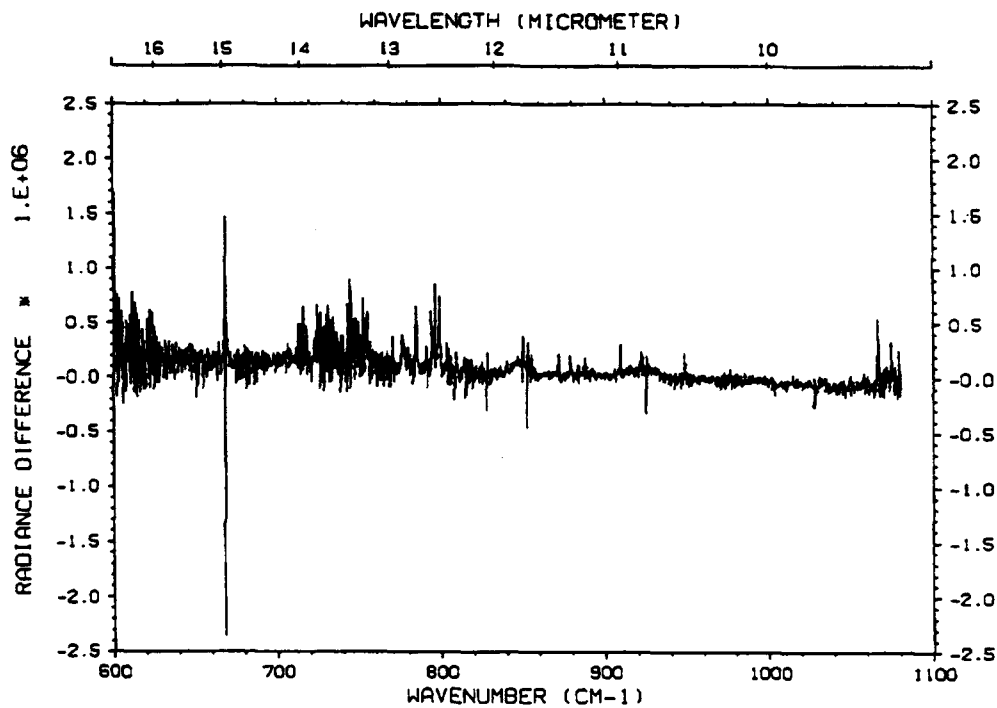


Figure 31. Radiance residuals between the observed spectral radiance of Figure 30 and a FASCODE calculation with a radiosonde defined atmosphere.

13.2 ITRA Microwave Validation

The international campaign to study the performance of line-by-line models (ITRA: Intercomparison of Transmittance and Radiance Algorithms) with respect to observed atmospheric radiance data has selected a dataset from Westwater et al. (1990) for the microwave region. During this reporting period, the performance of FASCODE has been evaluated with respect to this dataset. The dataset consists of zenith radiance measurements from the surface at three frequencies for 100 observational cases. The three frequencies are in the atmospheric windows at 20.6, 31.65 and 90.0 ghz.

In order to perform the necessary calculations with FASCODE, modifications to the atmospheric path computation program (FSCATM) were implemented to accommodate the large number of levels provided with the dataset for the specification of the atmospheric path. An abbreviated example of an input profile to the atmospheric layering program is provided in Table 7. The associated input to the FASCODE radiative transfer calculation obtained from utilizing the profile data from Table 7 is provided in Table 8. A study of the sensitivity of the FASCODE calculations to the layering indicates that the layering provided in Table 8 results in radiance calculations that are essentially invariant to finer atmospheric layering.

Radiance results using values for the oxygen line parameters included in FASCODE subroutine TESTMM as of 1 May 1991 were in poor agreement with the Westwater et al. brightness temperatures for the specific cases examined. Using this original version of TESTMM and a value of 2.75 K for the equivalent brightness temperature of the radiance from space, the observed and calculated brightness temperatures for the three frequencies were:

	<u>data of 88 10 29 1620</u>		
frequency (ghz)	20.6	31.65	90.0
observed (K)	17.66	12.32	31.23
calculated (K)	16.84	11.98	38.72

An effort was initiated to determine the cause of the rather serious disagreement at 90.0 ghz. Initial tests indicated that the sum rules on the line coupling coefficients, including temperature dependence, were satisfied. On examining the errors associated with

**Table 7. Abbreviated Input file for Atmospheric Layering Associated
with ITRA Microwave Comparison**

TEST CASE FOR FSCATM PROGRAM									
7	2	33	1	1	7	1			715.
1.611		60.000		0.000					
1.611		2.000		2.500		3.000	3.500	4.000	4.500
5.500		6.000		6.500		7.000	8.000	9.000	10.000
12.000		13.000		14.000		15.000	17.500	20.000	22.500
27.500		30.000		32.500		35.000	40.000	45.	50.
60.									55.
8810291620 317									
842.5	1.6110		7.60	-2.99		.47			
842.4	1.6120		10.00	-3.31		.39			
835.0	1.6850		6.90	-3.92		.46			
826.3	1.7720		9.90	-4.47		.36			
822.4	1.8110		11.20	-4.47		.33			
818.3	1.8530		13.20	-3.99		.30			
814.3	1.8940		14.30	-3.95		.28			
810.4	1.9350		14.20	-4.52		.27			
806.1	1.9790		14.00	-4.70		.27			
801.8	2.0240		13.80	-4.87		.27			
798.2	2.0620		13.70	-4.95		.27			
795.0	2.0960		13.70	-4.95		.27			
791.6	2.1320		13.50	-5.62		.26			
788.0	2.1710		13.30	-5.79		.26			
784.5	2.2080		12.90	-5.64		.27			
780.6	2.2500		12.70	-5.81		.27			
776.6	2.2930		12.30	-6.16		.27			
772.6	2.3360		11.90	-6.03		.28			
768.6	2.3790		11.50	-5.91		.29			
764.6	2.4230		11.10	-6.26		.29			
759.9	2.4740		10.60	-6.25		.30			
755.3	2.5250		10.20	-6.60		.30			
750.7	2.5760		9.70	-6.61		.31			
746.1	2.6270		9.20	-6.64		.32			
741.5	2.6780		8.70	-6.68		.33			
737.2	2.7260		8.20	-7.12		.33			
733.0	2.7730		7.80	-7.08		.34			
728.9	2.8190		7.30	-7.15		.35			
724.8	2.8660		6.90	-7.50		.35			
721.0	2.9090		6.50	-7.50		.36			
717.2	2.9520		6.00	-7.59		.37			
713.7	2.9920		5.60	-7.60		.38			
710.3	3.0310		5.30	-7.54		.39			
706.7	3.0730		5.00	-7.81		.39			
703.0	3.1160		4.60	-7.84		.40			
699.3	3.1590		4.20	-8.20		.40			
695.8	3.1990		3.90	-8.15		.41			
692.6	3.2370		3.60	-8.74		.40			
689.0	3.2790		3.30	-8.70		.41			

**Table 7. Abbreviated Input file for Atmospheric Layering Associated
with ITRA Microwave Comparison**

(continued)

685.6	3.3190	2.90	-9.06	.41
682.2	3.3590	2.60	-9.02	.42
678.8	3.4000	2.40	-9.51	.41
675.6	3.4380	2.10	-9.78	.41
672.2	3.4790	1.80	-10.06	.41
668.7	3.5210	1.40	-10.11	.42

Table 8. Layer Specifications Resulting from the Input File of Table 13.3

\$8810291620	317	WESTWATER ET. AL.										PROFILE #	1	FSCATM	
HI=1	F4=1	CN=1	AE=0	EM=1	SC=0	FI=0	PL=0	TS=1	AM=0	MG=0	LA=2	MS=0	XS=0	5	5
0.687142	0.687142	0.										.0	.0		
0.	1.														
32	7	1.000000	TWAT	T.	A	H1=	1.61	H2=	60.00	ANG=	0.000	LEN=	0		
823.34	284.25	3	1.61	842.500	280.75	2.00	804.090	287.06							
4.453E+21	0.000E+00	2.600E+16	2.612E+17	1.150E+17	0.000E+00	1.706E+23	6.411E+23								
780.84	285.64	3											2.50	757.551	283.55
5.063E+21	0.000E+00	3.234E+16	3.167E+17	1.372E+17	0.000E+00	2.069E+23	7.778E+23								
735.31	281.17	3											3.00	713.001	278.69
4.646E+21	0.000E+00	3.131E+16	3.030E+17	1.289E+17	0.000E+00	1.979E+23	7.443E+23								
691.73	276.70	3											3.50	670.448	274.75
4.170E+21	0.000E+00	3.009E+16	2.896E+17	1.211E+17	0.000E+00	1.892E+23	7.118E+23								
650.10	272.42	3											4.00	629.765	270.22
3.539E+21	0.000E+00	2.899E+16	2.765E+17	1.140E+17	0.000E+00	1.806E+23	6.799E+23								
610.36	267.93	3											4.50	590.949	266.12
3.133E+21	0.000E+00	2.861E+16	2.639E+17	1.079E+17	0.000E+00	1.724E+23	6.493E+23								
572.50	264.55	3											5.00	554.070	263.06
2.043E+21	0.000E+00	2.869E+16	2.507E+17	1.022E+17	0.000E+00	1.637E+23	6.177E+23								
536.52	261.07	3											5.50	518.994	258.87
1.562E+21	0.000E+00	2.853E+16	2.381E+17	9.676E+16	0.000E+00	1.555E+23	5.870E+23								
502.35	257.12	3											6.00	485.667	255.75
1.456E+21	0.000E+00	2.830E+16	2.263E+17	9.147E+16	0.000E+00	1.478E+23	5.580E+23								
469.95	254.45	3											6.50	454.189	252.69
1.244E+21	0.000E+00	2.880E+16	2.140E+17	8.557E+16	0.000E+00	1.398E+23	5.277E+23								
439.28	251.25	3											7.00	424.354	249.60
7.317E+20	0.000E+00	3.013E+16	2.025E+17	7.971E+16	0.000E+00	1.323E+23	4.999E+23								
396.86	245.83	3											8.00	369.340	242.28
1.034E+21	0.000E+00	6.287E+16	3.737E+17	1.423E+17	0.000E+00	2.441E+23	9.227E+23								
344.72	238.91	3											9.00	320.165	235.31
5.368E+20	0.000E+00	7.735E+16	3.338E+17	1.191E+17	0.000E+00	2.181E+23	8.250E+23								
297.58	231.54	3											10.00	275.272	228.20
2.316E+20	0.000E+00	1.012E+17	2.964E+17	9.726E+16	0.000E+00	1.943E+23	7.350E+23								
255.82	224.09	3											11.00	236.358	219.43
4.738E+19	0.000E+00	1.404E+17	2.610E+17	7.827E+16	0.000E+00	1.726E+23	6.530E+23								
219.02	215.26	3											12.00	201.680	212.11
1.127E+19	0.000E+00	1.925E+17	2.294E+17	6.194E+16	0.000E+00	1.538E+23	5.820E+23								
186.62	211.10	3											13.00	171.565	210.65
3.277E+18	0.000E+00	2.205E+17	1.963E+17	4.550E+16	0.000E+00	1.335E+23	5.054E+23								
158.82	212.35	3											14.00	146.095	213.93
1.210E+18	0.000E+00	2.373E+17	1.635E+17	3.083E+16	0.000E+00	1.130E+23	4.275E+23								
135.24	212.56	3											15.00	124.399	210.02
4.044E+17	0.000E+00	2.626E+17	1.367E+17	2.059E+16	0.000E+00	9.614E+22	3.638E+23								
103.60	209.46	3											17.50	82.8592	210.00
7.755E+16	0.000E+00	8.214E+17	2.516E+17	2.681E+16	0.000E+00	1.846E+23	6.988E+23								
69.103	211.11	3											20.00	55.2944	212.39
7.815E+17	0.000E+00	1.039E+18	1.471E+17	1.077E+16	0.000E+00	1.222E+23	4.624E+23								
46.195	213.80	3											22.50	37.1228	215.67
1.181E+18	0.000E+00	1.188E+18	8.463E+16	5.032E+15	0.000E+00	8.066E+22	3.053E+23								
31.076	217.35	3											25.00		
25.0391 219.31															

Table 8 Layer Specifications Resulting from the Input File of Table 13.3
(continued)

1.813E+17	0.000E+00	1.127E+18	4.872E+16	3.551E+15	0.000E+00	5.339E+22	2.021E+23
21.036	221.04		3			27.50	17.0328 223.43
0.000E+00	0.000E+00	9.299E+17	2.840E+16	2.642E+15	0.000E+00	3.555E+22	1.346E+23
14.353	225.74		3			30.00	11.6790 228.33
0.000E+00	0.000E+00	6.999E+17	1.708E+16	1.878E+15	0.000E+00	2.377E+22	8.994E+22
9.8708	230.75		3			32.50	8.06988 233.80
0.000E+00	0.000E+00	5.305E+17	9.910E+15	1.358E+15	0.000E+00	1.600E+22	6.054E+22
6.8480	236.84		3			35.00	5.63051 240.78
0.000E+00	0.000E+00	3.927E+17	5.431E+15	9.952E+14	0.000E+00	1.082E+22	4.093E+22
4.2257	246.91		3			40.00	2.82503 254.23
0.000E+00	0.000E+00	4.596E+17	4.183E+15	1.310E+15	0.000E+00	1.243E+22	4.703E+22
2.1443	258.86		3			45.00	1.46204 263.22
0.000E+00	0.000E+00	1.827E+17	8.652E+14	8.094E+14	0.000E+00	6.040E+21	2.286E+22
1.1155	265.33		3			50.000	.767683 265.51
0.000E+00	0.000E+00	6.211E+16	1.520E+14	5.490E+14	0.000E+00	3.075E+21	1.164E+22
.58470	263.83		3			55.000	.400472 260.32
0.000E+00	0.000E+00	1.910E+16	2.999E+13	4.202E+14	0.000E+00	1.622E+21	6.140E+21
.30270	256.15		3			60.000	.206091 251.09
0.000E+00	0.000E+00	6.071E+15	9.911E+12	3.487E+14	0.000E+00	8.647E+20	3.272E+21
1.055730							
3.002077							
-1.							

a number of observations, a pattern in the errors emerged. The errors were generally independent of the water column and the calculated brightness temperature at 90 ghz was consistently higher than the measurements. This systematic behavior around the main oxygen band at 60 ghz suggested that the problem was related to absorption by oxygen and, in particular, the neglect of coupling of the 60 ghz oxygen band with the band at 0 ghz and -60 ghz. A rereading of the paper by Rosenkranz lent support to this explanation. In his paper describing the development of his microwave model, Rosenkranz indicates that a value of -0.012 was added to all values of y for the 60 ghz band to account for the interaction with the other two bands.

In obtaining a correction to the oxygen line parameters in TESTMM, it was decided that the nominal values of the y 's and g 's calculated by Clough would constitute the starting point. This formalism had provided results generally consistent with other microwave radiative transfer models in more absorbing regions of the spectrum as evidenced in the previous ITRA intercomparison. The coupling parameters had been developed to be consistent with the treatment of line coupling and its temperature dependence in FASCODE. Inherent in this method is the treatment of the non-resonant band at zero frequency which incorporates a pressure dependent halfwidth, α_0 .

To develop a simple modification to the oxygen line parameters, two additional observations associated with low water column were studied: 88 11 11 1130 and 87 12 15 23 0. Two parameters were adjusted to obtain improved agreement between the calculations and the measurements: a constant term added to the y coefficients to account for line coupling with the non-resonant bands and a multiplicative scale factor applied to the y coefficients to account for approximations associated with the determination of the elements in the rate matrix. The sum rule on the y 's is preserved upon inclusion of the -60 ghz band in the sum since the y 's have opposite sign for the negative frequency transitions. The sum rule on the y 's is invariant to the scaling factor. The results provided below were obtained with a value of -0.017 for the additive constant for the y 's and a value of 1.3 for the scaling factor. Both quantities are dimensionless.

<u>data of 88 11 1 1130</u>			
frequency (ghz)	20.6	31.65	90.0
observed (K)	9.52	8.91	17.62
calculated (K)	10.52	10.47	18.92

data of 87 12 15 23 0

frequency (ghz)	20.6	31.65	90.0
observed (K)	7.60	9.20	14.40
calculated (K)	7.76	9.57	14.49

In order to assess the improvement attained in the presence of moderate water, the values for the data of 88 10 29 1620 were recalculated using the modifications discussed with the following result:

data of 88 10 29 1620

frequency (ghz)	20.6	31.65	90.0
observed (K)	17.66	12.32	31.23
calculated (K)	17.26	13.04	30.91

It is observed that a significant improvement has been achieved. The explanation for the need for the additive constant is relatively clear as previously discussed. The difference in value for this constant from that of Rosenkranz is presumably due to the fact that our values for y are different from his and that our formalism includes a second order contribution. The requirement for a scaling factor on the y coefficients is consistent with our experience with the line coupling coefficients for the Q-branches of carbon dioxide in the 600 - 800 cm^{-1} spectral region. It may be noted that the scaled coefficients are closer in magnitude to those of Rosenkranz which were obtained from a least squares fit to Liebe's laboratory measurements. The modified values for the parameters discussed here have been incorporated into a modified version of TESTMM which is available to PL/GP.

A meeting was held at AER with P.W. Rosenkranz, G.P. Anderson, M.L. Hoke and S.A. Clough in which the formalism for line coupling was discussed in general and Rosenkranz's approach to the oxygen problem was discussed in particular. Although definite conclusions were not reached, the discussions were interesting and should serve to enhance future developments. Of particular interest is the fact that Rosenkranz obtains values for the y 's by fitting to observed oxygen absorption spectra at a single pressure. The data used are due to Liebe. The results are then validated against similar spectra at other pressures. The Rosenkranz approach utilizes a least squares fitting procedure that obtains a least squares fit to the data with the constraint that the variation of the elements

along the superdiagonals of the rate matrix be small. It is important to note that Rosenkranz does not obtain the elements of the rate matrix with the conventional approach of fitting the halfwidths using the gap laws. This method of directly fitting the data ensures that the values obtained for the coupling coefficients will provide a satisfactory fit to the data. Both this approach and our approach, as described in this section, share a common element that an adjustment of the constant is made by performing a fit to available data.

13.3 High Altitude Modeling Support Activities

As an extension of the spectral model validation effort, we have conducted a series of studies involving the multispectral observations of the earthlimb. The context of these studies is the Midcourse Space Experiment (MSX), which is a research satellite with spectral sensors from the IR to the UV designed to measure the spectral and spatial variations of the earthlimb radiance over an altitude range of 60 to 200 km. The goal of these studies is to determine exactly what information about the atmosphere MSX can measure, and the optimum operating procedures to be used to obtain this information. In pursuit of these goals, the appropriate advanced spectral models were exercised to simulate the expected earthlimb signatures. These signatures, along with the sensor characteristics of MSX, were used to determine the information content of the expected measurements and to generate optimum experiment plans.

13.3.1 MSX

The MSX is an SDI research satellite designed for the specific purpose of measuring the spectral and spatial variation of the earthlimb radiance from 60 to 200 km for strategic applications. The satellite, due to be launched in 1994, is an 890 km, sun-synchronous polar orbiter with a 3 pm ascending node. The primary instruments are an IR interferometer and an imaging radiometer, collectively called SPIRIT III. The interferometer has six detectors, each filtered to be optimized for specific spectral regions from 4 to 20 micrometers, and is capable of 2 cm^{-1} resolution. The radiometer detectors consist of five linear arrays filtered for five bands covering 6 to 25 micrometers. The vertical field-of-view is provided by the linear array while the horizontal field-of-view is provided by a scanning mirror. SPIRIT III is cryogenically cooled and has a projected lifetime of about 2 years. SPIRIT III is complemented by a set of UV and Visible Imagers and Spectrographic Imagers (UVISI). Also on board is the Space Based Visible Sensor (SBV), a high spatial resolution instrument designed to track objects in space. The optical lines-of-sight of the

different instruments are fixed with regard to the spacecraft so that pointing the instruments requires rotating the spacecraft as a whole. In the "park" position, when not actively taking measurements, the spacecraft is viewing deep space so as to minimize the heat load on the cryogenically cooled components. The projected duty cycle (the time spent taking measurements) is about 10 percent.

MSX is designed to fulfill a set of scientific and systems requirements listed in the MSX Science Modeling Requirements Document (SMRD) and Systems Requirements Document (SRD). These two documents list limitations and deficiencies in our knowledge of quiescent and disturbed earthlimb radiance backgrounds which limit our ability to design strategic defense systems. For the purpose of this study, the relevant requirements are from the SMRD as follows:

- 4.7.1 Database Deficiencies/Requirements: deficiencies in measurement databases of earthlimb radiance.
- 4.7.2 Radiance Code Deficiencies: deficiencies in the models and codes for predicting earthlimb radiance.
- 4.7.3 Atmospheric Compositional Model Deficiencies: deficiencies in the models of atmospheric composition of radiatively active species.

We have investigated the means to satisfy these requirements given the capabilities of MSX. Specifically, we have investigated the particular experiments which would best utilize the multispectral capabilities of MSX to obtain vertical profiles of limb radiance and of radiatively active species.

13.3.2 Celestial Occultation Experiment

In this study, we sought to determine whether MSX could obtain profiles of trace species by measuring the transmitted radiation from a star, planet or the Moon in occultation. Using one of these celestial objects as a source, the transmitted radiance is measured as the object rises or sets through the atmosphere. The absorption is determined by comparing the transmitted radiance for each tangent height to the source signature, as measured at a high elevation angle. The constituent profile would be determined from the absorption using, for example, an onion-peeling technique. The question to be answered here is: is there sufficient information in the transmitted source radiance to determine the profile?

The results of this study are shown in Figure 32 which shows the magnitudes of the different source of IR radiation for this experiment compared to the noise-equivalent source radiance (NESR) of MSX. This figure shows the radiance for a limb tangent height of 60 km. The candidate celestial sources are the dayside and nightside Moon, IRC 10216 (the brightest IR star), and Sirius (the brightest visible star). In addition to these sources, there is the background zodiacal light, here shown at its maximum. The atmospheric radiance was computed by SHARC (Strategic High-Altitude Radiance Code). These different source radiances are compared to the NESR of the SPIRIT III interferometer.

This figure shows that, at 60 km, the radiance from even the brightest IR stellar source is 4 orders of magnitude below the peak of the atmospheric radiance. Even with a signal-to-noise of 1000, it does not appear possible to obtain a 'signal' of sufficient accuracy by viewing a star. The radiance from the dayside Moon is at least an order of

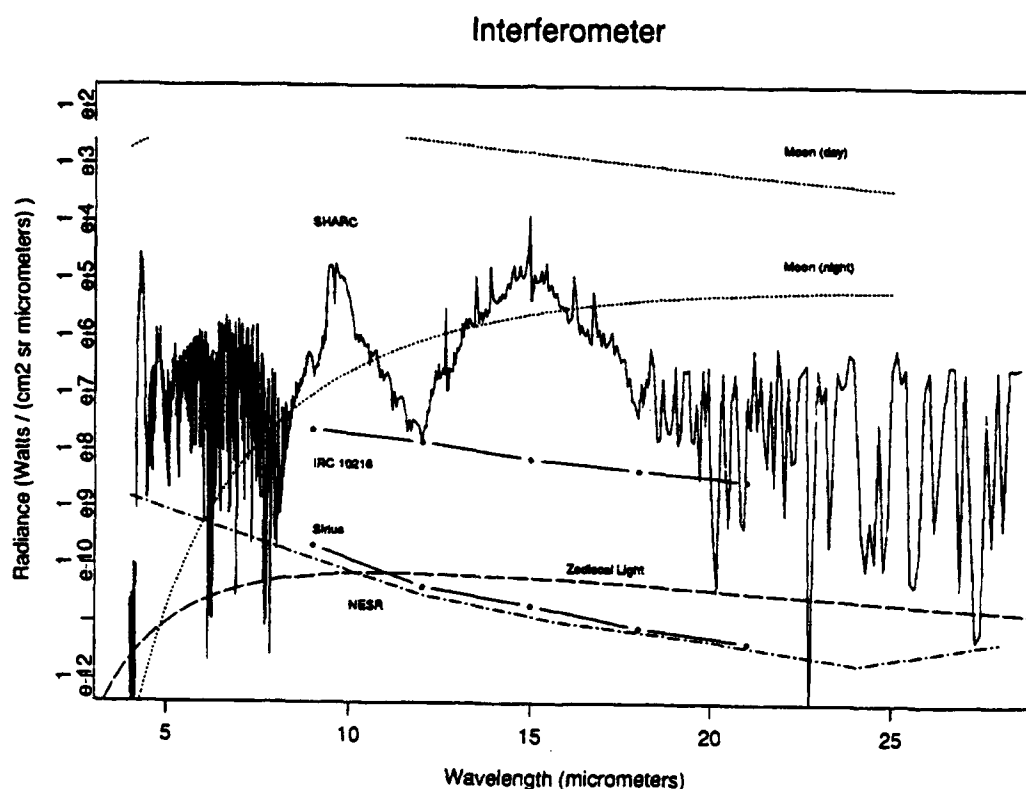


Figure 32. Sources of Spectral Radiance as Seen by the Spirit III Interferometer Viewing the Limb at a Tangent Height of 60 km. The dotted lines labeled Moon are for a blackbody of 410 and 110 K respectively, the lines labeled IRC 10216 and Sirius are the spectra of these two stars from the IRAS Catalog, the line marked SHARC is the atmospheric radiance for a 60 km tangent height, and the line labeled NESR is the noise-equivalent spectral radiance for the SPIRIT III interferometer.

magnitude greater than that of the atmosphere. However, a signal of this magnitude would place a large heat load on the detector and greatly limit the lifetime of the cryogen.

13.3.3 Earthlimb Experiments

In its normal operation, MSX measures the atmospheric earthlimb radiance without regard to the celestial background. Given the orbital characteristics and instrument capabilities, we sought to determine a set of experiments which would best obtain the measurements needed to satisfy the scientific requirements outlined earlier. In this context, an experiment is a set of spacecraft maneuvers, from park to park, designed to produce a measurement dataset which can then be analyzed to obtain the desired product, e.g. a vertical profile of species concentration. The experiment plan includes:

- a. the detailed spacecraft maneuvers - tangent height and azimuth versus time,
- b. the configuration of all the instrument, e.g. interferometer resolution, mirror field-of-view, and UVISI filters,
- c. atmospheric state requirements, e.g. quiescent atmosphere versus active aurora or high K_p ,
- d. auxiliary data requirements, e.g. DMSP imagery, profiles and limb spectra from UARS.

The experiment plan must ensure that all the data necessary to obtain the desired results are recorded while at the same time none of the spacecraft limitations are violated, e.g. data rate and recording time, and maximum acceleration and velocity.

We created two experiment plans to measure the quiescent earthlimb radiance. Their titles are listed in Table 9. In each experiment, the objective is to measure vertical profiles of earthlimb radiance spectra over a sufficiently localized space so that the profiles

Table 9. Earthlimb Experiment Plans

Number	Title
ELE-1	Airglow Staircase Survey
ELE-10	Vertical Profile Survey

can be inverted to obtain profiles of the radiating species. In experiment ELE-1, the spacecraft views perpendicular to the line of travel and performs a staircase scan of the limb. Figure 33 shows the tangent height versus time for a single staircase maneuver. The spacecraft holds at each tangent height long enough to take about 6 interferograms at high resolution. In the time required to perform one staircase maneuver, the spacecraft drifts through 15 degrees of latitude. A series of six of these maneuvers are performed as the spacecraft moves between the equator and the pole (or pole and equator). The full experiment timeline is shown in Figure 34.

Experiment ELE-10 is a variant on ELE-1. Instead of a staircase scan, it performs a sawtooth-type scan, with a constantly changing tangent height as shown in Figure 35. Although change in the tangent height over the measurement of a single interferogram will distort the resulting spectrum, studies have shown that the distortion is within acceptable limits. Fourteen of these maneuvers are performed over one quarter orbit, each covering 6 degrees of latitude. Compared to ELE-1, this experiment trades off accuracy in the spectra for increased vertical and horizontal resolution.

13.3.4 MSX Contributions to Global Climate Monitoring

The Air Force has shown interest in applying MSX measurements to support research in global climate monitoring. Given the types of multispectral sensors on board, and certain special operational characteristics of its sensor system, the possibility exists that MSX can contribute supplemental measurements to the national and international global change programs. In response to this interest, we have identified three specific scientific issues related to global change to which MSX could potentially contribute. In each case, MSX's unique capabilities, particularly its high altitude coverage and high sensitivity, can supplement existing data. In addition, we outlined a systematic approach to the further study of MSX in global change monitoring, based upon the program documents for the UARS and EOS programs. These ideas are incorporated in a white paper titled "MSX: Potential Contribution to the Global Change Program" (Gallery et al., 1991).

14. SUPPORT FOR ANNUAL REVIEW CONFERENCE

In order to properly develop models with the general applicability and acceptance of the AFGL radiance models, it is necessary to have a forum in which issues related to the

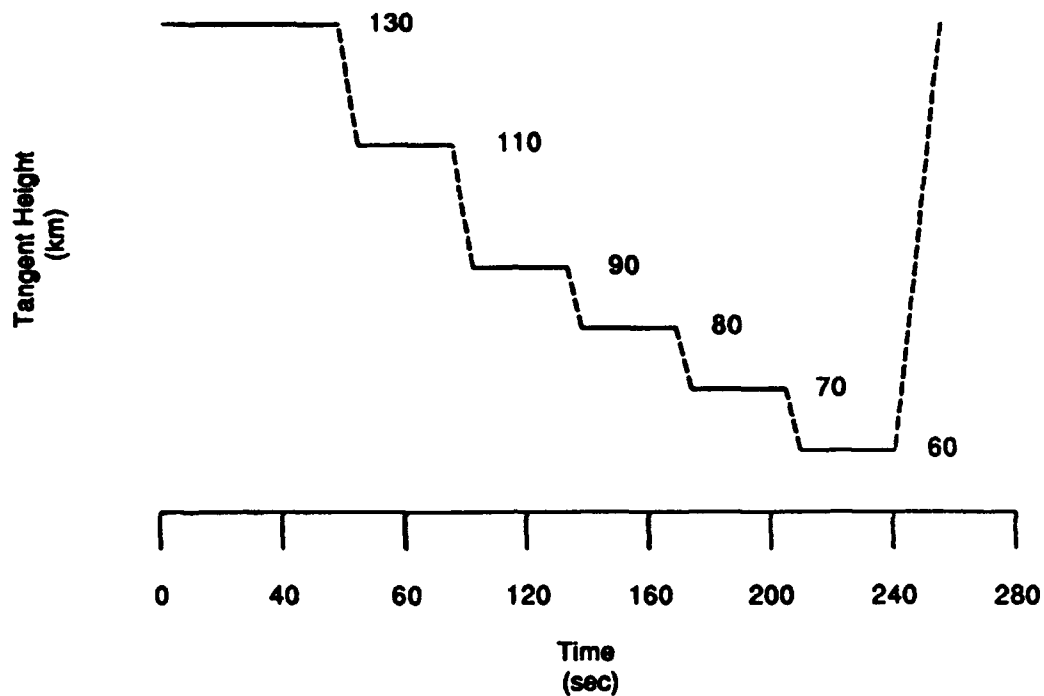


Figure 33. Timeline for the Stairstep Maneuver for ELE-1.

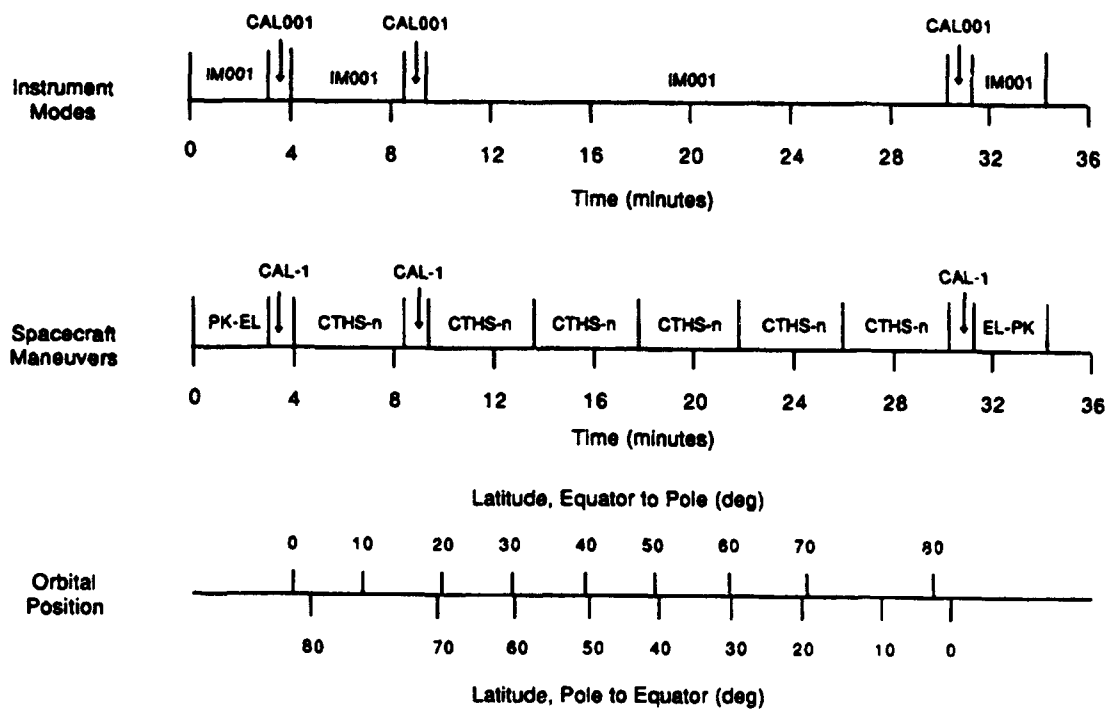


Figure 34. Experiment Timeline, From Park to Park, for ELE-1 Showing the Instrument Modes, the Spacecraft Maneuvers, and the Orbital Positions.

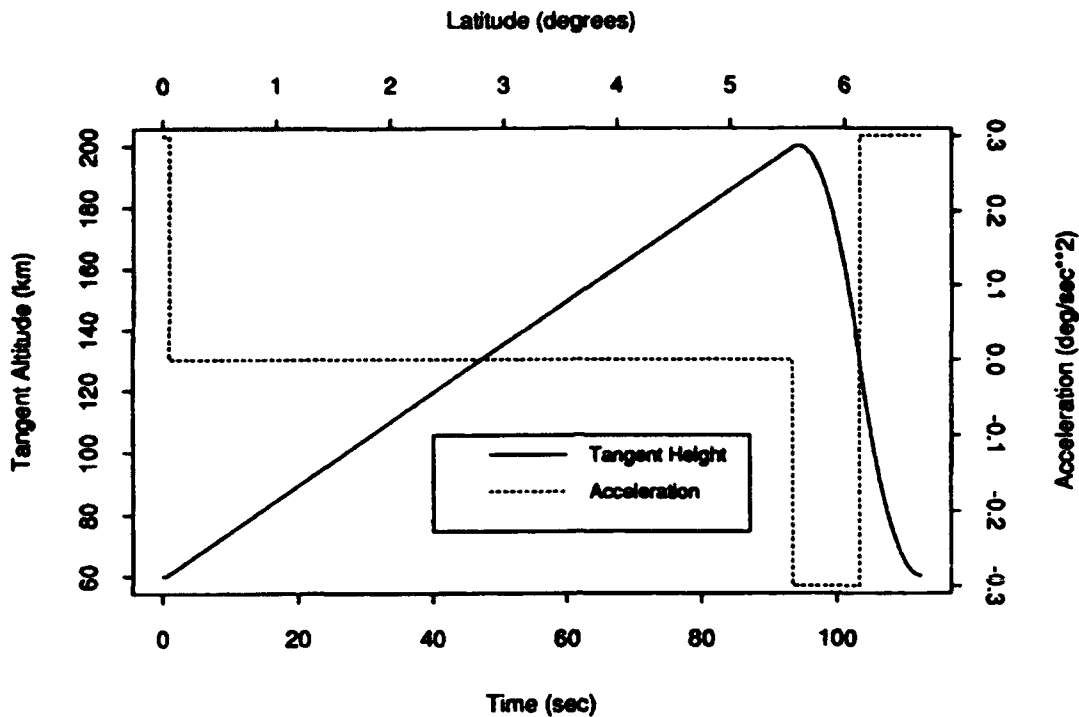


Figure 35. Timeline for the Sawtooth Vertical Profile Scan for ELE-10.

models can be addressed. In preparation for the 1990, 1991 and 1992 annual review conferences, E. Stenhouse of AER worked with F. Kneizys and L. Abreu of PL/GP. Preparation included the creation of a mailing list for potential attendees which involved updating the previous year's mailing list with changes of addresses, deletions and additions of names. When this was completed, the initial invitation and call for abstracts were mailed out. The next task was to type and mail out preliminary conference information including: preliminary conference programs, hotel information in the area, and maps to AFGL. Final conference information to be handed out during registration included: final conference programs, abstracts of each paper to be presented, name badges and coffee/donut tickets for attendees. E. Stenhouse participated in the registration process during the conference at GL which involved registering and providing support to the attendees. After the conference was concluded, work for the conference proceedings began which involved xeroxing viewgraphs from each talk and coordinating them with the abstracts, word processing of the report itself, preparing a list of attendees to be included as an appendix, and preparing a final product to be reproduced and mailed to all conference attendees.

15. CONCLUSIONS

This report has documented the results of a research program in advanced spectral modeling designed to address a variety of current research topics related to atmospheric state definition, long path surveillance, radiative transfer in cloudy environments and improved capabilities for defining highly disturbed environments. These topics included capabilities to: (a) accommodate the use of cross section data for transmittance calculations, (b) perform generalized multiple scattering calculations, (c) calculate both heating and dissociative fluxes, (d) provide radar and lidar backscatter coefficients, (e) incorporate surface reflection and emissivity effects including those of surface polarization on atmospheric radiance calculations, (f) extend NLTE capabilities, (g) modify the isotopic ratio, and (h) perform Fourier transform/interferometer studies. The approach taken in this program has been to improve model physics with improvement quantified and assessed by model validation. The work reported here has focused on implementations of these enhancements in the current versions of the Phillips Laboratory codes: LOWTRAN7 and FASCOD3, however, applications for MODTRAN have been suggested where appropriate.

16. REFERENCES

- Brown, L.R., C.B. Farmer, C.P. Rinsland, and R.A. Toth, 1987: Molecular line parameters for the atmospheric trace molecule spectroscopy experiment. *Appl. Opt.*, 26, 5154-5182.
- Clough, S.A., F.X. Kneizys, L.S. Rothman, and W.O. Gallery, 1981: Atmospheric spectral transmittance and radiance: FASCOD1B, Proc. of Soc. Photo. Opt. Instrum. Eng., 277, 152-1661.
- Clough, S.A., F.X. Kneizys, E.P. Shettle, and G.P. Anderson, 1986: Atmospheric radiance and transmittance: FASCOD2. Proceedings of the Sixth Conference on Atmospheric Radiance, Williamsburg, VA.
- Clough, S. A., R.D. Worsham, W.L. Smith, H.E. Revercomb, R.O. Knuteson, H.M. Woolf, G.P. Anderson, M.L. Hoke, and F.X. Kneizys, 1989: Validation of FASCOD2 Calculations with HIS Spectral Radiance Measurements, Proc of IRS '88, eds. J. Lenoble and J.F. Geleyn, A. Deepak Publishing.
- Clough, S.A., R.G. Isaacs, R.D. Worsham and J.L. Moncet, 1990: Application of the Optimal Probability Method to the Retrieval of Temperature, Water Vapor and Ozone Profiles, Proc. of the Meeting on Optical Remote Sensing of the Atmosphere, Incline Village NE, 57-59.
- Curran, R.J., 1971: Ocean color determination through a scattering atmosphere, *Appl. Opt.*, 11:1857-1866.

- Eaton, F.D., and I. Dirmhirn, 1979: Reflected irradiance indicatrices of natural surfaces and their effect on albedo, *Appl. Opt.*, 18:994-1008.
- Gallery, W. O., and S. A. Clough, 1992: FFTSCAN: A Program For Spectral Smoothing in the Fourier Domain, PL-TR-92-2131. **ADA264921**
- Gallery, W.O., J. Rodriguez, and D. Chang, 1991: MSX: Potential Contribution to the Global Change Program (unpublished).
- Gamache, R.R., R.L. Hawkins and L.S. Rothman, 1990: Total Internal Partition Sums in the Temperature Range 70-3000K: Atmospheric Linear Molecules, *J. Molec. Spectry*, 142, 205-219.
- Hoke, M.L., S.A. Clough, W. Lafferty, and B. Olson, 1989: Line coupling in oxygen and carbon dioxide. Proc. of IRS '88, eds. J. Lenoble and J.F. Geleyn, A. Deepak Publishing, 368-371.
- Isaacs, R.G., and A.M. Vogelmann, 1988: Multispectral Sensor Data Simulation Modeling Based on the Multiple Scattering LOWTRAN Code. *Rem. Sens. Envir.*, 26, 75-99.
- Isaacs, R.G., W.C. Wang, R.D. Worsham, and S.D. Goldenberg, 1987: Multiple scattering treatment for use in the LOWTRAN and FASCODE models, *Appl. Opt.*, 26(7):1272-1281.
- Isaacs, R.G., M. Livshits, R.D. Worsham, 1988: Scattering properties of precipitation for the AFGL RADTRAN model. *App. Opt.*, 27:1, 14-16.
- Isaacs, R. G., Worsham, R. D., & Lindner, B. L., 1989a: Characterizing microwave propagation using the AFGL microwave attenuation/transmittance/brightness temperature code (Technical Report No. AFGL-TR-89-0188). Air Force Geophysics Laboratory, Hanscom AFB, MA 01731. **ADA220248**
- Isaacs, R.G., Y.Q. Jin, R.D. Worsham, G. Deblonde, V.J. Falcone, Jr., 1989b: The RADTRAN Microwave Surface Emission Models, *IEEE Trans. on Geosci. and Remote Sensing*, Vol. 27, No. 4.
- Isaacs, R.G., S.A. Clough, R.D. Worsham, J.-L. Moncet, B.L. Lindner, and L.D. Kaplan, 1990: Path Characterization Algorithms for FASCODE. Final Report. 14 March 1990. Geophysics Laboratory, Air Force Systems Command, HanscomAFB, MA. GL-TR-90-0080, **ADA231914**.
- Kneizys, F.X., E.P. Shettle, W.O. Gallery, J.H. Chetwynd, Jr., L.W. Abreu, J.E.A. Selby, S.A. Clough, and R.W. Fenn, 1983: Atmospheric transmittance/radiance: Computer code LOWTRAN6. Technical Report 83-0187, Air Force Geophysics Laboratory. **ADA137786**
- Ko et al., 1990: Private communication.
- Massie, S.T., A. Goldman, D.G. Murcray and J.C. Gille, 1985: Approximate Absorption Cross Sections of F12, F11, ClONO₂, N₂O₅, HNO₃, CCl₄, CF₄, F21, F113, F114, HNO₄. *Appl. Opt.*, 24, 3426.

- McCartney, E.J., 1976: *Optics of the Atmospheric Scattering by Molecules and Particles*. J. Wiley, New York, 1976.
- Murcray, F.H., F.J. Murcray, D.G. Murcray, and W.J. Williams, 1981: Stratospheric Cryogenic Infrared Balloon Experiment, AFGL, Hanscom AFB, MA. AFGL-TR-81-0186, AD-A104168.
- Prabhakara, C., R.S. Fraser, G. Dalu, M.-L. Wu, R.J. Curran, and T.L. Styles, 1988: Thin cirrus clouds: seasonal distribution over oceans deduced from Nimbus 4 IRIS, *J. Appl. Meteor.*, **27**, 379-399.
- Revercomb, H.E., H. Buijs, H.B. Howell, D.D. LaPorte, W.L. Smith and L.A. Sromovsky, 1988: Radiometric calibration of IR spectrometers: solution to a problem with the High-Resolution Interferometer Sounder. *Appl. Opt.*, **27**, 3210-3218.
- Rinsland, C.P., R. Zander, J.S. Namkung, C.B. Farmer, and R.H. Norton, 1989: Stratospheric Infrared Continuum Absorptions Observed by the ATMOS Instrument. *J. Geophys. Res.*, **94**:D13, pp. 16,303-16,322.
- Rothman, L.S., 1988: Private communication.
- Rothman, L.S., R.R. Gamache, A. Goldman, L.R. Brown, R.A. Toth, H.M. pickett, J.-M. Flaud, C. Camy-Peyret, A. Barbe, N. Husson, P. Rinsland and M.A.H. Smith, 1987: The HITRAN database: 1986 edition. *Appl. Opt.*, **26**, 19,4058-4097.
- Savage, R.C., 1978: Radiative Properties of Hydrometeors at Microwave Frequencies, *J. Appl. Meteor.*, **17**, 904.
- Sidran, M., 1981: Broadband reflectance and emissivity of specular and rough water surfaces, *Appl. Opt.*, **20**:3176-3183.
- Smith, H.J.P., Dube, D.J., Gardner, M.E., Clough, S.A. Kneizys, F.X., and Rothman, L.S., 1978: FASCODE - Fast atmospheric signature code (spectral transmittance and radiance. (Tech. Report #AFGL-TR-78-0081). AFGL, Hanscom AFB, MA 01731. ADA057506
- Smith, W.L., H.M. Woolf, C.M. Hayden, D.Q. Wark and L.M. McMillan, 1979: The TIROS-N operational vertical sounder, *Bull. Am. Meteorol. Soc.*, **60**, 1177-1187.
- Smith, W.L., H.E. Revercomb, H.B. Howell, and H.M. Woolf, 1983: HIS - A satellite instrument to observe temperature and moisture profiles wit high vertical resolution, paper presented at Fifth Conference on Atmospheric Radiation, Am. Meteorol. Soc., Baltimore, MD, Oct 31 to Nov. 4.
- Stamnes, K. and P. Conklin, 1984: A new multi-layer discrete ordinate approach to radiative transfer in vertically inhomogeneous atmospheres, *J. Quant. Spectrosc. Radiat. Transfer*, **31**:273-282.
- Warren, S.G. and W. J. Wiscombe, 1980: A model for the spectral albedo of snow. I: Pure snow. *J. Atmos. Sci.*, **37**:2712-2733.

- Westwater, E.R., J.B. Snider and M.J. Falls, 1990: Ground-Based radiometric observations of Atmospheric Emission and Attenuation at 20.6, 31.65, and 90.0 GHz: A Comparison of Measurements and Theory IEEE Trans. Antennas Propag., vol. AP-38, pp. 1569-1580.
- Wiscombe, W.J. and S.G. Warren, 1980: A model for the spectral albedo of snow. II: Snow containing aerosols, *J. Atmos. Sci.*, 37:2734-2745.
- Zander, R., 1988: private communication.